

STUDY OF FLOW IN A FRACTURE UNDER SHEAR: PROGRESS REPORT

Prepared for

**Nuclear Regulatory Commission
Contract NRC-02-93-005**

Prepared by

**Center for Nuclear Waste Regulatory Analyses
San Antonio, Texas**

October 1995



**STUDY OF FLOW IN A FRACTURE UNDER SHEAR:
PROGRESS REPORT**

Prepared for

**Nuclear Regulatory Commission
Contract NRC-02-93-005**

Prepared by

**Sitakanta Mohanty
Ronald T. Green
Kristi A. Meyers-James**

**Center for Nuclear Waste Regulatory Analyses
San Antonio, Texas**

October 1995

PREVIOUS REPORTS IN SERIES

| Number | Name | Date Issued |
|---------------|---|----------------|
| NUREG/CR-6283 | Field Site Investigation: Effect of Mine Seismicity on Groundwater Hydrology | April 1995 |
| CNWRA 94-024 | Single Fracture Flow Behavior of Apache Leap Tuff Under Normal and Shear Loads | October 1994 |
| CNWRA 94-021 | Thermo-Hydro-Mechanical Coupled Modeling: Big Ben Experiment, TC3 DECOVALEX—Phase III | September 1994 |
| CNWRA 93-002 | Thermo-Hydro-Mechanical Coupled Modeling: Near-Field Repository Model, BMT3 DECOVALEX—Phase II | August 1993 |
| NUREG/CR-6021 | A Literature Review of Coupled Thermal-Hydrologic-Mechanical-Chemical Processes Pertinent to the Proposed High-Level Nuclear Waste Repository at Yucca Mountain | July 1993 |
| CNWRA 92-005 | Thermo-Hydro-Mechanical Coupled Modeling: Multiple Fracture Model BMT2. Coupled Stress-Flow Model, TC1 DECOVALEX—Phase I | April 1992 |

ABSTRACT

The near field of the proposed repository at the Yucca Mountain (YM) site is likely to experience coupled thermal, mechanical, and hydrological (TMH) interactions. To evaluate the consequence of these interactions, the key parameters controlling these processes need to be identified and adequate data need to be gathered so that a large-scale prediction of this process will be feasible. Current data availability for such coupled processes is very limited. The Center for Nuclear Waste Regulatory Analyses is pursuing experimental activities in the mechanical-hydrological (MH) interaction studies with emphasis on fluid flow through rock fractures, which is a subset of TMH coupled processes research. In conducting limited MH experiments in FY94, needs have been identified to modify the MH experiment apparatus as well as to conduct some basic laboratory and numerical experimentation studies that will enhance the design of MH experiments. The activities reported here include modifications to the MH experimental apparatus based on the deficiencies identified during the MH experiments conducted in FY94, experimental determination of fracture volume and fracture absolute permeability, numerical determination of fracture aperture from fracture profile data, the effect of disturbing the rock joint from its naturally occurring condition on fracture permeability, and focused literature review on fracture flow. The modified MH apparatus, along with the techniques developed in auxiliary experiments for the determination of fracture volume, fracture absolute permeability, and fracture aperture, is suitable for conducting either saturated or unsaturated fracture flow experiments under normal and shear loads. The fracture permeability values determined from the flow experiments were found to be nearly 100 times smaller than the permeability estimate based on the arithmetic mean aperture determined from the pycnometer method. Flow experiments conducted before and after disturbing the naturally occurring condition of a fracture (i.e., force-splitting the fracture) revealed up to one order of magnitude increase in the fracture conductivity. Analysis of fracture aperture distribution using an induced fracture in an Apache Leap tuff specimen revealed that, in spite of the strong heterogeneity in the fracture surface topography, the aperture distribution was relatively uniform. Although the aperture configuration carried a signature of the heterogeneity in the surface profile, it does not show the strong correlation and anisotropy. Fracture surface chip-off could potentially give rise to flow paths and influence the statistical properties of the aperture distribution. Numerical experimentation shows that, under shear displacement, the aperture distribution deviated from log-normal and tended to be more gaussian than log-normal. At larger shear displacements, a shift from unimodal to bimodal aperture distribution could occur. A 13-fold increase in the equivalent fracture conductivity was observed as a result of rock dilation under numerical shear displacement.

CONTENTS

| Section | Page |
|--|------|
| FIGURES | vii |
| TABLES | ix |
| ACKNOWLEDGMENTS | xi |
| EXECUTIVE SUMMARY | xiii |
| 1 INTRODUCTION | 1-1 |
| 1.1 BACKGROUND | 1-1 |
| 1.2 SCOPE | 1-3 |
| 2 LITERATURE REVIEW | 2-1 |
| 2.1 THEORY OF FLUID FLOW IN FRACTURES | 2-1 |
| 2.2 FLOW CHANNELING | 2-6 |
| 2.3 DISPERSION | 2-7 |
| 2.4 FRACTURE SURFACE EFFECTS | 2-9 |
| 2.5 JOINT HYDRAULIC CONDUCTIVITY UNDER STRESS | 2-10 |
| 2.5.1 Flow Experiments Under Normal Stress | 2-11 |
| 2.5.2 Applicability of Cubic Law to Deformable Joints | 2-13 |
| 2.5.3 Flow Experiments Under Shear Stress | 2-14 |
| 2.6 TYPES OF APERTURE ESTIMATES | 2-17 |
| 2.7 TORTUOSITY EFFECT | 2-19 |
| 2.8 RELATIVE PERMEABILITY | 2-20 |
| 2.9 MODELS RELATING STRESS-DEFORMATION AND HYDRAULIC PROPERTIES | 2-21 |
| 3 JOINT PROFILE MEASUREMENT | 3-1 |
| 3.1 LASER SCANNING PROFILOMETER | 3-1 |
| 3.2 CONTROLLING AND OPERATING PROGRAM | 3-2 |
| 3.3 FUNDAMENTAL OPERATING PROCEDURE | 3-4 |
| 4 APPARATUS AND PROCEDURE | 4-1 |
| 4.1 BASIC APPARATUS | 4-1 |
| 4.2 MODIFICATION TO ENHANCED DIRECT SHEAR TEST APPARATUS | 4-1 |
| 4.3 APPARATUS FOR AUXILIARY EXPERIMENTS | 4-5 |
| 4.3.1 Theory | 4-5 |
| 4.3.1.1 Mean Fracture Aperture | 4-5 |
| 4.3.1.2 Fracture Permeability | 4-6 |
| 4.3.2 Sample Selection, Test Cell, and Preparation | 4-6 |
| 4.3.2.1 Sample Selection | 4-6 |
| 4.3.2.2 Sample Test Cell | 4-7 |
| 4.3.2.3 Saturation Process | 4-8 |
| 4.3.3 Experimental Apparatus and Procedures | 4-8 |
| 4.3.3.1 Aperture Volume Measurement | 4-8 |
| 4.3.3.2 Liquid-Saturated Fracture Flow Experimental Apparatus and Procedures | 4-12 |
| 4.3.3.3 Pneumatic Fracture Flow Experimental Apparatus | 4-13 |

CONTENTS Cont'd)

| Section | Page |
|--|--|
| 5 RESULTS AND DISCUSSION | 5-1 |
| 5.1 RESULTS FROM AUXILIARY EXPERIMENTS | 5-1 |
| 5.1.1 Liquid and Gas Fracture Flow Test Results | 5-1 |
| 5.1.2 Effect of Forced Splitting of Fractured Specimen on Permeability | 5-6 |
| 5.2 ANALYSIS OF APERTURE DATA | 5-8 |
| 5.2.1 Analysis of Apache Leap Tuff Profile Data | 5-8 |
| 5.2.2 Effective Aperture Determination | 5-13 |
| 6 SUMMARY | 6-1 |
| 7 REFERENCES | 7-1 |
| APPENDIX A | Pressure Differential Measurements for Forward and Reverse Liquid Flow Experiments |
| APPENDIX B | Ramp Up and Ramp Down Tests in the Forward and Reverse Flow Directions |

FIGURES

| Figure | Page |
|---|------|
| 2-1 Chart showing the flow regimes in which various flow laws are valid (Louis, 1969) | 2-4 |
| 2-2 Exit face of a single natural fracture in a large granite block showing locations of maximum flow in a nonrestricted flow regime (Gureghian et al., 1990) | 2-8 |
| 2-3 Relationship between flow rate and effective stress in a horizontal saw-cut fracture (97×180 cm granite cylinder). Fracture closing is also prevented in the axis (Gale, 1975). | 2-12 |
| 2-4 Variation in flow through a finely fissured micashist under the effects of normal stress (Jouanna, 1972) | 2-16 |
| 2-5 Effective fracture aperture determined from various methods. The circle represents the effective aperture value and lines represent one standard deviation (Rasmussen, 1995). | 2-20 |
| 2-6 Schematic demonstrating the concept of tortuosity in 2D flow: (a) represents when tortuosity is absent, and (b) represents its presence | 2-21 |
| 2-7 Typical relative permeability versus water saturation curve for a water-air system | 2-22 |
| 2-8 Typical relative permeability versus matric potential curve for a water-air system | 2-22 |
| | |
| 3-1 Photograph of the laser-scanning profilometer along with the controlling and data acquisition system | 3-2 |
| 3-2 Top layout of the laser profiles showing the scan parameters | 3-3 |
| 3-3 Schematic of a joint specimen ready for profilometry. Sides are identified and the corner heights are indicated. | 3-5 |
| 3-4 Histogram of profilometer data collected from the surface of an aluminum block used in determining the reference height. This figure depicts the level of noise that could be expected in the data. | 3-6 |
| | |
| 4-1 Joint normal stress versus joint closure: (a) with basic apparatus, and (b) with apparatus enhanced for flow experiment | 4-2 |
| 4-2 Numerical dilatancy prediction from measured joint surface profile | 4-3 |
| 4-3 Elevation and plan view of the modified grout box. 90° brackets on four corners are designed to ensure the position of the two blocks under matched condition of the fracture surfaces. | 4-4 |
| 4-4 Schematic of sample test cell | 4-7 |
| 4-5 Schematic of inflow manifold | 4-9 |
| 4-6 Schematic of positive pressure experimental apparatus used to measure aperture volume | 4-10 |
| 4-7 Schematic of vacuum experimental apparatus used to measure aperture volume | 4-11 |
| 4-8 Schematic of liquid saturated fracture flow experimental apparatus | 4-14 |
| 4-9 Schematic of pneumatic fracture flow experimental apparatus using a constant area flowmeter | 4-15 |
| 4-10 Schematic of pneumatic fracture flow experimental apparatus using a J&W scientific flowmeter | 4-16 |
| | |
| 5-1 Steady-state flow rate versus pressure differential across the fracture during forward and reverse water flow | 5-3 |
| 5-2 Water flow rate versus pressure differential across the fracture with respect to a constantly increasing flow rate | 5-4 |
| 5-3 Steady-state flow rate versus pressure differential across the fracture | 5-5 |

FIGURES (Cont'd)

| Figure | Page |
|--|------|
| 5-4 Flow rate versus pressure drop across a fracture at low confining pressures varying between 30 and 90 psi for an unsplit natural fracture | 5-7 |
| 5-5 Flowrate versus pressure drop across a fracture at low confining pressures varying between 30 and 90 psi for a split natural fracture | 5-7 |
| 5-6 Photograph of the four vertical sides of a single rock mass (40×40×25 mm) containing a single fracture | 5-10 |
| 5-7 Surface heights data collected from the two faces of a fractured rock | 5-11 |
| 5-8 Sparsely distributed contact points between the two surfaces of the rock joint | 5-12 |
| 5-9 Histogram of joint aperture distribution presented in Figure 5-7 | 5-14 |
| 5-10 Semivariogram plot of the fracture aperture data showing stationary correlation length . . . | 5-14 |
| 5-11 Aperture distribution showing rock chip-off which could potentially distort the aperture statistics. | 5-15 |
| 5-12 Sequence of the figures showing the geometric configuration of contact area at various interpenetration of the two faces of the fractured rock | 5-16 |
| 5-13 Aperture distribution of ALT under simulated no-load joint dilation | 5-17 |
| 5-14 Histogram of aperture distribution corresponding to Figure 5-13 | 5-17 |
| 5-15 Aperture distribution of ALT under simulated no-load joint dilation | 5-18 |
| 5-16 Histogram of aperture distribution corresponding to Figure 5-15 | 5-18 |
| 5-17 Aperture distribution of ALT under simulated no-load joint dilation | 5-19 |
| 5-18 Histogram of aperture distribution corresponding to Figure 5-17 | 5-19 |
| 5-19 Fracture surface height data of a vertical cross section along the x-direction | 5-20 |
| 5-20 Idealization of the fracture face as a network of parallel plates | 5-20 |
| 5-21 Imposed boundary condition for numerically determining the effective aperture of a given aperture field | 5-21 |
| 5-22 Flux field superimposed on the corresponding aperture field | 5-22 |
| 5-23 Zoomed portion of the flux field from Figure 5-22 to highlight channeling effect conforming to the pattern of heterogeneity in the aperture field | 5-23 |
| 5-24 Effect of artificial joint dilation on the fracture permeability at various shear displacement under negligible normal-stress condition | 5-25 |
| 5-25 Flow rates presented as a function of head losses in a fully matched (mated) condition and at a specified shear under negligible normal load (Piggott and Elsworth, 1990) | 5-25 |

TABLES

| Table | Page |
|---|------|
| 2-1 Hydraulic conductivity and degree of nonlinearity at different flow regimes | 2-5 |
| 5-1 Pycnometer pressure and volume data | 5-2 |
| 5-2 Fracture permeability (m^2) calculated from gas and liquid flow tests | 5-6 |

ACKNOWLEDGMENTS

This report was prepared to document work performed by the Center for Nuclear Waste Regulatory Analyses (CNWRA) for the Nuclear Regulatory Commission (NRC) under Contract No. NRC-02-93-005. The activities reported here were performed on behalf of the NRC Office of Nuclear Regulatory Research, Division of Regulatory Applications. The report is an independent product of the CNWRA and does not necessarily reflect the views or regulatory position of the NRC.

The authors would like to thank R.G. Baca and R.D. Manteufel for the technical review and B. Sagar for the programmatic review of the report. One of the authors is greatly indebted to A.M. Pickens of Southwest Research Institute (SwRI) for his assistance in data acquisition and in preparing design drawings for modifying the shear test apparatus. This author also thanks D.D. Kana of SwRI for his continuing technical support in designing the shear test apparatus. R. Montoya, a student assistant (UTSA), conducted most of the apparatus testing and repeatability testing activities for the auxiliary experiment. The authors are thankful to C. Garcia, M. Gruhlke, Y. Lozano, E. Cantu, R. Sanchez, and A. Ramos for skillful typing of the report. C. Gray provided expert editorial services in the preparation of this document.

QUALITY OF DATA, ANALYSES, AND CODE DEVELOPMENT

DATA: All CNWRA-generated original data contained in this report meet quality assurance requirements described in the CNWRA Quality Assurance Manual. Sources for other data should be consulted for determining the level of quality for those data.

ANALYSES AND CODES: SMNETWORK.F and SMAPRT.F computational software were used for analyses contained in this report. These computational software fall under the categories covered by QAP-014, Documentation and Verification of Routine Calculations. Calculations presented in this report were checked as required by QAP-014 and recorded in a scientific notebook.

EXECUTIVE SUMMARY

Thermal, mechanical, and hydrological (TMH) interactions in fractured media are being addressed at the Center for Nuclear Waste Regulatory Analyses (CNWRA) and the Nuclear Regulatory Commission (NRC) through: (i) participating in modeling activities within the international cooperative project DECOVALEX (acronym for the **DE**velopment of **CO**upled models and their **VAL**idation against **EX**periments in nuclear waste isolation); (ii) performing coupled TMH laboratory experiments; and (iii) conducting additional model validation and code verification work for the development of compliance determination method (CDM) codes. The coupled TMH laboratory experiments are aimed at understanding the key parameters affecting the mechanical-effect-dependent fracture flow while simultaneously providing a database that can be used for evaluating current capabilities for calculating such fracture flow. Prior to coupling all the three processes, isothermal mechanical-hydrological (MH) coupled process experiments are under way, the current progress of which is documented in this report. During FY94, limited experiments were conducted to study the effects of normal and shear loads on the fracture flow, using single-jointed Apache Leap tuff specimen (Mohanty et al., 1994). In conducting these experiments, needs have been identified to modify the MH experiment apparatus as well as to conduct some basic laboratory and numerical experimentation studies that will enhance the design of the MH experiments.

The FY95 activities reported herein include a literature review on fracture flow, modification of MH experiment apparatus, experimental determination of fracture volume and fracture absolute permeability, numerical determination of fracture aperture from fracture profile data, and the effect of disturbing the rock joint from its naturally occurring condition on the fracture permeability.

The literature review on single- and multiphase fluid flow in a single fracture under stressed and nonstressed condition provided the state-of-the-art information on fracture flow. The literature provided evidences of channel flow based on field and large-scale laboratory tests. A change in the path of flow channels and a reduction in permeability by as much as a factor of three under compressive stress have been observed in tunnels. The application of the cubic law used in representing fracture flow appears to be questionable with increasing fracture surface roughness and with increasing normal stress. It has been recognized by many investigators that turbulence and kinetic effects are distinct possibilities at high flow rates. However, the development of techniques for data interpretation in this flow regime is very limited. No reasonable model based on experimental data was found which relates shear displacement and fracture conductivity. No experimental data on unsaturated or relative fracture permeability to water and air under shear stress were found in the literature.

The apparatus for conducting MH experiments with emphasis on fracture flow was modified to address the deficiencies identified by Mohanty et al. (1994). This modified apparatus along with the techniques developed for determination of fracture volume, fracture absolute permeability, and fracture aperture is suitable for conducting saturated/unsaturated fracture flow experiments under normal and shear loads.

For establishing fracture volume measurement method, the pycnometer method was adapted. The average of six-fracture volume measurements was determined to be $5.01 \times 10^{-4} \text{ m}^3$. This corresponded to an average fracture aperture of $1.2 \times 10^{-3} \text{ m}$. Fracture permeability to gas was found to be three to four times greater than the fracture permeability to liquid. The fracture permeability values from flow experiments were

found to be nearly a hundred times smaller than the permeability estimated using the arithmetic mean fracture aperture obtained from the pycnometer method and the cubic law.

For studying the effect of disturbing the naturally occurring condition of a fracture on the fracture permeability, a specimen was carefully selected from a larger field sample of Apache Leap tuff in which the two surfaces of the fracture appeared to have been held together by cementitious material. Flow tests were conducted before and after splitting the joint. Measurements revealed an order of magnitude increase in permeability after splitting the specimen. In order to test this, a specimen was carefully drilled from a large field sample of Apache Leap tuff. No definitive effect of confining pressure on the fracture permeability was observed at low confining pressures at which the experiments were conducted.

Difficulties were experienced in calculating correct aperture values from the surface profile data. The profilometer was modified, recalibrated, and a procedure was developed for calculating aperture values from surface profile data. It appears that, in spite of the strong heterogeneity in fracture profile data, the corresponding aperture distribution does not display such strong heterogeneity. Although the aperture configuration carries a signature of the heterogeneity in the surface profile, it does not show the strong correlation and anisotropy as seen in the latter. However, further studies are needed using more specimens of different sizes. The aperture distribution measurements of an Apache Leap tuff specimen with induced fracture showed approximately log-normal distribution of the aperture. A mean aperture value of 0.21 mm and a standard deviation of 0.14 was observed; the maximum and minimum values were 1.59 and 0 mm. Isotropic correlation of aperture distribution was found for the Apache Leap tuff specimen which was about one-sixth of the system length. It should be kept in mind that the joint specimen collected from the field may show a different geometric description compared to a fresh fracture created at the CNWRA laboratory. Fractures collected from the field as well as laboratory-created fresh fractures most often show weak spots on the fracture faces from which the rock materials easily chip off. Some of the large apertures in the aperture distribution may correspond to a few such areas from where rock may have chipped off. If chipping is present in a larger proportion, then the fracture properties measured from laboratory-scale experiments may be incorrect and misleading when applied at a larger scale.

The fracture profile data measured by using a noncontacting laser profilometer was used in numerical exercises designed for studying the rock dilation under shear displacement. From the numerical rock dilation studies, it was observed that the maximum change in the largest aperture value took place at the beginning of the displacement and then the change rapidly slowed down. With a final mean aperture value of 1.8 mm, the change in mean aperture at the corresponding displacement was observed to be 7.6 times that of the original mean aperture. Similarly, the change in standard deviation with respect to the matched condition was found to be nearly 2.5 times. The aperture distribution deviated from log-normal and tended to gaussian with increasing displacement. At larger shear displacements, a shift from unimodal to bimodal aperture distribution may take place. While the aperture distribution in a matched condition appeared to be isotropic, the displacement tended to develop large aperture streaks which might potentially contribute to the growth of an anisotropic flow path, such as flow channels.

Permeabilities were numerically estimated at various shear displacements. At zero horizontal displacement (i.e., fully matched condition), the equivalent permeabilities in the x- and y-directions were essentially identical, suggesting isotropicity in the aperture field. As dilation occurred due to shear displacement, the permeability increased in a nonlinear fashion, with y-directional permeability rising more rapidly than the x-directional permeability. The permeability curves may be indicating development of anisotropy with

larger displacement. A sudden increase in permeability was observed during shear displacement which may confirm the two distinct scales of heterogeneity inferred from the aperture distribution data. A 13-fold increase in the equivalent fracture conductivity has been observed as a result of 2.4 mm of numerical shear displacement.

1 INTRODUCTION

1.1 BACKGROUND

Yucca Mountain (YM), located approximately 160 km northwest of Las Vegas, Nevada, has been designated by the U.S. Congress for characterization as a potential repository site for high-level nuclear waste (HLW) disposal. The potential repository location is about 350 m below the ground surface and 225 m above the water table (Klavetter and Peters, 1986). Geologically, the repository horizon is a densely welded devitrified tuff, a zone that contains capillary water held tightly in pores of rock matrix, estimated at about 65 percent in saturation. Potential existence of perched water zones above the repository horizon has been suggested (U.S. Department of Energy, 1988). If a repository is constructed at this site, the construction activities are expected to change the stress conditions around the underground opening, thus disturbing the vicinity of the opening. The emplaced waste will generate heat that will cause the temperature of the rock mass around the emplacement areas to rise and will alter the hydrologic condition around the emplacement area. The raised temperature will also change the stress field in the repository area. Simultaneous occurrence of all these processes will result in coupled thermal, mechanical, hydrological, and chemical (TMHC) processes in the perturbed zone at the YM site. It has been argued (Buscheck and Nitao, 1993) that, at YM, fracture flow may be the most likely means for condensate to flow back toward the waste packages since the matrix permeability of the TSw2 unit is extremely low to the extent that the matrix flow in the near field is of little concern to repository performance. In this condition, the fracture flow could persist for a long distance before the condensate is revaporized or imbibed into the rock matrix. It would, therefore, appear that the extent of dry-out zone, the amount of condensate available above the emplacement areas, the infiltration due to rainfall, the hydrological properties of fractures, vapor flow under the buoyant pressure, etc., are the predominant factors that may determine the hydrologic conditions at the repository.

The hydrological properties of fractures will be perturbed due to the construction of the repository caused by the normal and shear displacements on fractures (Kana et al., 1991). Fracture normal and shear deformations will not only have implications regarding the stability of excavations but will also affect fluid flow and solute transport in the rock mass through changes in fracture aperture. Second, the heat generated from the emplaced waste could induce rock expansion, that in turn will cause fracture dilation, closure, and shear failure of fractures, leading to changes in the hydrological properties of fractures. Third, dynamic ground motions, including the cumulative effect of repetitive seismic motions (Hsiung et al., 1992a,b; Kana et al., 1995) could cause further dilation, closure, and shear of fractures. Hydrologic changes due to earthquakes have been observed in connection with several earthquakes (e.g., Ofoegbu et al., 1995). Recent observations (Hill et al., 1993) that a large earthquake can induce smaller earthquakes at great distances from its epicenter make this concern much more significant to repository design and performance assessment than previously thought. The cumulative effects of repetitive seismic loads may form preferential pathways connecting the emplacement area with the condensation zones above the emplacement area or perched water zones that could increase significantly the chance for water to contact waste packages. Laboratory data presented by Althaus et al. (1994) suggest that pressure in the rock matrix may weaken the rock enough to increase the likelihood for microfracturing. The occurrence of microfracturing may cause considerable increase in the rock-mass permeability. However, it is not yet clear if such changes in rock-mass permeability may significantly affect the performance of the proposed repository. In addition to the coupled thermal-mechanical-hydrological (TMH) interactions discussed above, there is also the concern of chemical coupling with the flow field. This coupling may be related to the precipitation or dissolution of minerals, which will either decrease or increase the permeability of

the fracture network (Lin and Daily, 1989; de Marsily, 1987). However, the effect of chemical reactions on TMH processes, and vice versa, was not considered in this study. The effect of chemical reactions on TMH processes, and vice versa, will be considered at a later date, if appropriate.

The U.S. Department of Energy (DOE) has been pursuing activities in order to understand the rock mechanics aspects of very-near-field (canister scale), near-field (room scale), and far-field (site scale) effects on the geologic isolation of the radionuclides. The DOE has recently suggested that fractures and variations in rock properties appear to be an advantage rather than a problem, thus emphasizing fracture flow (U.S. Department of Energy, 1994). Observations in tunnels similar to those that may be constructed for a repository suggest that water will be able to contact only a small fraction of waste packages, because water infiltration may be only local due to the fractures, thus potentially limiting waste package failures and total releases from the repository.

Recognizing the importance of coupled processes on the long-term behavior of the repository, the DOE is engaged in conducting laboratory tests, field tests, and numerical modeling. The laboratory tests are expected to support modeling studies and field tests. The DOE has planned to perform tests to investigate the long-term time-dependent behavior of fractures at above ambient temperatures and to perform tests to investigate the instantaneous effect of elevated temperatures on the properties of fractures. At a larger scale, the DOE has proposed testing thermal and mechanical properties *in situ* before conducting *in situ* coupled TM tests in the Exploratory Studies Facility (ESF). The DOE has planned to conduct large block tests (LBTs) toward determining the dominant heat transfer mechanism, monitoring dry-out zone, condensate refluxing, and draining rewetting at the end of the boiling period. The DOE will measure various rock and flow properties using small blocks collected during preparation of the LBT. Simulation results will be compared with the actual measurements to evaluate the adequacy of the numerical models. Laboratory experiments using small blocks include determination of rock properties, testing of TM, thermal-hydrological (TH), and thermal-chemical (TC) processes. In addition, mechanical-hydrological coupling has been pursued through experiments and modeling. The main emphasis has been the coupling through fracture aperture parameters (Blair, 1994). The need for coupling geomechanics codes with hydrologic codes (thermal field, flow parameters), and geochemical codes (rock material properties) has been identified. The DOE also anticipates that detailed coupling will be necessary in the future to estimate time dependence of local stress and displacement fields in fractured rock and to estimate the nature and location of rock damage zones.

To address the issue of thermomechanical-effect-dependent fluid flow through fractures, that is coupled TMH interactions on fracture flow in the rock mass surrounding the engineered barrier system (EBS), the Nuclear Regulatory Commission (NRC) and Center for Nuclear Waste Regulatory Analyses (CNWRA) have undertaken a program of developmental technical work on coupled TMH processes (Manteufel et al., 1993; Ahola et al., 1992, 1993, and 1994). This study on coupled TMH processes is being conducted through: (i) participating in the modeling activities within the international cooperative project DECOVALEX (acronym for the **DE**velopment of **CO**upled models and their **VA**lidation against **EX**periments in nuclear waste isolation); (ii) performing coupled TMH laboratory experiments; and (iii) conducting model validation and code verification for the development of compliance determination method (CDM) codes. The first and second activities are being conducted under the Rock Mechanics research project, and the third activity is being conducted under the Repository Design, Construction, and Operations (RDCO) subtask on Investigation of Issues Related to RDCO.

As a continuation of the DECOVALEX activities, the DECOVALEX task force has selected two large-scale *in situ* experiments for modeling. The purpose of these two test programs is to obtain input

data for verification of coupled TMH models and the associated computer codes. The first problem involves the predictive modeling of coupled MH processes associated with the NIREX Rock Characterization Facilities (RCF) Shaft Excavation at Sellafield, Cumbria, England. This will provide a scope for comparing the mechanical-hydrological (MH) numerical modeling results with actual observations obtained during shaft sinking. The second problem is the coupled Thermo-Hydro-Mechanical experiment at Kamaishi mine, conducted by the Power Reactor and Nuclear Fuel Development Corporation of Japan. This experiment is a part of the safety assessment of the near field. This includes assessment of coupled phenomena such as stability of the drift, groundwater flow around the repository, water seepage into the buffer material, occurrence of swelling pressure in buffer material, and the thermal effect.

The overall objectives of the coupled TMH laboratory experiments are to understand the key parameters affecting the mechanical-effect-dependent fracture flow and to provide a database that can be used to evaluate current capabilities for calculating such fracture flow. With the experience gained through participation in modeling the field-scale studies of DECOVALEX and through conducting laboratory-scale studies at the CNWRA, the NRC will be in a better position to critique the DOE near field test activities. In FY93, the coupled experimental program was initiated on an exploratory basis with the radial flow study of the MH coupled effects on a single-jointed Apache Leap tuff (ALT) specimen. In subsequent years, this program will be followed by selected two-process coupled experiments, and finally, coupled TMH experimental studies, possibly using a large rock mass containing multiple fractures. The objective of this report is to present a literature review and a progress report on the laboratory activities. In FY94, limited linear flow experiments have been conducted, to study the effects of normal and shear loads on the fracture flow, using single-jointed ALT specimen. The study reported herein is the continuation of these experimental activities.

1.2 SCOPE

The scope of work for this report relevant to coupled MH experiments (linear flow) on a single-jointed ALT specimen includes:

- Brief literature review on basic fracture flow and mechanical load dependent fracture flow
- Enhancement of experimental technique
- Characterization of rock joint interfaces
- Fracture volume measurements
- Qualitative study of the effect of rock dilation on flow
- Linear flow experiments under combined normal and shear loads

2 LITERATURE REVIEW

Rock mass in general shows structural heterogeneity as well as weaknesses at many scales including pore scales where they show up at the grain boundaries (Wang and Kemeny, 1994). At small scale such as core scale, heterogeneity and weaknesses show up as pre-existing cracks, and at larger scale they show up as joints, faults, bedding planes, etc. When subjected to loading conditions such as mechanical and thermal loading, these pre-existing natural discontinuities may close, open, slide, or induce crack growth, which not only may change the structure of the rock composite, but may also change the fluid flow properties of the rock mass. For example, a group of fractures or microcracks seemingly disconnected may become connected when the structure of rock composite changes and forms a pathway for fluid flow and radionuclide migration. This process could be further complicated in the presence of heat, that will not only contribute to the structural changes of the rock composite, but may also change the fluid flow scenario by adding multiple phases to the flow system and by changing the spatial fluid saturation distribution through evaporation and condensation. Therefore, understanding how water transmits in fractures is essential for evaluating the isolating characteristics of a particular waste isolation site. Insight into how specific pathways carry fluids through a fracture or a network of fractures under conditions of partial saturation is necessary to study the isolation characteristics of a site. A considerable effort has been expended by various investigators on single-phase and multiphase fracture flow under isothermal as well as nonisothermal conditions and under various stress conditions.

In the following sections, a brief but focused literature review is presented addressing some of the issues concerning the fluid flow in single fractures. No attempt has been made to summarize all research that have been conducted to date on fracture flow. The emphasis, however, has been given on presentation of some of the pertinent issues that are unique to fracture flow as well as the current attempts by various investigators to address those issues. Particular attempts have been made to review the studies by various investigators on mechanical stress-fluid flow coupled processes in fractures.

2.1 THEORY OF FLUID FLOW IN FRACTURES

The governing equations used in the fracture permeability measurements are based on the Navier Stokes equations (Lamb, 1932) from which Darcy's law (1856), an empirical equation for one-dimensional (1D) flow through porous media, may be derived:

$$Q = - \left[\frac{kA_f}{\mu L} (p_i - p_o) \right] \quad (2-1)$$

where:

- Q = volumetric flux, cm^3/s
- k = permeability, cm^2
- A_f = fracture cross-sectional area, cm^2
- p_i = inflow pressure, Pa
- p_o = outflow pressure, Pa
- L = length of fracture along flow direction, cm
- μ = dynamic viscosity of the test fluid, Pa-s

Darcy's law holds for macroscopic fracture flow according to the Navier-Stokes flow equations provided that inertial forces are negligible, the fluid is incompressible, and the flow is steady-state.

The cubic law may also be derived from the Navier Stokes equations. The cubic law is the simplest way to view volumetric flux for saturated laminar flow through parallel plates of very small width (Zimmerman and Bodvarsson, 1994). It is shown here for 1D flow in the horizontal direction.

$$Q = - \left[\frac{wb^3}{12\mu L} (p_i - p_o) \right] \quad (2-2)$$

where

- w = fracture cross-section width, cm
- b = mean fracture aperture width, cm.

Solving Eqs. (2-1) and (2-2) simultaneously for k leads to an expression for fracture permeability:

$$k = \frac{b^2}{12} \quad (2-3)$$

The cubic law is applicable only for homogeneous, incompressible fluids under isothermal conditions. It assumes that there is no slip flow at the boundaries (Klinkenburg effect), no surface friction, that the fracture is fully saturated, and that there is no flow channeling. It was soon recognized that the cubic law may be applied only to smooth fractures.

It appears that comprehensive work on studying flow characteristics in fractures began when Lomize (1951) conducted experiments using two narrow glass plates while studying the peculiarity of the boundary layer on the wall. He studied the effect of fracture aperture width by using two narrow glass plates 20 cm long and varying the aperture (gap between the two parallel plates) from 0.5 to 10 mm. Later, Romm (1966) conducted similar experiments by using smooth parallel optical plates and verified the validity of the cubic law for flow between parallel plates. Romm observed that the cubic law holds for apertures as small as 0.002 mm.

In order to study the effect of surface roughness on fracture flow, Lomize (1951) used different fracture shapes, as well as finer scale surface roughness. Later, Huitt (1956) and Parrish (1963) studied the similar wall-roughness effect on the flow using smaller systems and gluing glass beads or sand grains to the walls of the parallel plates. Baker (1955) and Louis (1969) used concrete material made of a sand and cement mixture to create surface roughness for their studies. Sharp (1970) had performed flow tests by using natural fractures in a hard granite porphyry with extremely low matrix permeability. Later, Rissler (1978) conducted experiments by machining surface roughness onto the plate surface. Most of these studies were conducted at various separations between the rough walls. In the case of Parrish's experiment, the two fracture walls were touching each other.

Experiments conducted by Louis (1969) suggested that flow of water in a single fracture of constant aperture, can be laminar or turbulent according to the Reynold's number defined as

$$R_e = \frac{2\rho bv}{\mu} \quad (2-4)$$

and the relative roughness k'/D_h , where

- ρ = the fluid density
- v = the fluid velocity
- b = the fracture aperture
- k' = the surface roughness
- D_h = the hydraulic aperture of the fracture which can be shown to be $2b$
- R_e = the Reynold's number

The critical Reynold's number ranges between 100 and 2,300 in which the transition takes place between laminar to turbulent flow. Based on the relationship between Reynold's number and friction factor, which is associated with energy losses in the fracture, Louis (1969) proposed different flow laws for different flow regions. The range of validity of these flow laws can be clearly seen in Figure 2-1. In this figure, the flow fields have been divided into five regions (regions I-V) corresponding to laminar flow versus turbulent flow and parallel versus nonparallel flow.

Louis observed that parallel plate assumption of fracture was valid for relative roughness k'/D_h less than 0.033, corresponding to $R_e=2,300$ where the transition takes place from the laminar flow (region I) to turbulent hydraulic smooth flow (region II). Transition from turbulent hydraulic smooth flow (region II) to turbulent completely rough flow is marked by the value of Reynold's number

$$R_e = 2.553 \left[\log \left(\frac{k'/D_h}{3.7} \right) \right]^{18} \quad (2-5)$$

This relationship is obtained by equating the friction factors (f) for regions II and III in Figure 2-1. At relative roughness k'/D_h greater than 0.033, parallel plate flow assumption is no longer valid, although the flow could still be laminar. This regime is represented in region IV. The transition from nonparallel laminar (region IV) to nonparallel turbulent flow (region V) is obtained once again by equating the friction factor associated with these two regions, which results in

$$R_e = 384 \left[1 + 8.8 \left(\frac{k'}{D_h} \right)^{1.5} \right] \left[\log \frac{k'/D_h}{1.9} \right]^2 \quad (2-6)$$

The solid lines separating various regions were obtained experimentally by Louis. The dotted lines represent the numerically obtained boundaries which do not coincide with the experimentally obtained boundaries for transition between regions IV and V and between regions II and III.

The flow velocity in regions (I-IV) in Figure 2-1 can be represented by

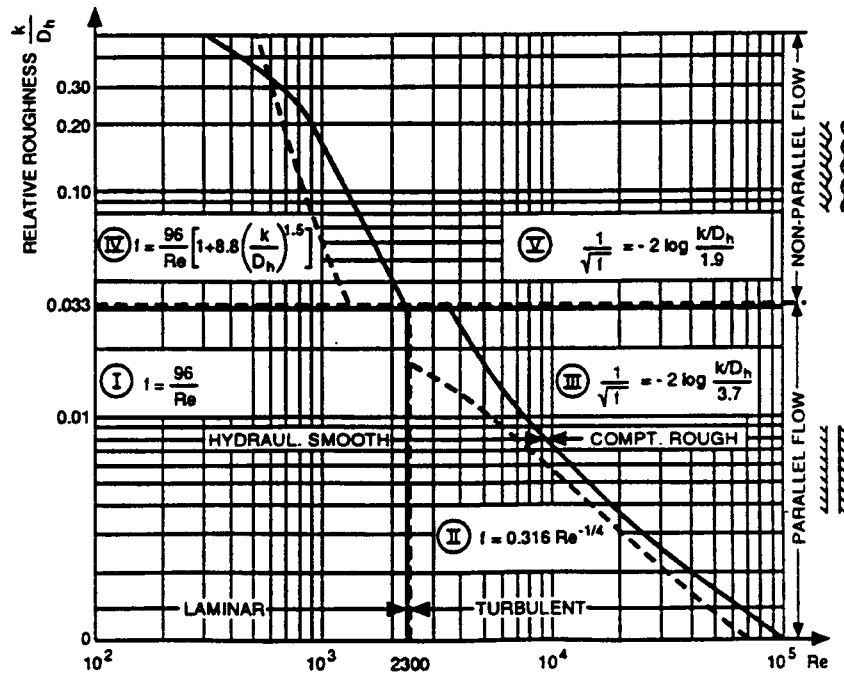


Figure 2-1. Chart showing the flow regimes in which various flow laws are valid (Louis, 1969)

$$v = Ki^\alpha \quad (2-7)$$

where v is the average velocity, i is the gradient in total head, K is the hydraulic conductivity, and α is an exponent. The above relationship can be rewritten as

$$v = K_T i \quad (2-8)$$

where

$$K_T = Ki^{\alpha-1} \quad (2-9)$$

K_T is, therefore, the constant of proportionality which depends on hydraulic gradient i unlike K . This implies that the nonlinearity in flow actually indicates nonlinearity in the transmissivity which becomes a function of the gradient. The fracture flow equation representing all these flow regimes, (i.e., α not equal to 1) is a nonlinear equation. For regions I and IV where flow is laminar, the fracture flow equation is simplified because K_T is independent of the gradient. Then the fracture flow is represented by a linear partial differential equation. On the other hand, in regions II, III, and V, the fracture flow equation is nonlinear. Expressions for hydraulic conductivity K_T and corresponding values of the exponent α for the linear and nonlinear flow regimes are presented in Table 2-1.

Amadei et al. (1995) have conducted numerical calculations and have observed that head distribution and velocity fields are different between laminar and turbulent flows. The flow rate through the fracture at a fixed pressure gradient is much less under turbulent flow.

Table 2-1. Hydraulic conductivity and degree of nonlinearity at different flow regimes (Louis, 1969)

| Hydraulic Region | Hydraulic Conductivity (K) | Exponent (α) | Flow Condition |
|------------------|--|-----------------------|----------------|
| I | $K_I = \frac{\rho g b^2}{12\mu}$ | 1.0 | Laminar |
| II | $K_{II} = \frac{1}{b} \left[\frac{g}{0.0079} \left(\frac{2\rho}{\mu} \right)^{0.25} b^3 \right]^{4/7}$ | 4/7 | Turbulent |
| III | $K_{III} = 4\sqrt{g} \log \left[\frac{3.7}{k'/D_h} \right] \sqrt{b}$ | 0.5 | Turbulent |
| IV | $K_{IV} = \frac{g b^2}{12 \frac{\mu}{\rho} [1 + 8.8(k'/D_h)^{1.5}]}$ | 1.0 | Laminar |
| V | $K_V = 4\sqrt{g} \log \left[\frac{1.9}{(k'/D_h)} \right] \sqrt{b}$ | 0.5 | Turbulent |

The relation between flow rate and hydraulic gradient is often assumed to be linear. This is true only for laminar flow at low velocities. The flow becomes nonlinear as the velocity increases. Nonlinearity implies that the flow rate is not directly proportional to the potential gradient.

Sharp and Maini (1972) proposed that the nonlinear laminar flow can be represented as

$$v = K \left[i - B(i - i_{lim})^n \right] \quad (2-10)$$

where i_{lim} is the limiting gradient for laminar flow and B and n are empirically determined constants. As they found that the relationship $Q \propto b^3$ is not always true, they proposed $Q \propto b^n$ where the following hold:

| Flow Type | Rough Discontinuity | Parallel Plate |
|-------------------|---------------------|----------------|
| Linear laminar | $n=2$ | $n=3$ |
| Nonlinear laminar | $1.2 < n < 2$ | — |
| Fully turbulent | $n=1.2$ | $n=1.5$ |

The nonlinear flow can be expressed by (i) Forchheimer's law, and (ii) Missbach's law. Forchheimer's law can be expressed by the polynomial expression

$$\nabla P = bv + cv^2 \quad (2-11)$$

where b and c are constants, P is the pressure or pressure head, and v is flow velocity in the direction of maximum gradient. In Missbach's law, which is represented as:

$$v = -k\nabla P^\alpha \quad (2-12)$$

k is the hydraulic conductivity of the discontinuity and α is equal to unity for laminar, and one half for turbulent flow in a rough-walled discontinuity. Equation (2-12) is linear until the onset of turbulence. Beyond this transition, the equation considers the contribution of kinetic head to the total head loss. In contrast, the Forchheimer's law considers a continuous function relating head loss and velocity.

A similar expression based on Missbach's law was presented by Maini (1971) which indicated that the relationship between flow rate and pressure drop may be nonlinear at lower hydraulic gradients. The form of the nonlinear law was presented as

$$v^n = C \frac{\partial P}{\partial x} \quad (2-13)$$

where v is mean velocity, exponent n represents the degree of nonlinearity, and C is a constant which depends on the viscosity of the fluid and the geometry of the discontinuity.

The nonlinearity may be a direct result of high velocity in the flowing fluid at which interference in flow might be taking place because of the inertial and kinetic effects associated with the higher flow velocities. The inertial effect is expressed through a ratio n which is the ratio between inertial loss and friction loss. For laminar flow, the inertial effect is significant for a convergent or a divergent flow at an injection point in a radial flow system. This effect can also be significant if the fissure is tapering in the direction of flow. At high velocities, kinetic effects could also dominate the flow field. At high velocities, increased flow occurs due to velocity head in addition to potential head. For flow in fissures, this effect could account for a significant portion of the total losses. Finally, it is not possible to separate the kinetic effect from the turbulent loss effect because both effects may be present simultaneously, although to different extents.

2.2 FLOW CHANNELING

The knowledge of the flow path is important for determining velocity as well as water saturation in single fractures and fracture networks. Downhole hydraulic measurements and tracer experiments performed at the Stripa mine as a part of the Swedish nuclear fuel and waste management program (Abelin et al., 1987) indicated that most of the fractures were closed and that most of the flowing fluid was carried by only a few intercepted channels. In the two-dimensional (2D) Stripa experiment, it was observed that 90 percent of the water was flowing into 5 out of 27 observation sites and dry sections often existed between the sections carrying water. Similar three-dimensional (3D) experiments indicated that 50 percent of the flow took place in about 3 percent of the observation sites.

A large block (91.5×86.5×49.0 cm) laboratory experiment was designed by Atomic Energy of Canada Limited (AECL) to understand the processes affecting the migration of a tracer in a single fracture. The test was carried out in the AECL laboratory in Canada using a natural fracture in a granite block with an estimated fracture aperture of 0.8 mm obtained from a surface quarry (Gureghian et al., 1990). In spite of the fact that the inlet covered the whole available cross section of the fracture, the injected water entered the fracture mainly at one location because the varying aperture did not allow for a uniform flow from the inlet of the reservoir; and this was evident from the post-experimental 2D gamma scanning of the fracture surface. Channeling was found to be a severe problem. Figure 2-2 shows the block experiment and illustrates that flow only occurred through a few channels.

From the previous two examples, it is evident that breakthrough of the radionuclides will take place earlier than would be expected considering a porous medium of equivalent hydraulic conductivity. Moreno and Tsang (1994) have indicated that even in unfractured porous media, a two or three orders of magnitude contrast in heterogeneity may result in considerable flow channeling and earlier radionuclide breakthrough than in an equivalent homogeneous medium.

Amadei et al. (1995) have suggested that when large pressure gradients are present, such as in preferential flow paths in a fracture due to the flow confinement, turbulence can have a major impact on flow and solute transport.

Microfractures that can hardly be visually detected appear to have significant effects on the transient moisture distribution (Russo and Reda, 1989). Significant air entrapment and hysteresis in a horizontal fracture saturated from the matrix has been observed by Glass and Norton (1992). Flow instability in gravity-driven flow results in downward growing fingers during infiltration events (Foltz et al., 1993). Differences in matrix saturation could occur potentially due to the channeling of water within the unsaturated fracture (Rasmussen, 1992).

2.3 DISPERSION

Determination of the amount of water moving in the fractured rock and the amount of dissolved species carried along with water requires the knowledge of water flow rate as well as the knowledge of the path through which water is flowing and the water velocity. The dissolved species, such as radionuclides, do not necessarily move at the water velocity. The velocity at which the radionuclides travel varies from the average water velocity because of the variations in water velocity and mixing of the different portions of the water (Neretnieks et al., 1987) contributing to some portions of nuclides moving faster and some slower than the average velocity. The effects are inherent in the definition of dispersion.

Keller et al. (1995) presented a method for predicting *a priori* the effective transmissivity and dispersivity to a fracture plane, given aperture distribution. Their measured single-fracture effective transmissivity was 13 percent larger than the estimated effective transmissivity whose aperture distribution was measured by computer tomography (CT) scanning. The measured effective dispersivity of 0.48 was 33 percent larger than the estimated dispersivity. Keller and others attributed the difference to the mixing at the inlet and outlet, lack of resolution of CT scan in capturing the heterogeneity adequately, incomplete development of dispersivity (model limitation), and errors associated with only first-order approximation in the model. They have suggested that these errors could be addressed by using mixing boundary conditions in the model, increasing the resolution of CT scanning, and using larger specimens to reduce the end effect.

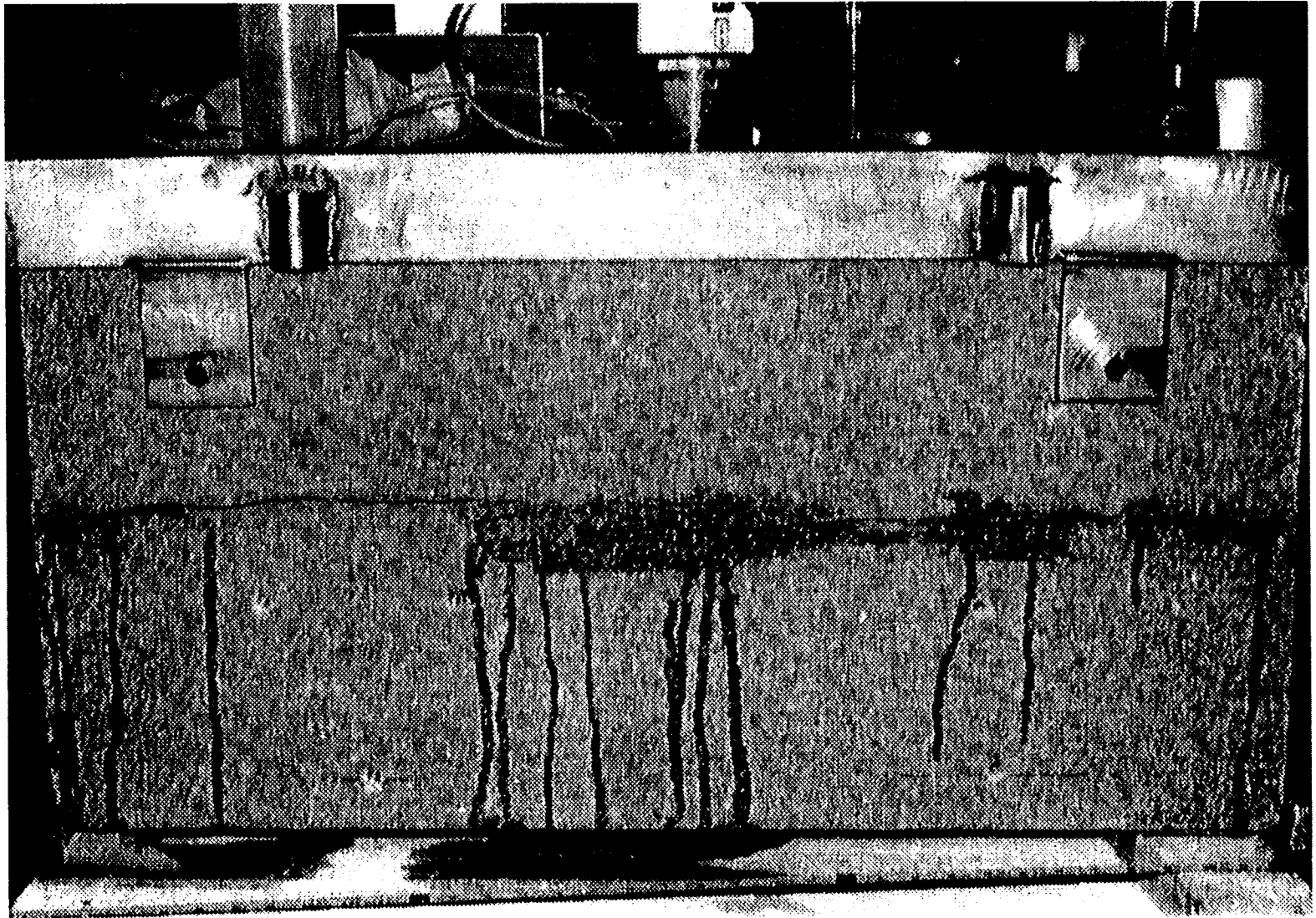


Figure 2-2. Exit face of a single natural fracture in a large granite block showing locations of maximum flow in a nonrestricted flow regime (Gureghian et al., 1990)

Hull et al. (1987) suggested that, for a nuclear waste repository, assumption of homogenization of solute front and complete mixing at the intersections of single fractures are reasonable assumptions. Because of the homogenization at low flow rates, the tracer transport can be treated in 1D instead of 2D. In rocks in which the fracture apertures may be on the order of microns, complete mixing will take place in fractures at velocities up to several meters per day.

2.4 FRACTURE SURFACE EFFECTS

The radionuclides may be absorbed at the fracture surface or may undergo ion exchange. Determination of the amount of dissolved species carried along with water requires the knowledge of radionuclide retardation due to fracture surface absorption and/or ion exchange. Such chemical processes will retard the radionuclides, sometimes many orders of magnitude slower than the water velocity.

In the models for radionuclide transport in a fractured rock, it is usually assumed that the velocity (v_x) of a radionuclide in a fracture is related to the water velocity (v_w) in the transport solution through a retardation factor R . The retardation factor is a function of the surface sorption coefficient K_a and the fracture aperture b which can be expressed as (Freeze and Cherry, 1979)

$$R = \frac{v_w}{v_x} = 1 + \frac{2K_a}{b} \quad (2-14)$$

The sorption coefficient is defined as the ratio between the amount of the radionuclide sorbed per unit area of the surface to the amount of contaminant per unit volume of the solution. Dimensionally, K_a is the reciprocal of the fracture aperture. At a specified flow rate, the retardation is larger if a large surface area is available for nuclides to interact. Such retardation is typically noted as an advantage, but in fracture flow, the surface area that the flowing water encounters is much less than in a porous medium. But if the inner surface of the rock mass embodying the fracture can be accessed through diffusion, then the retardation may increase considerably because of the much larger surface area available for the radionuclides to interact. Such a matrix diffusion effect could be a very important retardation mechanism.

A migration experiment typically could be performed by injecting conservative and nonconservative tracers. The conservative tracers can be used to monitor the velocity of the transport fluid whereas the nonconservative tracer could be used as a sorbed tracer in order to determine the surface sorption coefficient.

Factors such as stress in the rock and fluid flow conditions could impact the fracture surface effects on radionuclide transport. The rock stresses at the repository depth could reach nearly 20 to 30 MPa, which may be sufficient to decrease diffusivity in the rock matrix (Neretnieks, 1987a). The numerical calculations of Amadei et al. (1995) suggested that turbulence could slow down solute transport in fractures. It also affects apparent dispersion due to the fracture face heterogeneity.

Fracture coating could have impact on the matrix imbibition of fluid from the fracture (Gallegos et al., 1992). Fracture skin effect may occur as a result of mineral deposit formation on the fracture surface which are formed by the precipitation of minerals from the groundwater flowing along open fractures and by the deposition of detrital clay minerals and other substances transported from flowing groundwater (Sharp et al., 1995). The skin may reduce the diffusion process into the matrix (Moench, 1984; Smyth-Boulton and Sharp, 1994). The fracture coating could also be considered as a form of skin. Fracture

skin can significantly reduce the matrix imbibition of water flowing in the fractures because the fracture skin could have porosity, permeability diffusion coefficient, and sorptivity which could be different from the matrix properties. A porosity reduction by 4 percent (from 10 to 6 percent) and a permeability reduction from 1.919 to 0.273 md due to skin effect has been reported by Sharp et al. (1995).

2.5 JOINT HYDRAULIC CONDUCTIVITY UNDER STRESS

In recent years, a considerable effort has been made by many investigators (Bernaix, 1967, Gangi, 1978; Tsang and Witherspoon, 1981, 1983; Walsh, 1981; Barton, 1986; Gale et al., 1985; Pyrak-Nolte et al., 1987; Makurat et al., 1990) to understand the mechanics of flow through fractured rocks under stress conditions. While stress characteristics in most of these studies are based on the distribution of asperities, the stress dependent flow properties are based on the variable nature of the apertures in the rock joint. Field evidences of channel flow (Neretnieks, 1985, 1987b; Abelin et al., 1987) led investigators to approach the channeling problem from a variable aperture point of view for calculating flow and transport.

Nonreactive tracer studies (Neretnieks, 1987a; Abelin et al., 1987) have suggested that the tracer breakthrough is sensitive to applied normal stress. This may suggest that the flow channels in the joint may be drastically changing with the normal load. Using a high-pressure triaxial cell, Lai (1971) conducted experiments to determine permeability of salt under mean confining stress and octahedral shear stress. The triaxial cell allowed the axial load to be applied independent of the lateral confining pressure. Lai observed a change of permeability of six orders of magnitude over a range of confining pressure between 0 and 40 MPa. A field-scale permeability test at Stripa, Sweden (Wilson et al., 1983) extended over a 33-m-long section of a tunnel at about 340 m depth which had a fracture density of 2.9 to 4.5 joints/m. There was a reduction in permeability by a factor of three in a zone approximately 2.5-m-thick adjacent to the tunnel. Such reduction was attributed to compressive stress around the drift, chemical precipitation due to evaporation of water, and two-phase flow because of the gases coming out of the solution.

Elsworth and Goodman (1986) have presented simplified solutions for aperture changes due to post-peak shear strength deformations. Tsang and Tsang (1987) have pointed out that compression of joint surfaces under normal load proportionally reduces aperture width, the rate of reduction being much more in the small-aperture regions than in the large-aperture regions. Sometimes the aperture width may approach zero, thus diverting flow.

The fluid flow under shear stress is much more complicated than the fluid flow under normal stress. When the normal stress is low, shear displacement may cause the two rock surfaces to ride on each other due to shear strain, resulting in dilation of the fracture aperture. If the shear displacement takes place under high normal stresses or if the rock mass is a soft material, then shear force may deform and damage the asperities, thus changing the aperture distribution. The damage caused to the rock during forward shearing may alter the rock surface to the extent that the hysteresis effect may be observed during cyclic loading. Experimental, as well as theoretical, work has been pursued in this area to determine the magnitude of change in flow characteristics under shear load and also to establish empirical relationships for different materials and different normal stress conditions (Makurat and Barton, 1985; Barton, 1986; Makurat et al., 1990).

2.5.1 Flow Experiments Under Normal Stress

Many experiments have been conducted by various investigators to study the effect of normal load on fluid flow through a single fracture. These include Jones (1975), Gale (1975, 1982, 1984), Iwai (1976), Nelson and Handin (1977), Kranz et al. (1979), Engelder and Scholz (1981), Johnson (1983), Reda and Hadley (1985), and others. Normal stress of up to 200 MPa has been applied in some cases.

Snow (1968) studied the effect of stress on fracture flow in the context of water pressure tests at dam sites. Snow indicated that permeability and porosity of fractured rocks are a much stronger function of fluid pressure compared to intergranular porous media. From field tests, Snow found that fracture aperture varied between 0.1 to 0.2 mm with 10 m of ground surface and decreased to between 0.05 to 0.1 mm at depths greater than 100 m. Using finely fissured mica schist, Jouanna (1972) conducted field and laboratory experiments. From laboratory experiments under biaxial loads, Jouanna observed that the flow rate changes under various stress levels and the original flow rate is unrecoverable when the stress is removed. Using a triaxial testing machine, Ohnishi (1973) measured the effect of confining pressure on flow rates using a vertical fracture in Lyons sandstone. Ohnishi created surface roughness by sandblasting surfaces of interest. His experiments used an upstream pressure of 50 psi (0.34 MN/m²) and confining pressure up to 4,500 psi (31 MN/m²). Ohnishi also observed irreversibility in flow rates under repeated loading conditions. Louis (1974) used uniaxial and biaxial loading conditions to perform flow tests. He also observed that the hydraulic characteristics of the joint show hysteretic behavior under repeated loading. Gale (1975) performed a triaxial cell test by using a large granite core specimen 97 cm in diameter and 183 cm long. He used two different fracture types, of which one was a saw-cut, whereas the other fracture was a tension fracture. The fracture plane was perpendicular to the length of the cylindrical core. Using uniaxial loading and convergent radial flow configuration, he studied the effect of normal stress on flow characteristics of the fracture. Typical results from his experiment can be seen in Figure 2-3. Bernaix (1967, 1969), using a radial flow configuration, conducted a large-scale experiment and observed the difference between radially converging and radially diverging flow. As a part of an *in situ* rock testing program, Pratt et al. (1974) performed a field-permeability test on a vertical fracture under normal loading conditions. They observed that the flow rate decreases linearly with the increasing normal stress up to 1 MN/m². A further increase in load did not change the flow rate. Jones (1975), using a Hassler-type core holder, studied the effect of continuing pressure on fracture conductivity in carbonate rocks and observed a linear relationship between the logarithm of confining pressure and fracture permeability.

Somerton and others (1975) performed triaxial tests on coal by using a uniaxial load plus Hassler-type core holder. The finely jointed coal showed two orders of magnitude drop in the permeability as the compressive strength was increased from 1.5 to 15 MPa (Somerton et al., 1975). A decrease in permeability by a factor of four to five was observed in fractures in a large granite block when the effective normal stress acting across the joint was changed from 0.5 to 1.0 MPa (Gale, 1975). Similar stress dependency was observed in rocks containing microcracks (such as tight gas sand) in which the permeability showed large sensitivity to the change in overburden pressure (Brower and Morrow, 1985). Takahashi et al. (1991) measured permeability and volumetric strain of Shirahama sandstone and Inada granite under stress by using the transient pulse method which could measure permeability to a nanodarcy order. Takahashi and others observed a decrease in rock permeability under isotropic stress, and they attributed this to the pre-existing microcracks. They observed that under axial differential stress, the sample permeability increases as a result of the sample becoming more dilatant.

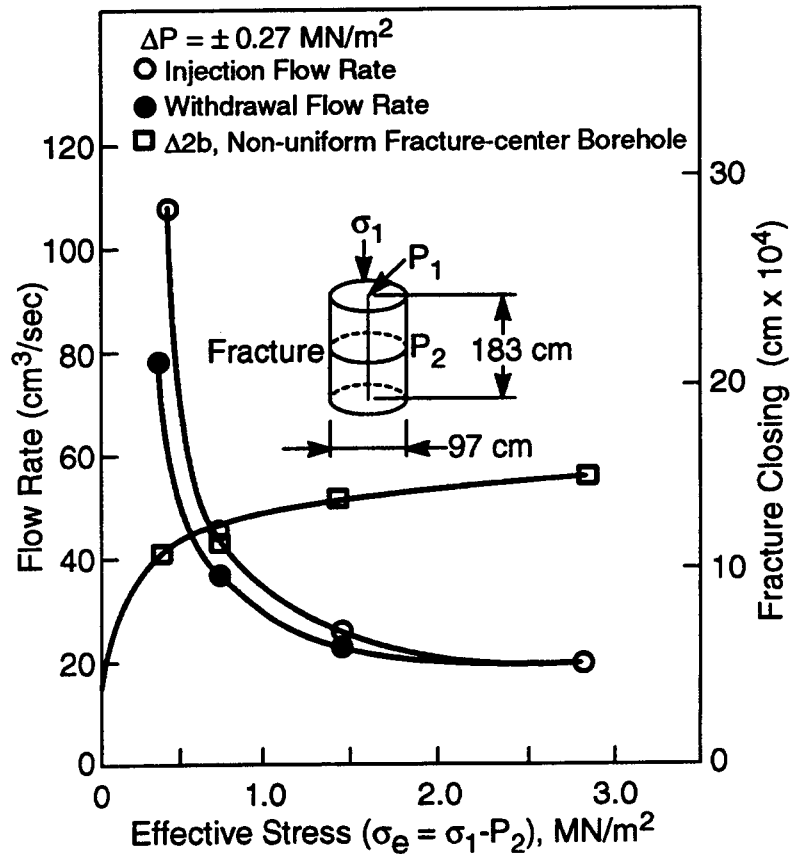


Figure 2-3. Relationship between flow rate and effective stress in a horizontal saw-cut fracture (97×180 cm granite cylinder). Fracture closing is also prevented in the axis (Gale, 1975).

While experimenting with fractures on three different rock types, Iwai (1976) observed that, for apertures greater than 2×10^{-3} cm, the fracture flow is not greatly influenced by the small-scale fracture surface roughness. He observed only a small effect of contact area on flow. He attributed larger contact area in the marble due to the low rock strength. Under uniaxial loading, while the stress deformation behavior of rock was nonlinear, the cyclic loading produced hysteresis and permanent set. But Iwai did not observe significant impact under cyclic loading in a basalt (extremely nonuniform fracture) sample which led him to believe that the initial fracture aperture cannot be uniquely defined. He also observed a small flow rate (residual flow) even at high normal stress (30 MN/m^2) which he attributed to small defects on the fracture surface, suggesting that, ideally, the fracture could completely close at higher normal stress.

Nelson and Handin (1977) conducted experimental studies of fracture permeability in porous rock by using Navajo sandstone. They observed that the fracture deformation under confining pressure is mostly inelastic, whereas the matrix deformation is substantially elastic. They have observed complete close-off of the fracture, thus fracture permeability approaching matrix permeability. They observed that change in fracture permeability with depth largely depends on the macroscopic ductility. They also found that change in permeability with depth is substantially permanent when pressure alone is applied, but elastic when temperature alone is applied.

2.5.2 Applicability of Cubic Law to Deformable Joints

Thorpe et al. (1983) observed that the measured closure of the discontinuities was greater than the equivalent aperture change calculated by assuming flow through a single parallel plate. Kranz et al. (1979), based on their experiments on smooth joints, suggested that additional parameters are needed to be included in the cubic law in order to account for stress history. Iwai (1976) showed that changes in aperture of a rough-walled discontinuity resulted in changes in flow rate as expected from the application of the cubic law. The validity of the cubic law was studied by Iwai (1976) under condition of no fracture contacts to the application of 20 MPa normal stress. The deviation from the cubic law was explained by Witherspoon et al. (1980), based on Iwai's data in terms of a friction loss parameter and expressed in terms of the Darcy-Weisbach friction factor. Engelder and Scholz (1981) used smooth joints and stress up to 200 MPa and observed experimentally a significant deviation from the cubic law. Similarly, Gale (1982) observed a significant deviation from the cubic law under increasing normal stress.

The nonapplicability of the cubic law to deformable natural fractures was indicated by Gale and Raven (1980). They attributed this to the significant changes in flow rates because of the changes in contact area due to the rock deformation. They obtained an exponent to fracture aperture b greater than 3 which increased with successive load cycles and increasing sample size. The cubic law was found not to be applicable to induced fractures under normal loads above 20 MN/m². In the natural discontinuities, breakdown occurred at lower normal stress, because of the more tortuosity in the flow path experienced in a natural joint compared to a joint with induced fracture. Tsang and Witherspoon (1985) indicated that neglecting the tortuosity could result in a two to three order of magnitude error in the flow rate at a given pressure differential. Tsang and Witherspoon (1981) also indicated that the parallel plate assumption holds for rock joints only at low applied stress.

Gale et al. (1985) concluded, based on the laboratory data, that applicability of the cubic law with appropriate corrections for roughness was limited to fractures with faces not contacting each other. Corrections for roughness only did not appear to adequately define the flow properties and tortuous flow paths in single fractures. They considered the inability to determine actual aperture geometry and flow properties for single fractures was a real limitation in determining true fluid velocities in fractures. This is expected to be even more complicated in case of multiple fractures systems, some of which may be completely discontinuous in nature.

Gale et al. (1985) reported that, at low normal stress and a given pressure differential across the fracture, the flow rate was observed to drop more rapidly than predicted by the cubic law. This implies that the hydraulic aperture changes much more rapidly than the measured fracture closure. They have also reported that at 10 to 15 MPa normal stress, the fracture aperture began to change more rapidly than the flow rate and the change in flow rate is the first power of the aperture. However, they observed a weak trend of decreasing fracture permeability with increasing sample size. Data from Gale (1984) indicated that the aperture versus flow rate relationship approached the cubic law rapidly as the sample size was increased. While conducting experiments at a larger scale (with a fracture perpendicular to the core axis), differences were observed between laboratory experiments and numerical models, even after nonlinearity in the flow laws had been taken into account. The discrepancy was attributed to the anisotropy effect being significant when the majority of the fracture area was in intimate contact.

The fluid flow rate can be two or more orders of magnitude smaller than predicted without accounting for the tortuosity. Based on the departure from this velocity, Gale et al. (1985) concluded that

correction for surface roughness alone was not sufficient to account for flow in a fracture with intimate contact, though it was found to be adequate when the fracture faces were not in contact with each other.

Brown (1987) showed a 20–30 percent lower actual flow rate compared to the flow rate expected from the parallel plate model for the range of joint closure expected during an elastic deformation.

Initial aperture, roughness, contact areas, or wall strength influences the flow rate and hydraulic conductivity in a fractured rock joint. Under normal stress, the contact area between fracture faces is a function of discontinuity surface roughness (Gale, 1987). The increase in contact area is usually associated with a resultant decrease in aperture which restricts the fluid flow through the noncontacting areas of the fracture. Establishing a relationship between fracture surface characteristics and fluid flow has been attempted by various investigators (Gale and Raven, 1980; Gale, 1982, 1987; Bandis et al., 1981). The focus in such research has mostly been on the effect of normal stress and very limited on the effect of shear stress.

2.5.3 Flow Experiments Under Shear Stress

Investigations on the effect of shear load on flow are rather limited. Fracture flow data under shear load have been collected by various investigators (Ohnishi, 1973; Maini and Hocking, 1977; Makurat and Barton, 1985; Tafel, 1987; Esaki et al., 1991; and Mohanty et al., 1994) by using three different laboratory techniques: (i) triaxial and biaxial shear, (ii) direct shear test, and (iii) rotary shear test. The rotary shear test has been used by Sandia National Laboratories to gather MH coupled process data for jointed rock masses. This technique has also been used by many other investigators to measure mechanical data (Christensen et al., 1974; Kutter, 1974; Blandpied et al., 1987; Olsson, 1987, Xu and Frieta, 1988). The technique requires a hollow cylindrical jointed rock mass specimen, in which the annular ring-like core is cut perpendicular to the joint. Shear load is applied by twisting both the hollow cylinders coaxially in the opposite direction under the imposed normal load. This design is particularly convenient for the imposition of normal and shear load where the normal load can be applied uniformly. The area of sliding interface also always remains constant and there is no limitation on the extent of shear displacement that can be achieved. The biggest limitation of the method, however, is the variation of slip velocity along the radius of the specimen at the joint surfaces (Price et al., 1994). In addition, for the MH coupled process experiment, the flow field changes along the radius, with the largest velocity occurring at the inner radius of the rock joint. Data interpretation can be difficult because the Reynold's number which is used in identifying the flow regimes could be different at the inner boundary and outer boundary of rock joint specimen. One approach to avoid such difficulty, which is purely because of the geometric configuration of the specimen, is to allow the inner radius of the specimen to be much larger than the thickness of the specimen in the radial direction. Unfortunately, this contributes to having less area of contacts between fracture faces.

The direct shear test method has the advantage that it accommodates measurement of the shear strengths of large rock samples. In this method, the shear and normal stresses are applied in a decoupled manner. Imposition of cyclic loading is particularly easy in this test method. It has been observed that it is difficult to maintain a uniform normal load, and thus the surface area of contact is characterized by change. There is a tendency for a turning moment, giving rise to difficulty in maintaining a uniform normal stress. Uniform elevated temperature is difficult to apply on a direct shear testing apparatus.

The triaxial compression test method is applicable only for small size cores. In this method, a cylindrical core with a fracture located near the center which makes approximately a 30° angle with the sample axis is used. The method requires a sample diameter that is typically smaller than the length of the specimen. When triaxial load is applied, the proper proportion between the axial load and confining load have to be maintained in order to impose desired normal load. The main advantage of this method is that it allows high normal load as the rock strength increases with the increase in confining pressure. The main disadvantage is that a large size rock cannot be accommodated. Secondly, a large slip or shear displacement cannot be attained.

Makurat and Barton (1985) used a biaxial cell to study the change in hydraulic properties of fractures under shear load. This apparatus accommodated a 15-cm-diameter core sample and allowed 0.5 cm maximum shear displacement under confining pressures up to 10 MPa. Taufel (1987) used a triaxial experimental apparatus for shear flow coupling test. Taufel's results showed that hydraulic conductivity across the fracture decreased with increasing shear deformation because of localized deformation along the fractures and the evolution of a gouge zone. Maini and Hocking (1977) used a direct shear test and showed a potential for two orders of magnitude change in conductivity with shear displacement. Esaki et al. (1991) have pointed out, as did Mohanty et al. (1994), that the above shear flow coupling tests do not adequately represent the condition of an actual fracture because of small shear displacement and/or low normal stress.

Esaki et al. (1991) conducted shear flow coupling tests using 8×10×12-cm granite specimens. Their apparatus had a shear loading capacity of up to 40 metric tons and normal loading capacity of up to 200 tons. The upper grout box allowed vertical movements and rotation while the lower box was restricted to horizontal movement. The setup allowed a maximum shear displacement of 2.0 cm. They conducted radial flow experiments by injecting water through a 6-mm-diameter hole drilled at the center of the lower part of the specimen. They used a shear displacement rate of 0.1 mm/s. It appears that the flow was continued while shear displacement was taking place. These investigators apparently assumed that steady-state could be reached instantaneously. Esaki et al. (1991) could create an artificial joint in an intact rock mass by using this apparatus. However, they had to create several saw cut slits (width 1 mm, depth 10 mm) at mid-height of the specimen to create an artificial joint correctly and easily. Their apparatus had a special arrangement for measuring acoustic emission characteristics of the joint during the shear-flow coupling test.

Using slate specimens, Maini (1971) conducted flow experiments under shear loading conditions. He observed two orders of magnitude increase in permeability during a shear displacement of 6 mm. This experiment potentially represented the effect of dilation due to shear in the absence of gouge production because the applied normal load was only due to the weight of the top block. Ohnishi (1973) also conducted an experiment to investigate the effect of shear displacement on fracture flow characteristics. Under a normal stress of 500 psi (3.45 MN/m²) and within a shear displacement of 5 mm, he observed a twofold increase in flow rate. Jouanna (1972), in his field experiment on micaceous schist rock, observed a decrease in flow rate with increasing shear stress. The effect of normal stress during shear displacement in Jouanna's experiment can be seen from Figure 2-4. This figure shows that, as the shear stress increases, dilation also significantly increases as long as constant normal stress is maintained across the fracture. But if normal stress is adjusted such that no dilation takes place, then a significantly higher shear stress is required to obtain the same amount of shear displacement.

When walls of the fractures are in contact, unlike the parallel plates where there is zero contact between the two surfaces, deviations from cubic law have been observed, even after the correction has

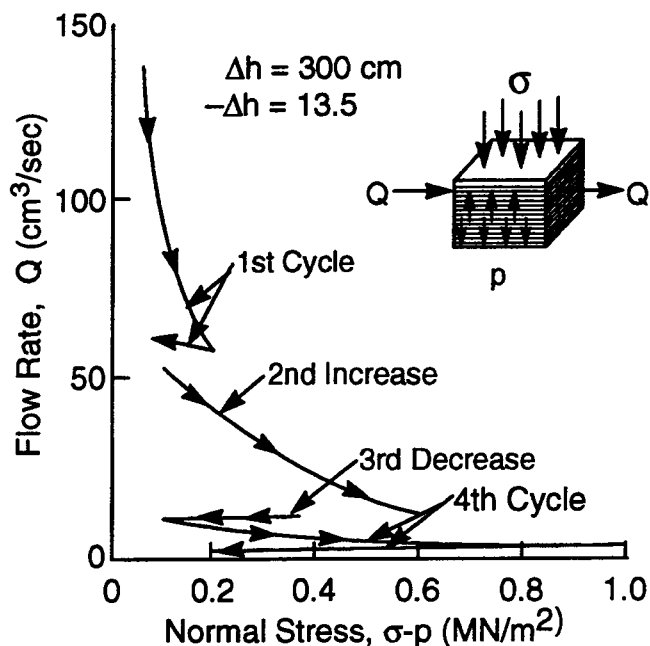


Figure 2-4. Variation in flow through a finely fissured micaschist under the effects of normal stress (Jouanna, 1972)

been made for the fracture surface roughness. Up to normal stress of 10 MPa or so, Gale et al. (1985) indicated that this pattern can be characterized by flow rate versus aperture relationships. Above 15 MPa, these relationships approach the first power. They have also indicated that accurate determination of aperture geometry and flow properties for single fractures may be the limiting factors in evaluating the velocities in fractured systems. Well-designed tracer tests associated with fracture network transport modeling were advocated for determining the fluid velocity distribution in fractured rock masses.

The distinction between small- and large-scale roughness has been made in the past based on the comparison of the size of the roughness to the fracture aperture. When the size of the protrusion from the fracture surface is the same order of magnitude as that of the flow channel, then the fracture is said to have large-scale roughness. Gale et al. (1985) have cautioned that care should be exercised in using the roughness equation presented by various investigators because of the apparent differences in the definition of basic variables, notably the use of hydraulic radius in the definition of Reynold's number. When the Reynold's number was expressed in terms of the Darcy-Weisbach friction factor (Parrish, 1963), then the onset of nonlinear flow, (i.e., deviation of Reynold's number versus friction factor) was observed at 80 for the relative roughness e of 1.0 and about 100 for e of 0.862, corresponding to the work of Romm (1966). At the relative roughness value of 1.0, the two fracture faces barely touch each other and the contact will increase when normal load is applied. Under the imposition of normal load, the asperity height would decrease as the aperture height decreases. If the aperture were inferred from the volume of fluid in the fracture plane (Lomize, 1951), then the aperture height would decrease more rapidly than the asperity height (Gale et al., 1985), reflecting larger relative roughness. No experiments are known to have been done in this area to pinpoint the effect of these factors on the flow behavior.

Piggot and Elsworth (1990) conducted experiments using a 190-mm-diameter and 320-mm-long granite specimen with the natural fracture parallel to the principal axis of the cylindrical specimen. An

average mimicked displacement of 2.39 mm was accomplished that resulted in an average normal displacement of 1.00 mm. Two series of tests were run. The first series was run under a fully mated condition. The second series of tests was run under a mimicked sheared state in which one side of the joint was manually displaced with respect to the second half normal to the axis of the core specimen. Only one mimicked shear displacement was considered. Piggot and Elsworth had conducted pneumatic tests, hydraulic tests, electrical tests, and tracer tests. They had found that the change in aperture from the mated condition to the sheared condition is substantially larger than as indicated by the transport tests. The aperture derived from the pneumatic and hydraulic tests compared well, but they differed from the aperture derived from electrical measurements. Similarly, the changes in aperture as derived from the volumetric, pneumatic, hydraulic, and tracer tests are larger than those derived from the electrical tests. Their tracer test experiments have suggested that the tracer transit time distributions are more uniform for the sheared condition than for the mated condition. They have recommended that additional experiments should be conducted in order to resolve the apparent discrepancy between hydraulic and electrical apertures.

2.6 TYPES OF APERTURE ESTIMATES

Fracture apertures have been determined in the past by using many different methods and apertures were significantly different for different methods. Neretnieks (1987a,b) has observed one to two orders of magnitude larger fracture opening than interpreted from pressure drop data. Gustaffson and Klockars (1982) observed, from their near-surface two-well test at Finnsjon with relatively large fractures, that the aperture derived from pressure drop and aperture derived from tracer residence time differed by a factor of six. Many such examples exist in the literature. Silliman (1989) published a theoretical paper addressing some of the discrepancies in aperture distribution estimates derived from hydraulic and tracer tests in a single fracture. Tsang (1992) also noted that the apparent discrepancy of the field results partly arise from how the aperture from a tracer test is derived or how it has been subsequently used by different researchers. Vandergraaf (1995) had drilled 11 boreholes into a block of granite (81×90×75 cm) with the fracture parallel to the 81×90-cm sides. Using a 2D well model (Chan and Nakka, 1995), Vandergraaf obtained the fracture aperture distribution. In spite of relative dense placing of boreholes for fracture hydraulic characterization, fracture asperity could not be uniquely determined. Therefore, he has suggested that alternate noninvasive techniques should be used to determine the aperture-width distribution of a fracture. Alternate approaches may include a replica approach (Persoff et al., 1991), profilometry approach, Wood's metal or epoxy injection approach, position emission tomography approach (Gilling et al., 1991), or fluorescent dye injection (Snow, 1970).

Mean fracture aperture (b_1) can be estimated by the pycnometer method which is traditionally used in measuring effective porosity of an intact porous rock. Mean aperture is obtained from the fracture volume and specimen dimension data. This method requires that the effective porosity of the rock should be determined separately, using a representative specimen, and the pore volume should be subtracted from the total volume to obtain the fracture volume. Additional descriptions of this measurement method will be presented in a subsequent chapter.

Fracture aperture can be obtained from fracture permeability when fluid flow is assumed to be smooth-walled. In that case, the transmissivity T can be calculated from (Rasmussen, 1992)

$$T = b_2 \frac{e_1^2}{12} \frac{\gamma}{\mu} \quad (2-15)$$

where b_2 , e , γ , and μ are “volumetric” aperture, “Poiseuille” aperture estimate, specific weight of manometer fluid, and fluid viscosity, respectively. For rough-walled fractures, the equation underestimates the volumetric aperture due to the inertial and friction effects (Rasmussen, 1992).

The equivalent aperture normally refers to the fracture aperture used in the cubic law which is defined by Eq. (2-2). It is the aperture between two parallel plates that would cause a pressure drop that would be caused by a rough fracture with all its details exposed to same steady-state pressure drop and flow rate. For the comparison purposes, this aperture is referred to as e_2 . The cubic law aperture has sometimes been considered as mean aperture (Neuzil and Tracy, 1981; Brown, 1984). It is also generally referred to as “hydraulic” aperture.

Another type of fracture aperture, interpreted from the mean residence time of a tracer during a tracer test, can be represented by

$$Qt_w = Ab_3 \quad (2-16)$$

where Q is the volumetric flowrate, t_w is the mean tracer residence time, A is the areal extent of the single fracture, and b_3 is the derived equivalent aperture. b_3 is derived from the mean residence time of the tracer particles, volumetric flow rates, and the area of the flow region. Therefore, b_3 depends only on the mass balance and is relevant to the fracture volume. Therefore, it relates to the arithmetic mean of all the fracture values in the tracer flow path. This has been verified by the numerical simulations of Moreno et al. (1988). This is referred to by some as tracer aperture. Smith et al. (1987) have referred to this as the volume balance aperture.

For tracer aperture, the mean residence time is determined from the time movement of the tracer breakthrough curve. When the tracer mean residence time t_w is represented in terms of velocity between injection and collection point, respectively, then a different definition for the fracture aperture evolves, and is referred to as “friction-loss” aperture. According to this definition, the velocity between the injection and production point in a linear flow configuration is constant. The “friction-loss” aperture

$$e_1 = L \left(\frac{12\mu}{\gamma |\Delta H| t_w} \right)^{\frac{1}{2}} \quad (2-17)$$

By definition, the “friction-loss” aperture is the smooth parallel plate aperture with terms accounting for the wall roughness. This aperture is determined from hydraulic head-loss measurements, length of flow path, and the measured tracer residence time from the tracer breakthrough curve. This has been referred to by Silliman (1989) and Smith et al. (1987) as the tracer aperture.

Another aperture, referred to as the “capillary” aperture by Rasmussen (1995), is the one that is related to the air entry pressure of a single fracture. The air entry pressure is the negative pressure head required to initiate draining a fully water saturated fracture. This can be represented as

$$C = \frac{2\sigma \cos\beta}{\gamma \Delta Z} \quad (2-18)$$

where C is the capillary aperture, σ is the interfacial tension between air and water, β is the contact angle at the air-water-solid interface, γ is the water specific weight, and ΔZ is the air-entry pressure head. On a highly wetting surface, the contact angle between the rock and the water can be assumed to be zero.

Rasmussen (1995) has plotted a comparison of all these distinct aperture estimates, which is presented in Figure 2-5. The pycnometer method (aperture b_1) and the tracer experiments (aperture b_3) gave similar values for apertures. The aperture determined from the tracer velocities (aperture e_1) was much smaller than the previous two. Aperture b_2 is significantly smaller than b_1 and b_3 . An aperture estimated from the permeability calculation was much smaller than b_1 , b_2 , and b_3 . The aperture derived from the capillary pressure data gave the smallest aperture value.

2.7 TORTUOSITY EFFECT

Tortuosity has been argued to have a strong effect on discharge (Tsang and Witherspoon, 1985). If not considered in the model application, a substantial error would result in the effective fracture conductivity determination. The significance of tortuous flow characteristics is that a gradient applied in one direction may induce flow in a direction nonparallel to the orientation of the maximum global gradient (Elsworth and Goodman, 1986).

For purely longitudinal flow across the described profile, the weighted average cubic fracture aperture (b) may be given by

$$\frac{\sum_j a_j b_j^3}{\sum_j a_j} = \langle b^3 \rangle_{x_{1,0}} \quad (2-19)$$

Here a_j represents incremental step widths and b_j represents apertures. When all pixels are of equal length and width, Eq. (2-19) reduces to an arithmetic average as has been presented before as the mean aperture value. Such averaging implies that there is no variation in the aperture in the x-direction, and therefore the aperture field in terms of fluid conductance can be presented as shown in Figure 2-6a. This figure shows an electrical conductance representation of the fluid conductance of the fracture apertures. However, the geometric positioning intuitively must influence the flow path. In order to take this into account, the aperture field is represented as fluid conductance distribution as shown in Figure 2-6b. The major shortcoming in using arithmetic average of aperture width is that it does not capture the tortuosity in flow path.

The effect of tortuosity decreases as the aperture distribution approaches a delta function representing a condition of all apertures being of approximately the same size. In that case, the streamlines are almost perpendicular to the potential lines, in which case the conductivity can be approximated as proportional to $\langle b^3 \rangle$.

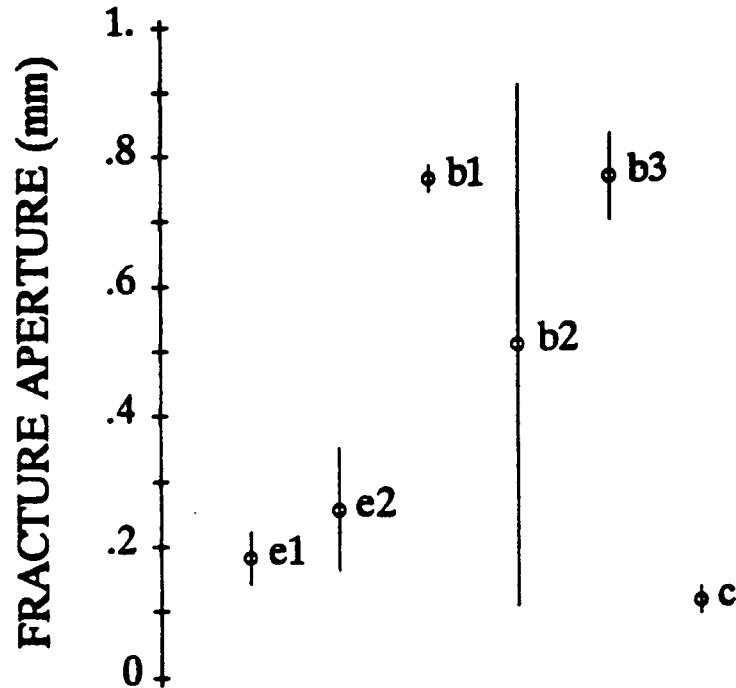


Figure 2-5. Effective fracture aperture determined from various methods. The circle represents the effective aperture value and lines represent one standard deviation (Rasmussen, 1995).

It is observed that the parallel plate hydraulic aperture deviates more from the physical aperture with increase in variance of $\ln b$. It has been speculated that it may be true, presumably due to the abundance of small apertures which create constriction to flow.

2.8 RELATIVE PERMEABILITY

The aperture width can vary significantly over the fracture plane, ranging from zero at contact points and it can be much larger than the effective aperture at the other points. The variation in aperture width has a strong influence on the ability of the fracture to transmit water under unsaturated flow conditions. This is the case because, in a capillary dominated flow, the aperture widths determine the volume of the fracture that can transmit water at a given matric potential.

Many investigators have performed numerical modeling (Pruess and Tsang, 1990; Kwicklis et al., 1991) as well as physical experiments (Persoff et al., 1991) in order to establish relationships between water or air saturation and the relative permeability of a fractured media. Typically, water/air relative permeabilities are presented by one set of curves as shown in Figures 2-7 and 2-8. In these figures, results from the numerical calculations have been presented for lognormal distribution of aperture widths for several variances. These figures show that the relative permeability to air decreases with increasing aperture variance at smaller matric potentials during wetting. This is because at smaller matric potential, water is essentially held by the small apertures and these small apertures are abundantly present. Only a small range of matric potentials was observed in Figures 2-7 and 2-8 over which both liquid and gas phases have nonzero relative permeabilities. A hysteretic effect can also be strong in the relative

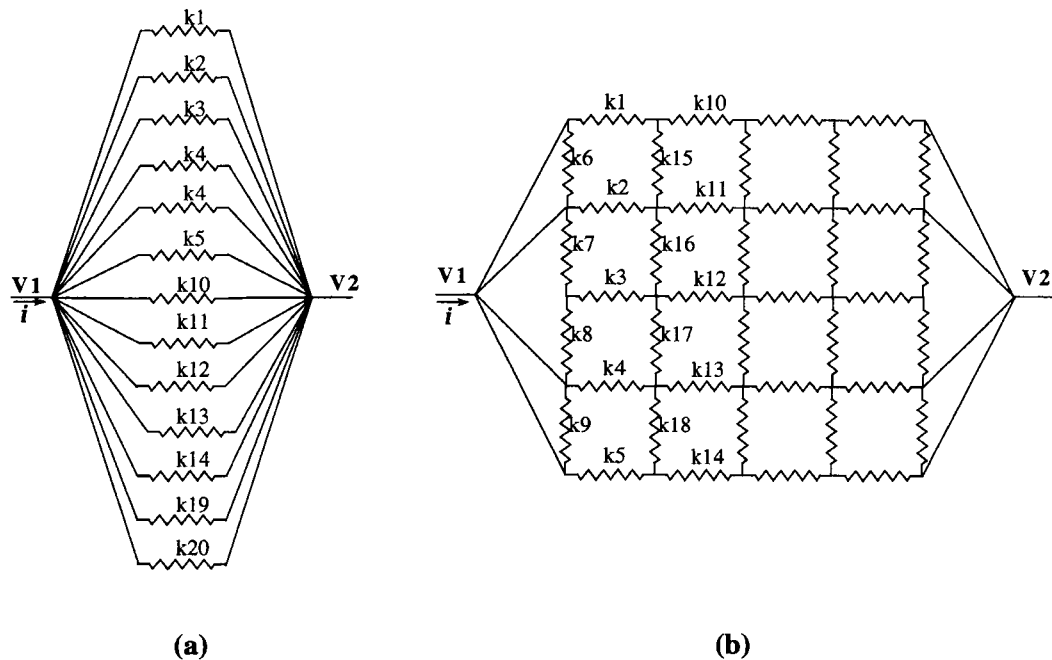


Figure 2-6. Schematic demonstrating the concept of tortuosity in 2D flow: (a) represents when tortuosity is absent, and (b) represents its presence

permeability curves (Pruess and Tsang, 1990; Kwicklis et al., 1991). This effect depends on the mode of saturation, that is, whether an originally air-filled medium was encroached by water or vice versa.

2.9 MODELS RELATING STRESS-DEFORMATION AND HYDRAULIC PROPERTIES

Most models describing hydraulic properties as a function of stress deformation use a variable aperture description of the jointed rock mass. The fracture flow in these models is accounted for either explicitly by taking all apertures into account in the calculation, or by using their statistical properties. Because it is impossible to determine the void space or aperture distribution for all rock joints, therefore, statistical properties and probability density functions of the aperture distributions are commonly used. The statistical properties typically used are the mean, standard deviation, and correlation length. On the other hand, the displacement under mechanical load is calculated as the mechanical pressure averaged over the contact areas (zero aperture). For example, Gangi (1978) calculated the stress-displacement relationship in which the mechanical pressure is averaged over the points of contact between the two surfaces that are needed to encompass the asperities. Tsang and Witherspoon (1981) used the concept of deforming the void spaces, where a concept of mean rock surface is used. In this approach, the grain protrusions with reference to the mean surface contact each other from opposite rock surfaces to form the asperities. The void space is defined between these asperities.

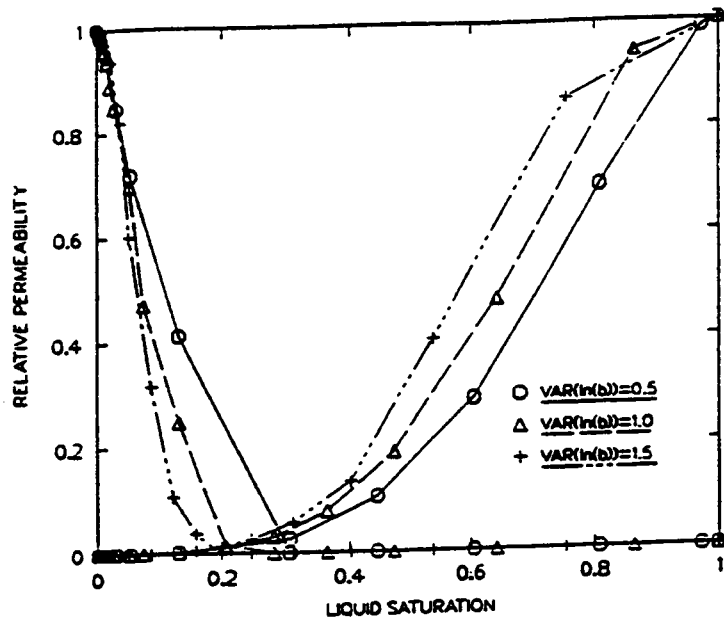


Figure 2-7. Typical relative permeability versus water saturation curve for a water-air system. The three sets represent three different aperture variances in a single fracture (Kwicklis et al., 1991).

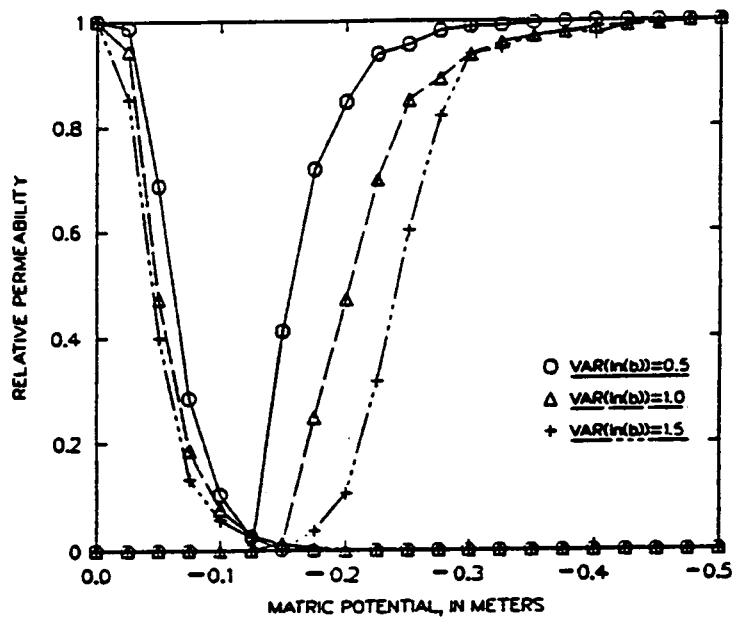


Figure 2-8. Typical relative permeability versus matric potential curve for a water-air system. The three sets represent three different aperture variances in a single fracture (Kwicklis et al., 1991).

In general, two different modeling approaches have been adopted: (i) empirical or exceptional models, and (ii) physical models. Physical models are based on the principle and theory of elasticity and the Hertz theory (Brown and Scholz, 1986; Swan, 1983; Johnson, 1983). Based on theoretical studies, Walsh (1981) suggested that the relationship between effective pressure and hydraulic conductivity can be represented through a linear relationship between the cube root of hydraulic conductivity and logarithms of effective pressure. Watanabe and Kodajima (1981) suggested a relationship between fracture aperture and hydraulic conductivity using a triaxial experimental apparatus with a cylindrical specimen which has a longitudinal fracture. Watanabe and Hoshino (1980) presented an approximated fracture hydraulic conductivity model based on an asperity model.

Bandis et al. (1983) have considered initial contact area; relative amplitude of the aperture, distribution of aperture, wall roughness, strength and deformability of asperities; and thickness, type, and physical properties of unfilling materials as the characterizing parameters. A joint constitutive model was proposed by Barton et al. (1985) that relates permeability and shear and normal stress. The model is based on joint roughness coefficient (JRC), joint wall strength, residual friction angle, and the conducting smooth-wall aperture. Barton and others presented a relationship between the actual aperture and theoretical aperture given by

$$e = \text{JRC}^{2.5} / (E/e)^2 \quad (2-20)$$

where JRC is the joint roughness coefficient, E is a real mechanical aperture obtained from a shear test, and e is a theoretical smooth-wall aperture obtained from a flow test. We are not aware of any equation which is capable of including the production of gouge into a theoretical calculation. As fundamental joint properties depend on the scale effects, therefore, empirical relationships were presented to account for sample size and joint spacing.

A physical model was proposed by Tsang and Witherspoon (1981). In their model, the joint consisted of a collection of voids and the closure occurred as a result of deformation of these voids. They represented $\langle b \rangle$, a weighed average aperture as a function of normal stress. For linear flow,

$$Q(x) = \frac{w}{L} \frac{\rho g}{12\mu} \langle b^3 \rangle_x^{1/3} \frac{1}{\langle 1/b^2 \rangle_y} [H(0) - H(x)] \quad (2-21)$$

where $\langle b^3 \rangle_x^{1/3}$ is the average over the width of the sample and $\langle 1/b^2 \rangle_y$ is an average over the length of the sample in x and y directions, respectively. $Q(x)$ is the flow rate in the x-direction and $H(0) - H(x)$ is the head drop across the system. This model does not appear to agree well with experimental data when the aperture distribution shows large variation.

Based on a nonlinear fracture deformability model proposed by Goodman (1976), Iwai (1976) presented a model relating flow rate and nonlinear stress:

$$\frac{Q/\Delta h}{(Q/\Delta h)_0} = \frac{1}{\left[A \left(\frac{\sigma_e}{\zeta} \right)^t + 1 \right]^3} \quad (2-22)$$

where $Q/\Delta h$ is the flow rate per unit head difference at imposed effective stress σ_e . The subscript 0 indicates zero effective stress condition. A , ζ , and t are empirical constants. Using the cubic law assumption, this equation can be presented in the form

$$\frac{K_e}{K_0} = \frac{1}{\left[A \left(\frac{\sigma_e}{\zeta} \right)^t + 1 \right]^3} \quad (2-23)$$

where K_e and K_0 are hydraulic conductivities of the rock mass at effective stresses σ_e and 0, respectively. The similarity between the above two equations suggests that, if a set of parallel fractures have the same deformability, then the hydraulic conductivity of the whole set together can be obtained by conducting laboratory tests on a single fracture (Case and Kelsall, 1987).

Having data on equivalent fracture aperture as a function of applied stress improves one's ability to visualize mechanical models of fracture behavior under stress. A change in the fracture aperture represents a measure of change in the physical system itself. A change in permeability in turn represents a change in the resultant rock property (Amyx et al., 1960). The measured change in the equivalent aperture or aperture distribution as a function of stress may lead to predicting porosity and permeability of different fracture flow channels.

Most of the available experimental techniques used for measuring hydraulic properties of intact rock mass could theoretically be applied to fractured rock masses. However, such applications could be potentially limited. For example, as the fractures have an extreme anisotropy (thickness compared to the length or width), specimen size usually constrains laboratory tests to specimens containing only one or two fractures. Tests using a single fracture can provide important information on the effect of temperature, stress, surface roughness, fracture infill, etc., on the fluid flow characteristics. However, it is difficult to study these effects on a system of fractures because a few fractures at the laboratory scale cannot capture the fracture network geometry completely. This leaves one with either the option of conducting expensive very-large block tests that contain a statistically significant number of fracture intersections or conducting field-scale tests. Although standard methods that are used for homogeneous porous media are used for fractured media, a number of difficulties are inherent in the latter test. In an injectivity test, the use of high pressure may open up the fracture intersecting the well. High pressures are often required in order to obtain a measurable flow rate during the test. The fractures may get sealed due to the invasion of the drilling fluids. The fractures may open up because of the stress changes due to excavation or drilling activities or due to vibration associated with blasting activities. Even in large-scale tests such as field tests, fracture density, network anisotropy and length of individual fractures play a significant role. Therefore, it is quite common to see a large scatter in the test data (Priest, 1993).

3 JOINT PROFILE MEASUREMENT

There are various approaches to measuring rock joint profile. One approach is to use a noncontacting laser source based technique. Esaki et al. (1992) used one version of this and measured surface roughness. This device included a cross-traveling micrometer stage on which the sample is placed. A laser displacement meter with an accuracy of 0.001 mm was set at a fixed location above the joint surface. It appears that their micrometer stage had to be mechanically displaced from point to point to take measurements, which could be an extremely cumbersome task. They took measurements inside a 40×40-mm area on both surfaces, which corresponded to approximately one quarter of the total surface area of the fracture face. In the following sections, the surface profilometer developed at the CNWRA is described. In contrast with the apparatus used by Esaki et al. (1992), this apparatus is fully automated and is capable of obtaining aperture distribution from a much larger surface area. Background discussions on the use of this apparatus for surface profiling can be found in Hsiung et al. (1994) and Mohanty et al. (1994). While providing further details on the operation of the profilometer, this chapter also provides the detailed technique developed for aperture distribution.

3.1 LASER SCANNING PROFILOMETER

The CNWRA apparatus built for profiling a rock surface and retrieving aperture data is a noncontacting profilometer assembled in-house. A photograph of the assembly is shown Figure 3-1. The equipment consists of an X-Y-Z positioner, scannerhead, a machine table, and a computer data acquisition system. The X-Y-Z positioner is held in place in an inverted fashion by a sturdy four-legged frame, 750 mm long, 500 mm wide, and 400 mm high. The X-Y-Z positioner is an Asymtek A-102B benchtop gantry-type. It has a 25.4-mm-diameter smooth bar which moves horizontally and perpendicular to its own length on guide rails at its two ends. A stepper motor using a toothed flexible belt and two gear wheels move the horizontal bar on the guide rails. The scanner head hangs from the horizontal bar and moves along the length of the horizontal bar for scanning in the x-direction.

The horizontal bar is attached on one side to a moveable carriage which moves transverse to the horizontal bar. Each movement of this carriage is such that the new position in the y-direction of the horizontal bar is parallel to its old position. The other end of the horizontal bar has a pulley that slides on the rail (linear bearing). The bar slides on two guide rails by another stepper motor. The pulley of the motor is connected to the movable carriage through a toothed pulley such that the rotary motion of the pulley on the motor results in the linear displacement of the horizontal bar assembly in the horizontal direction transverse to its length.

The stepper motor completes one revolution of the pulley over 200 steps resulting in a step angle of 1.8°. The step angle is increased or decreased in order to control the linear displacement of the scanner head. The step angle is controlled by varying the number of pulses fed to the motor.

An LC-2320 red-visible laser head is attached to the Z-axis of the A-102B X-Y-Z gantry positioner. The LC-2100/2320 combination forms the laser displacement meter. The laser head has a specified vertical displacement resolution of 0.5 micrometer. The laser head has a measurement window of about 18 mm from a standoff position of about 50 mm. The laser displacement meter operates on the principle of triangulation. According to this principle, when the laser head is raised or lowered, the apparent shift in the position of the laser light spot indicates the displacement. From a standoff position of 50 mm, a laser spot of about 140 micrometers in the mid-range is obtained.

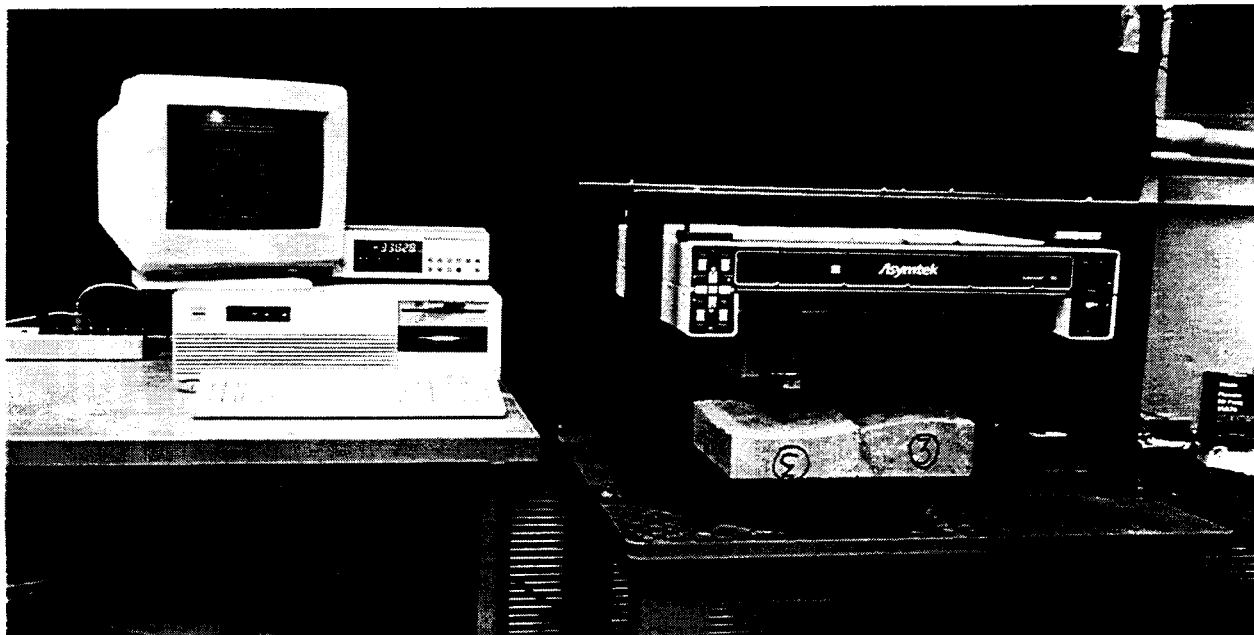
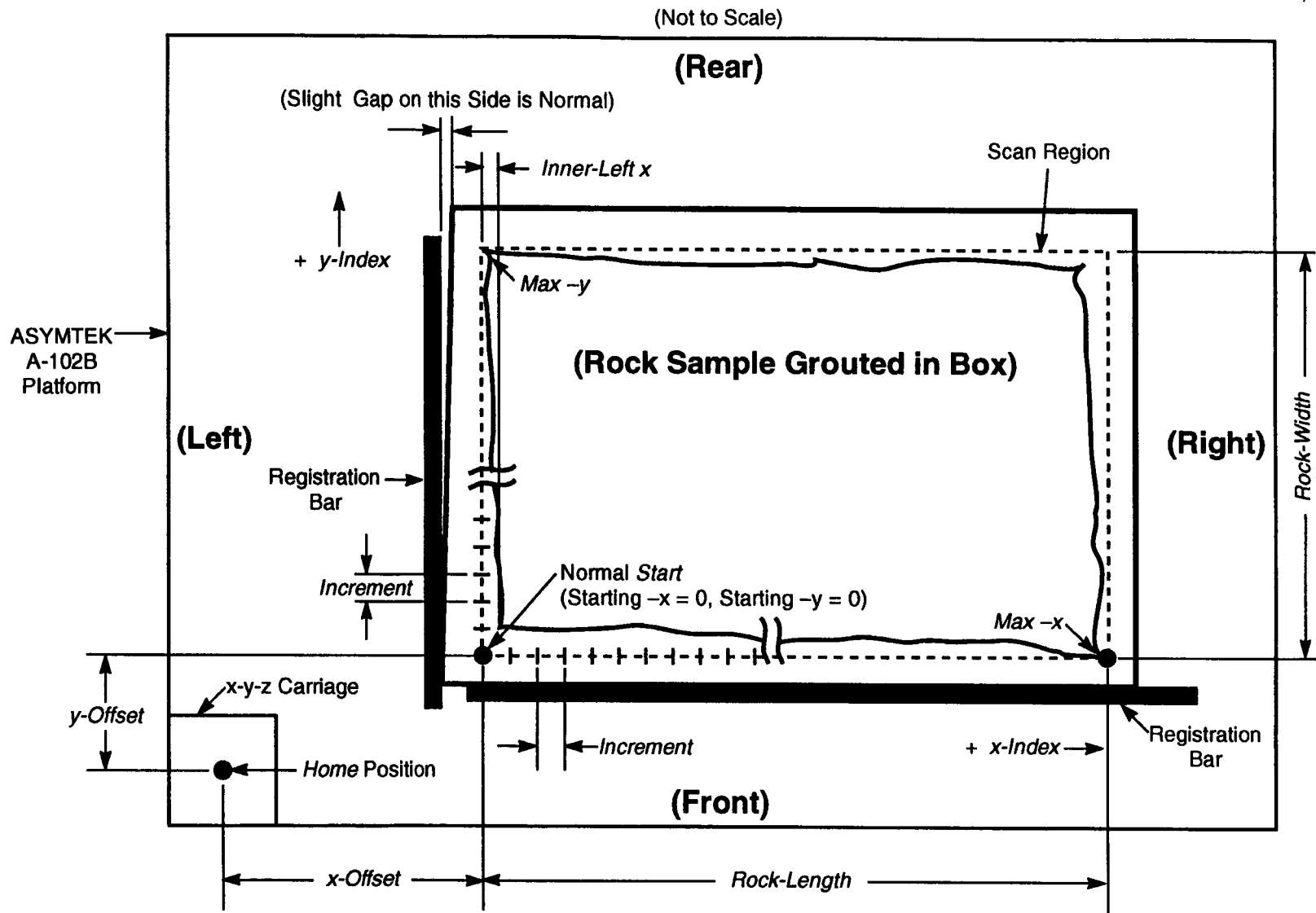


Figure 3-1. Photograph of the laser-scanning profilometer along with the controlling and data acquisition system

3.2 CONTROLLING AND OPERATING PROGRAM

The entire rock profiler system is controlled by IBM PC/AT commands to the A-102B X-Y-Z table by way of a serial communication port. The A-102B table has a built-in microcomputer for interpreting high-level commands from the PC/AT and then executing the move.

A custom computer program for the AT computer, written in Borland's Turbo C, Version 2.0, is used to issue move commands to the A-102B, to read the displacement measurement from the LC-2100, and to format and store pertinent scanning and rock profile displacement information in a PC floppy disc or hard drive. The program seeks to learn whether the user is initiating a "normal" test or otherwise. For a normal profiling condition, the user describes the area to be scanned. The coordinate parameters are set to zero to imply that the scanning start point is set at the origin. The increment is set to 50 mils (0.050 in.) which is the normal scan step increment in the x- and y-axis directions. X-Y-Z table scanning parameters are clearly shown in Figure 3-2. The origin at which the user wishes to start profile scanning may also be other positive integers within the scanning perimeter of the rock surface. The user specifies



3-3

Figure 3-2. Top layout of the laser profiles showing the scan parameters

parameters, such as rock length, rock width, x-offset, y-offset, increment, etc. (and an inner left-x to match the parameters from the previous file if the program is restarted).

The operating computer program guides the user through a series of instructions to use A-102B front panel keys to manually locate rock surface locations, such as innermost front edge, outermost back edge, etc., to define the area to be scanned during the profile session. The user is then given a display of the scan parameters that will be used and asked if he wishes to proceed. If he continues, he is given the opportunity to observe the X-Y-Z table scan the parameter of the rock surface area that will be profiled. Immediately after this, the X-Y-Z table is homed (i.e., reference HOME switches located at the front left corner of the A-102B and at the top of the z-axis travel are automatically located) and the rock profiling begins. A display on the video monitor shows current x-position, y-position, and LC-2100 displacement meter readings. A parameter, z-errors, keeps the operator aware of the number of out-of-range readings that are encountered during the profiling. Out-of-range readings should be rare and will likely occur only where very abrupt changes in surface height occur. An estimate of time remaining is also displayed and reflects the actual average time to process a row of data experience, up to that point of time, multiplied by the number of rows remaining to be processed. The program has provision for restarting a session after power interruption, purposeful termination of the program as well as for retesting of the same specimen, using the same scan parameters. If a profiling session is being restarted, the user moves to the end of the last file in which data have been collected, and notes the last row and column number that have been successfully processed. By entering these two numbers, the data acquisition is restarted. The program has the option to append new data to the existing partial data file from where the previous session left off, or it can create a new data file.

3.3 FUNDAMENTAL OPERATING PROCEDURE

Before test data are taken, the Keyence LC-2100/2300 Displacement Meter is warmed up for at least 0.5 hr. When the laser head is turned on, an intense focused laser light (red) from the sensor head is seen. As a safety precaution, one should not look directly into the laser beam. For accurate readings, the room temperature should not be allowed to vary widely and should be maintained in the range 30–35 °C, since the temperature affects the accuracy of the reading. Also, intense light, such as from direct sun through a window, shining on the rock surface under test will significantly degrade the LC-2100/2230 performance and should be avoided. Proper operation of the rock profiler is ensured if the input parameters are limited to 500 steps/in. in the z-axis and 1,000 steps/in. along the x- and y-axis. Specification for the profilometer are summarized by Mohanty et al. (1994).

For data acquisition purposes, the jointed rock mass is first cut to the rectangular size by using a water jet cutter and a disc blade cutter. The rectangular block is then polished on all six sides to 1/1000 in. (0.025 mm). Care must be exerted in order to minimize the damage to the fracture face because both the rock masses constituting the rock joint are held together while polishing the block. Then the vertical faces and top and bottom sides are marked and the thickness at the four corners is measured. The schematic of the rectangular block with indicated corner heights is shown in Figure 3-3. For surface sampling purposes, the rock profiler platform is cleaned to remove any particles that would displace the rock sample from its reference position.

The rock sample surfaces are also cleaned to remove loose debris that would cause inaccurate height measurement. The top block is flipped upside-down and aligned with the bottom block by letting the two neighboring sides touch each other; then, both these samples are held together as one piece and

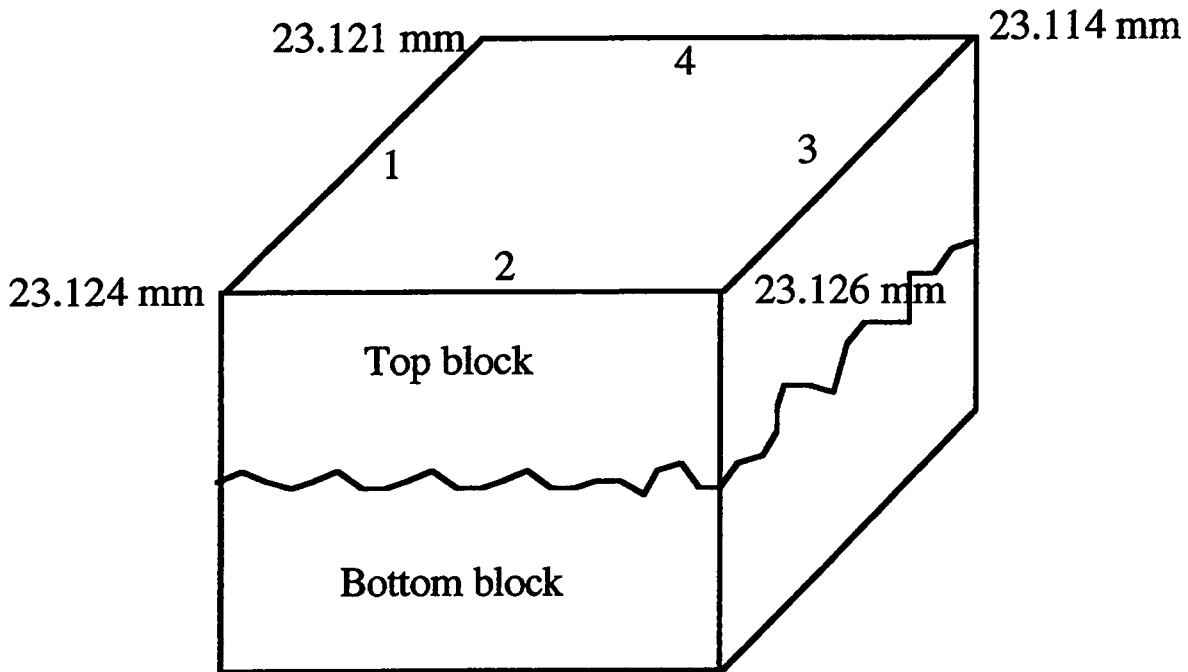


Figure 3-3. Schematic of a joint specimen ready for profilometry. Sides are identified and the corner heights are indicated.

are slid together to the corner created by the intersection of the vertical and horizontal rectangular bars. The rock sample is registered accurately by pulling the rock forward against the front stop, then sliding it to the left against the left stop. Then, it is ensured that the rock samples are flushed against the front stop. A gap between the rock sample and the left stop is normal, though the rock sample must contact the left stop at some point. The z-axis of the A-102B is manually lowered and carefully moved over the rock surface to assure that it cannot inadvertently collide with the rock surface. Note that the z-axis will sag to its lowest position when the A-102B is turned off or RESET, and may shift into a position where it could collide with the rock. A repeatable location of the rock sample relies on careful registration of the rock sample by full contact with the front registration bar and contact with the box at a point on the left registration bar. It should be ensured that neither the registration stops nor the LC-2320 sensor head mounting position slips, otherwise the reference position will be lost. In order to verify the accuracy and repeatability of the rock profiles, calibration has been done using gauge blocks. Although such calibration is a very tedious process, it reduces the requirements for computer manipulation of data. The calibration is also mandated by the quality assurance program.

After acquisition of the surface height data, the height data for the top block were flipped numerically. Using the touching sides of the top and bottom blocks as a reference line, the inverted top block is superimposed on the bottom block. By positioning three equal-height aluminum bars at any three locations adjacent to the rock masses, the angle of inclination between the bottom surface and the laser beam traversing plane is obtained. In essence, one plane is assumed to be the reference plane and the slope of the other plane is obtained. The aperture at each location is obtained by using

$$b = rd + rd_1 - (h_1 + h_2) \quad (3-1)$$

where

- rd = height of the rod
- rd_1 = depth reading by the profilometer
- h_1 = thickness of the top rock
- h_2 = thickness of the bottom rock
- b = aperture width

It should be kept in mind that the laser scanning profilometer may involve scatter in the data, thus leading to uncertainty. This is evident from the scatter in the depth data presented in Figure 3-4 that was obtained by scanning the top of the smooth aluminum rod. Ideally, one would expect to see a single spike in the histogram. Therefore, it must be ensured that the scatter in the data is negligible compared to the accuracy needed in the aperture data.

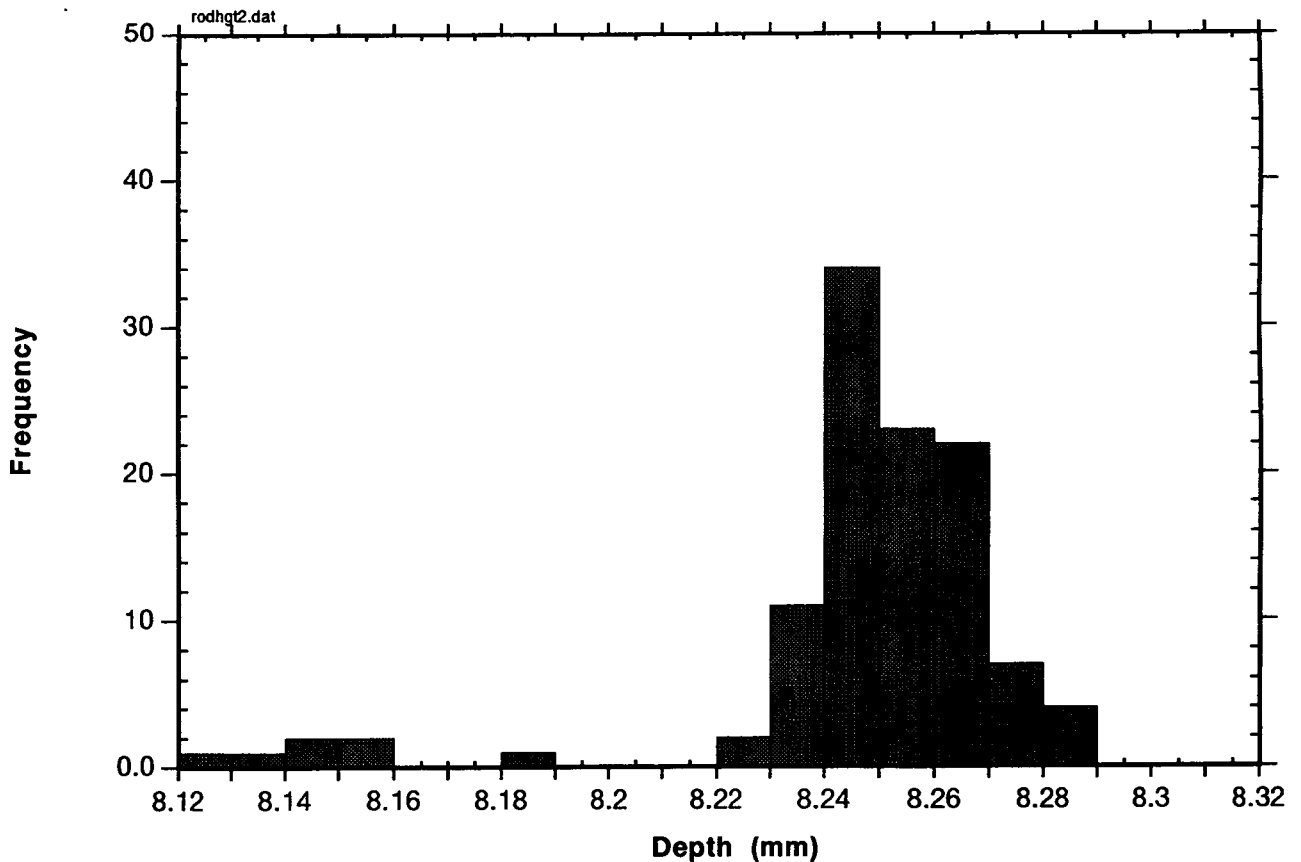


Figure 3-4. Histogram of profilometer data collected from the surface of an aluminum block used in determining the reference height. This figure depicts the level of noise that could be expected in the data.

4 APPARATUS AND PROCEDURE

4.1 BASIC APPARATUS

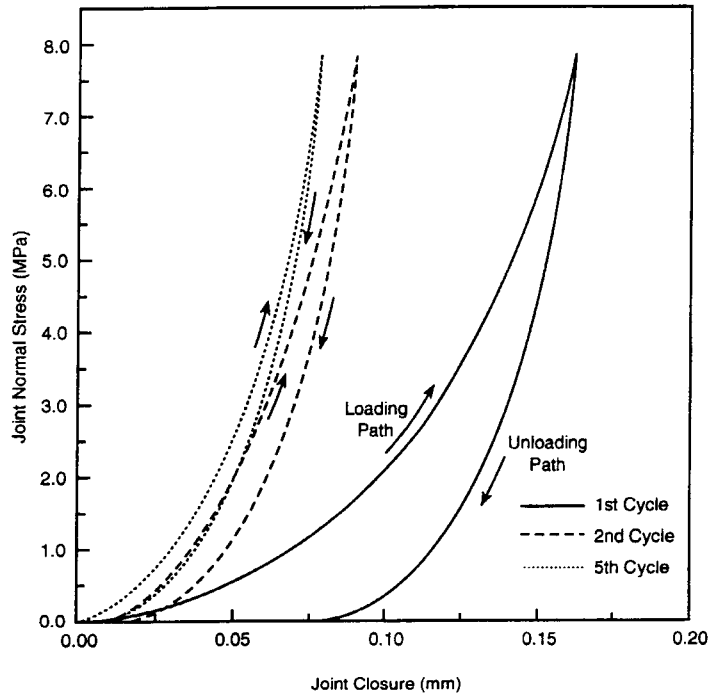
The apparatus for conducting experiments on fracture flow behavior of single joints under normal and shear loads has been described in detail by Mohanty et al. (1994). In brief, the apparatus is based on the direct shear test method. This apparatus has been prepared by the enhancement of a direct shear testing machine called "basic apparatus" (Kana et al, 1990; Hsiung et al., 1994) to incorporate the hydrologic aspect of the MH experiments. The apparatus consists of vertical and horizontal servocontrolled loading actuators, reaction frames, shear box fixtures, and an instrumented jointed tuff specimen. The loading capacity for each of the three vertical actuators is 0.133 MN, while the horizontal actuator has a capacity of 0.222 MN. The horizontal actuator can be operated in either load or displacement control mode. Each vertical actuator is equipped with a 0.111 MN capacity load cell for monitoring the applied forces. The instrumentation for monitoring the applied normal load is arranged to provide an analog output for the sum of the three load cells, as well as for the individual signals. The bottom shear box is designed to house a specimen with maximum dimensions of 0.305×0.203×0.102 m. The top shear box houses a specimen with maximum dimensions of 0.203×0.203×0.102 m. Both specimens are grouted in their respective specimen boxes by using cement. The bottom shear box and other fixed devices are bolted to a 1.22×2.13×0.15-m-thick steel base plate for rigidity. The horizontal translation of the top shear box along the direction of shearing is guided through three rollers between the top shear box and normal load frame. It is also guided through side rollers. Thus, the normal load frame and the side rollers prevent rotation of the vertical actuators (and, therefore, also the top specimen block) about a vertical axis perpendicular to the direction of shearing.

The original apparatus for MH experiment has demonstrated a capability for measuring the effect of rock-joint shear displacement of up to 0.0254 m (1 in.) on permeability, though theoretically, a displacement of up to 0.0508 m (2 in.) can be studied. A new dynamic sealing mechanism allows linear steady-state fluid flow for permeability measurements. Shear load experiments were much more difficult to perform compared to the normal load experiments. This increased difficulty was due primarily to the extreme conditions to which the fluid sealing mechanism was subjected. These extreme conditions were complicated by the fact that shear testing is a destructive test method. It is clearly evident that damage of the rough surface produces a significant amount of gouge material. Thus, it is necessary to separate the effects of joint dilation on the flow from that of gouge material on the flow. Modifications that have been incorporated this year address some of these issues.

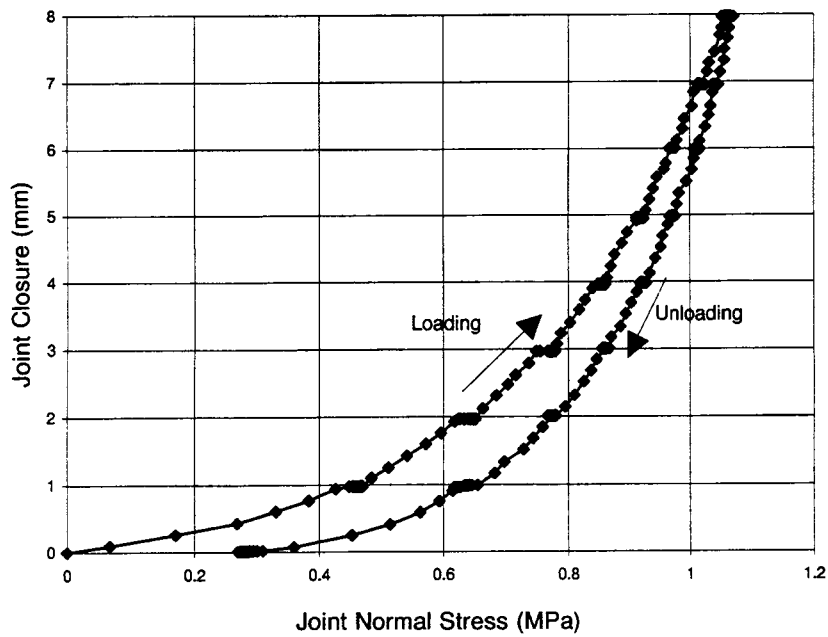
4.2 MODIFICATION TO ENHANCED DIRECT SHEAR TEST APPARATUS

The grout boxes holding the rock joint specimen were modified in order to rectify some of the deficiencies in the original grout boxes. While every care was taken to obtain the best match between the top and bottom rock joint, the normal displacement was observed to be greater than what was measured using the "basic apparatus" (Kana et al., 1990; Hsiung et al., 1994). This is evident in Figure 4-1 in which the joint normal displacement has been presented as a function of normal load. Difficulties were also experienced in calculating acceptable aperture distribution from profile data measured before and after shear load experiments. Numerical modeling¹ using the surface profile data to study joint dilation

¹Ohnishi, Y. 1995. Private Communication



(a)



(b)

Figure 4-1. Joint normal stress versus joint closure: (a) with basic apparatus, and (b) with apparatus enhanced for flow experiment

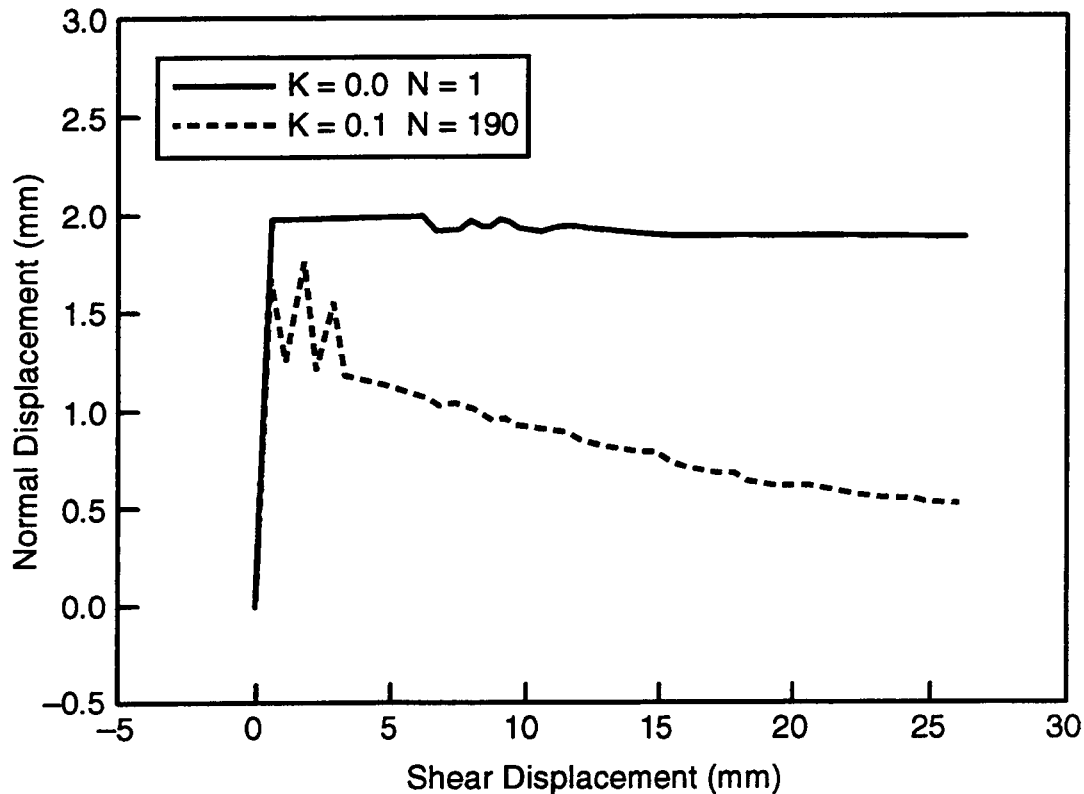


Figure 4-2. Numerical dilatancy prediction from measured joint surface profile

behavior did not show the expected normal-shear displacement relationship (Figure 4-2). To address the above problems, a stricter control on the apparatus design, experimental procedure, and profile measurement was warranted. As the post-test profilometry of the joint surface is done while the rock masses are grouted in the box, it must be ensured that the aperture distribution calculation techniques account for the shape of these boxes. The aperture distribution calculation technique requires that the top and bottom of the top and bottom grout boxes, respectively, are parallel to each other, in addition to these surfaces having a smoothness well within the precision of the aperture data.

In order to fabricate a rigid box in the modified apparatus, the box frame was prepared from a rectangular steel block of dimensions 18.00×10.25×4.00 in. Steel from a 12.5×8.75×4.00 in. section was extruded out in order to obtain the frame of the box. To start the extrusion process, four holes were first drilled at four corners of the rectangular block. Then, these holes were corrected by using saw cuts. All four internal sides were then ground to within the specified tolerances. The exterior of the frame was polished to within specified tolerances. Then, the mounting holes for proximeter detector plates, etc., were drilled and tapped to specifications. The top and bottom plates were polished to specified tolerances. In the new design, the exterior dimensions of the grout box were kept identical so that the corner brackets with pins could be accommodated. A schematic drawn to scale is presented in Figure 4-3. The four corner brackets can be seen clearly in the top view presented in the figure.

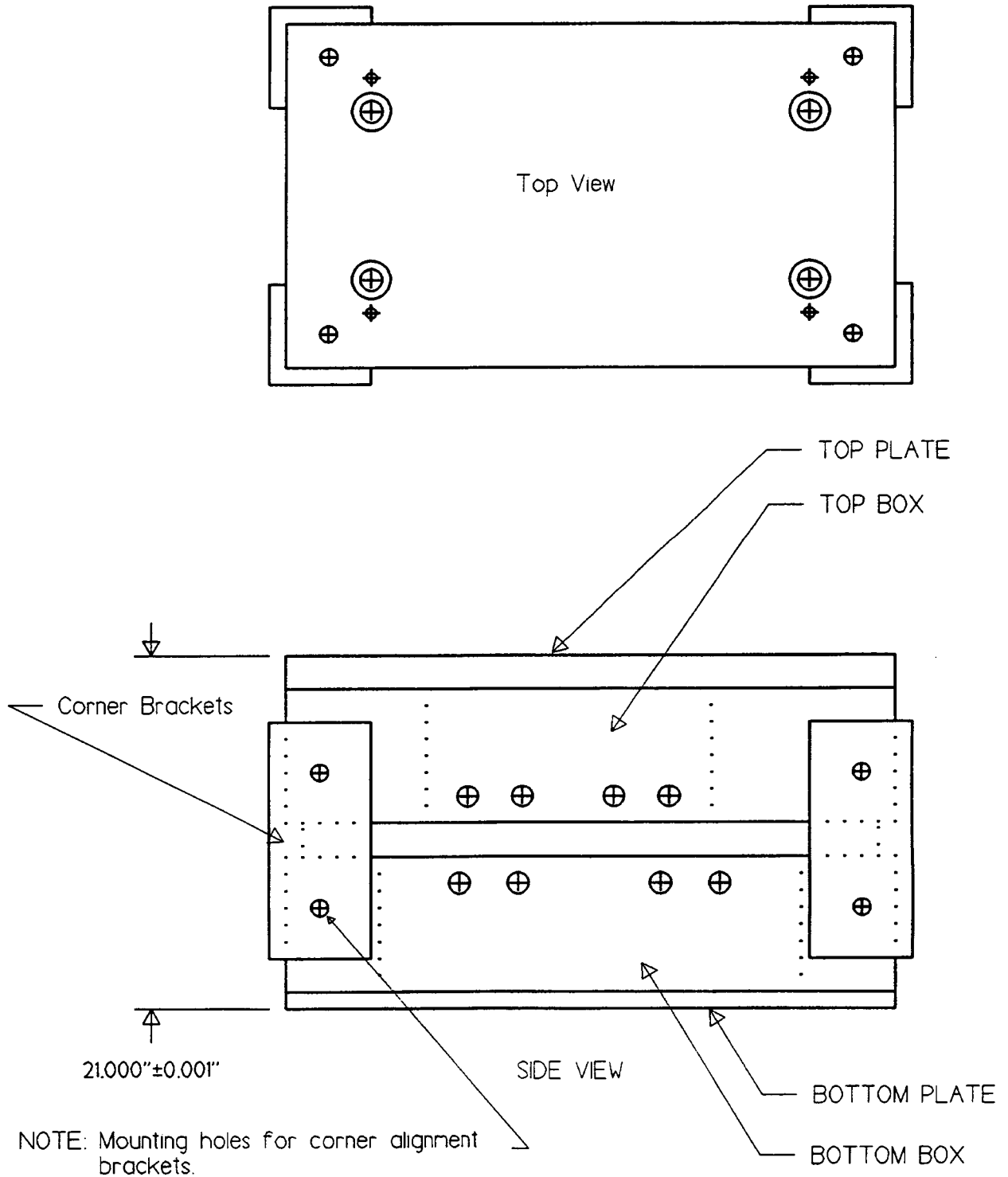


Figure 4-3. Elevation and plan view of the modified grout box. 90° brackets on four corners are designed to ensure the position of the two blocks under matched condition of the fracture surfaces.

In order to initiate the grouting process, the bottom plate was bolted onto the bottom box frame. The bottom rock was then grouted into the bottom box. Next, the top box frame and four corner pin alignment devices were assembled. The top rock was put on top of the bottom rock in the fully matched condition. Spacers 1-in. thick were placed between the top and bottom box surrounding the rock joint. Then, the top box assembly was put on top of the bottom box and held in place by using the alignment pins on the bottom box. The top rock was then grouted, and the top plate was installed. All four corners were measured by using a dial gauge to ensure that the specified heights were maintained. If differences in corner heights were observed, then it was ensured that the gap between the top box frame was completely clean of gouge materials. The whole grout-box assembly was then dried in an oven at 105 °C for 7 d. Then, the assembly was dismantled and the 1-in. spacers were replaced by rubber gaskets. The rubber gaskets with larger durometer readings were glued to the bottom box, and the softer gasket was attached to the top box. The two boxes were then assembled back together with the rubber gaskets in place. This assembly was done under compression load in order to engage the corner pins, because the thickness of the rubber gaskets exceeds 1-in. gap between the top and bottom box. Once the holding pins were in place, the load could be relieved. This new modification ensured that the top and bottom rocks were in matched condition before the rock was exposed to specified loading while performing the experiment.

4.3 APPARATUS FOR AUXILIARY EXPERIMENTS

The auxiliary experiments have been designed to provide measurement of the hydraulic properties of a single discrete horizontal fracture in the absence of any load other than the load needed to hold the rock joint together. Results from these experiments are to be used for establishing the experimental procedure and to aid in the MH experiments. Fracture aperture and permeability measurements can also be compared to similar measurements being made in the MH experiments.

The parameters measured in the laboratory experiments included the mean fracture aperture (fracture volume) and the saturated fracture permeability of gas and deaerated, deionized water. The hydraulic fracture flow laboratory experiments were performed on an 8×8×4-in. (20.32×20.32×10.16 cm) block of ALT specimen. The tuff specimen contained a fracture bisecting the block in the horizontal direction. The specimen was encased in a hermetically sealed container with inflow and outflow manifolds attached to two opposing ends of the block.

4.3.1 Theory

4.3.1.1 Mean Fracture Aperture

As defined in Chapter 2, the mean fracture aperture is the ratio of the total fracture volume [cm^3] to the fracture surface area [cm^2]. The mean fracture aperture was obtained using the constant volume pycnometer method.

The pycnometer methodology is based on Boyle's gas law, which states that the product of the pressure and volume of a gas for a contained system is constant at constant temperature. Therefore, if a smaller quantity of gas of known volume (i.e., a reservoir of known volume) and pressure is allowed to expand into a larger volume (i.e., the combined volume of the reservoir and the fracture, initially at atmospheric pressure), the resulting pressure can be used to calculate the fracture volume (Page, 1948;

Russell, 1950) by equating the sum of the pressure–volume products to those of the combined system. The volume of gas in the sample chamber was calculated as follows:

$$V_c = (P_r - P_f)V_r/P_r \quad (4-1)$$

where

- V_c = volume of gas in the fracture [cm^3]
- P_r = initial known gas pressure of the reservoir [Pa]
- P_f = final gas pressure of the combined reservoir and fracture system [Pa]
- V_r = initial known volume of gas in the reservoir [cm^3].

The fracture volume was measured after the rock matrix was saturated with deaerated, deionized water. In this way, the mean fracture aperture could be determined without including complicating factors, such as diffusivity of the gas into the rock matrix and unsaturated matrix porosity.

The mean fracture aperture (b) was determined as:

$$b = V_c/A_f \quad (4-2)$$

where A_f is the area of the fracture calculated as the length times the width of the tuff specimen or 412.90 cm^2 .

4.3.1.2 Fracture Permeability

Fracture permeability to both gas (N_2) and to deaerated, deionized water was determined in the hydraulic fracture flow experiments. The actual observed quantity was the pressure loss or macroscopic pressure differential, measured at the inlet and outlet manifolds of the experiment, for a given constant flow rate through the fracture. Fracture permeability was obtained by using Eq. (2-2).

4.3.2 Sample Selection, Test Cell, and Preparation

4.3.2.1 Sample Selection

The rock sample used in the fracture flow experiments was selected from welded tuff specimens collected from Apache Leap, Arizona, as part of Task 2 of the Seismic Rock Mechanics (SRM) research project. The tuff at the Apache Leap site is highly vitrified and densely welded, similar to the tuff at the horizon of the proposed HLW repository at Yucca Mountain, Nevada (Mohanty et al., 1994). The original core samples were 18 in. (45.72 cm) in diameter and were collected with a large-diameter core drilling technique that used water as the drilling fluid (Hsiung et al., 1994).

Sample selection criteria for the fracture flow experiments included: existence of a planar discrete fracture and a minimum rock size, which when prepared would allow for a finished block with dimensions of $8 \times 8 \times 4$ in. ($20.32 \times 20.32 \times 10.16$ cm) with the fracture running horizontally through the 4-in. (10.16-cm) height. The block was cut from the original core with a large rock saw at the CNWRA laboratory and then ground to its final dimensions. In both procedures, water was the lubricating fluid.

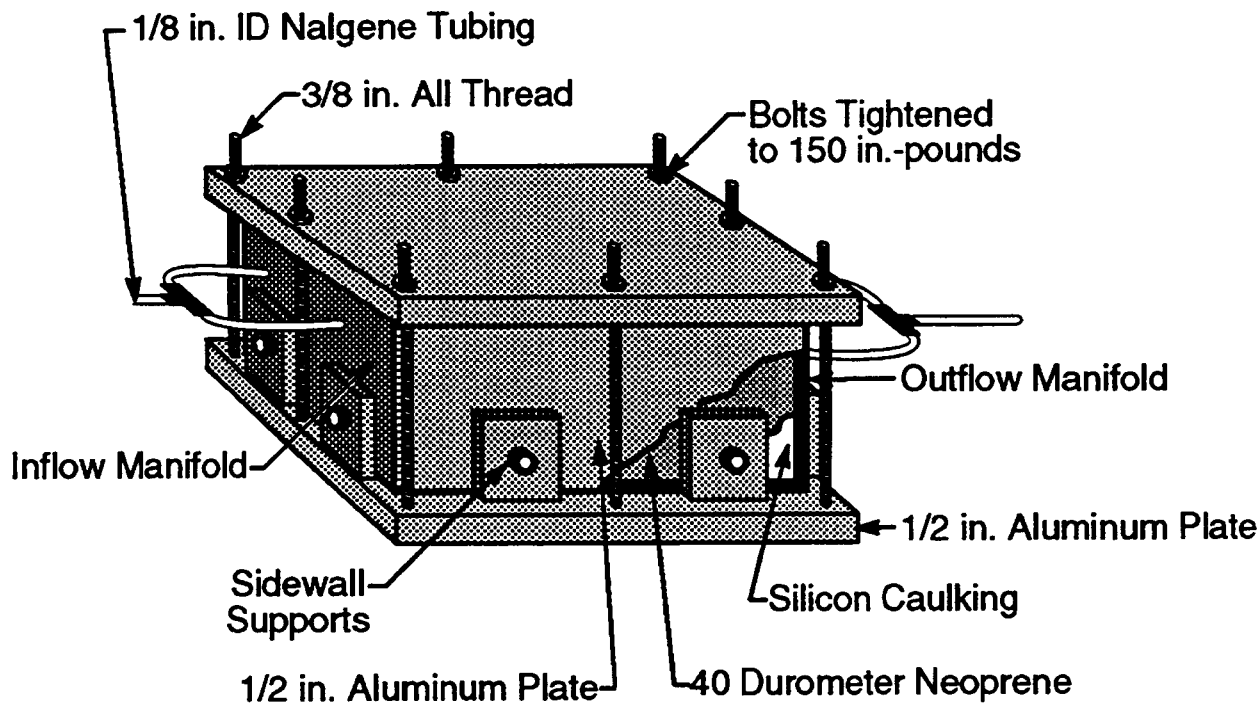


Figure 4-4. Schematic of sample test cell

4.3.2.2 Sample Test Cell

The test cell for the fracture flow experiments was designed and manufactured at Southwest Research Institute (SwRI) and assembled in the CNWRA laboratory (Figure 4-4). The test cell was designed to be hermetically sealed. It consisted of 0.5-in. (1.27-cm) thick aluminum plates along the top, bottom, and two of the sides (length) of the tuff specimen. Inflow and outflow manifolds [also of 0.5-in. (1.27-cm) thick aluminum] were designed to follow the fracture contours of two opposing sides (width) of the tuff specimen. The manifolds were designed to create constant laminar flow (Figure 4-5). The side aluminum plates and manifolds of the container were braced using allen bolts placed in brackets attached to the bottom plate of the test cell. Three-eighths-in., all-thread bolt was inserted through holes in the top and bottom plates, enabling them then to be bolted together.

Assembly of the tuff specimen inside the test cell was performed in the following manner. Duct tape was placed along the length of the tuff specimen. The specimen was placed on silicon caulking and 40-durometer neoprene in the middle of the bottom plate. The side plates were then emplaced along the length of the rock specimen using the caulking and neoprene, hermetically sealing the perimeter and bottom of the test cell. The manifolds were positioned with care along the fracture inflow and outflow ends to provide proper alignment of flow paths. The top plate was emplaced, once again using silicon caulking and 40-durometer neoprene. The test cell was then bolted together and allowed to dry for 24 hr. The bolts were then tightened to 150 in.-lb using a calibrated torque wrench to provide for a consistent

normal stress in all experiments. A fixed amount of torque was necessary to achieve repeatability in the experiment.

The test cell was then examined for leaks by first pressurizing the cell to approximately 14 psi (7×10^4 Pa), then observing the cell for 24 hr to ensure no pressure loss was noted.

4.3.2.3 Saturation Process

Preparation of the sample for the fracture flow experiments entailed drying the sample in an oven until a consistent mass was attained for a period of at least 3 d to ensure total desaturation. Full liquid saturation of the sample was then achieved in the following manner. The sample was enclosed in the hermetically sealed test cell, and a vacuum of approximately -29.3 in. Hg ($\sim -9.9 \times 10^4$ Pa) was drawn using a vacuum pump connected to the outlet manifold of the test cell. CO₂ was then permeated into the specimen by pressurizing to 20 psi (1.4×10^5 Pa) for a period of approximately 1.5 hr. The vacuum-CO₂ cycle was repeated twice, at which time a vacuum was redrawn and the sample was saturated with deaerated deionized water. The sample was pressurized to 18 psi (1.4×10^5 Pa) and left for a period of 24 hr, after which the sample was assumed to be fully saturated.

4.3.3 Experimental Apparatus and Procedures

The hydraulic fracture flow experiments were modified from established testing methods and the literature. The basic design for the pycnometric volume apparatus was taken from Danielson and Southerland (1986) and adapted for use in the fracture volume experiments. The fracture permeability apparatus is similar to that used by other investigators (Chuang et al., 1990; Bassett et al., 1994; Persoff et al., 1991).

4.3.3.1 Aperture Volume Measurement

The gas pycnometer experimental apparatus and methodology used to measure the aperture volume was modified from Danielson and Southerland (1986), Bassett et al. (1994) and Chuang et al. (1990). To apply the principle of Boyle's gas law, a pycnometer was set up utilizing a constant-volume reservoir and the assembled sample/test cell. A ball valve was placed within the connection to isolate or connect the cells as needed. A calibrated Parascientific absolute digital pressure gauge capable of measuring to the nearest 1/1,000 of 1 psi (± 6.9 Pa) was used to measure the pressure within the system during the analysis. The aperture volume of the saturated test sample within the test cell was calculated using this apparatus.

Two procedures were used to measure the aperture volume using the constant-volume pycnometer methodology. The first involved placing a known initial positive pressure on the reservoir (Figure 4-6), and the second procedure involved drawing a known initial vacuum on the reservoir (Figure 4-7). In both procedures, the volume of the reservoir (V_r) was calculated from reservoir dimensions that were measured with a caliper.

The first procedure was performed as follows. The valve between the sample/test cell and the reservoir was opened, and gas (industrial grade helium) was introduced to a known positive initial pressure (P_r), typically between 10 and 15 psi. The inflow valve was closed, and the system was stabilized for approximately 3 to 5 min to allow: (i) the gas to attain thermal equilibrium and (ii) to ensure there were

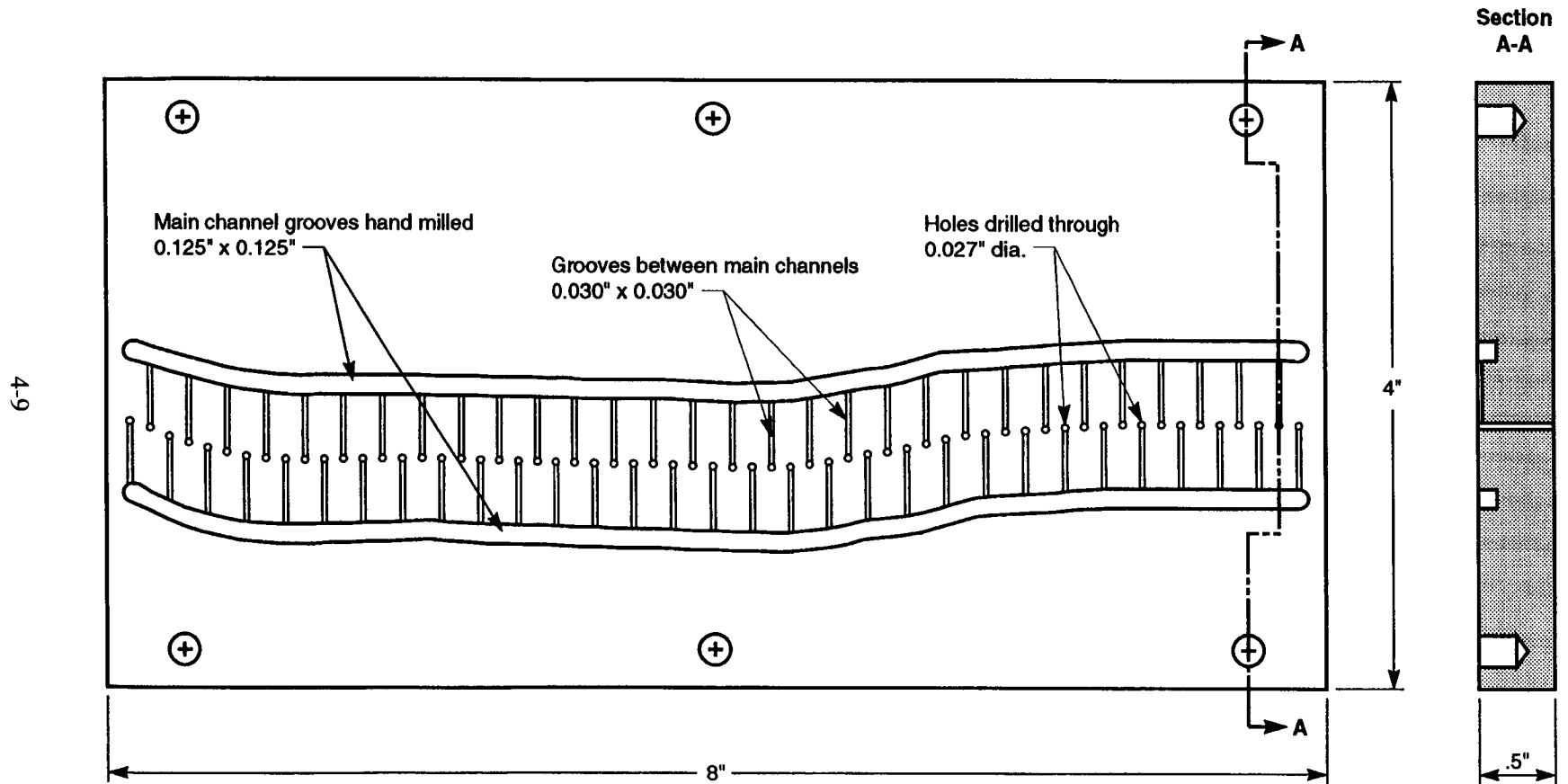


Figure 4-5. Schematic of inflow manifold

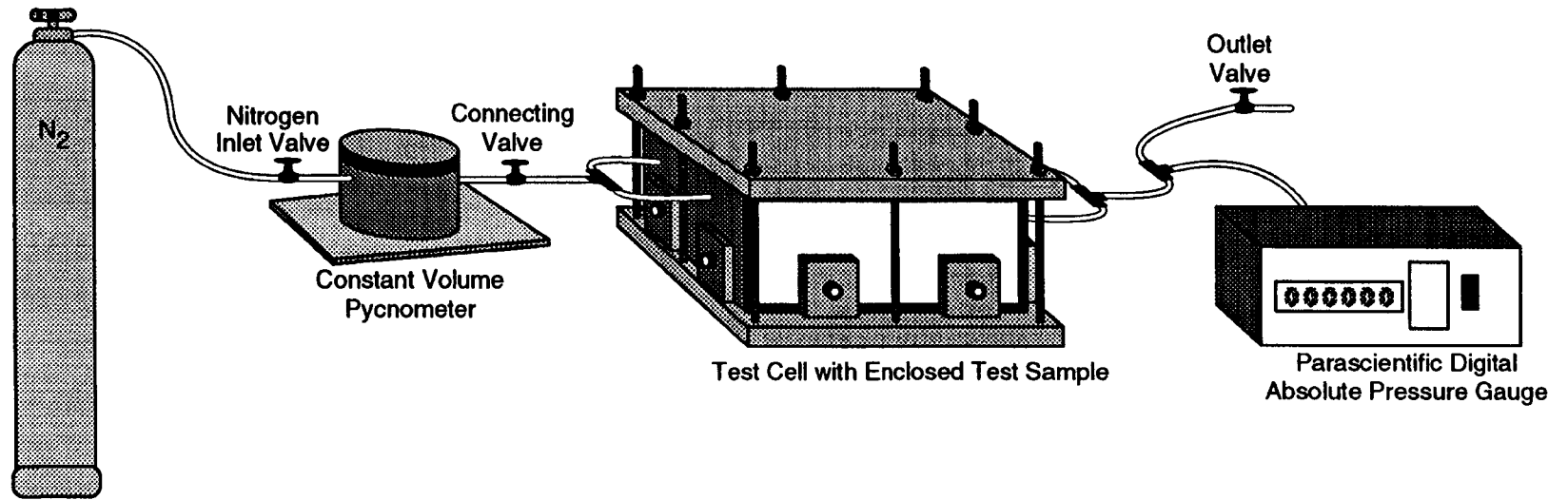


Figure 4-6. Schematic of positive pressure experimental apparatus used to measure aperture volume

4-11

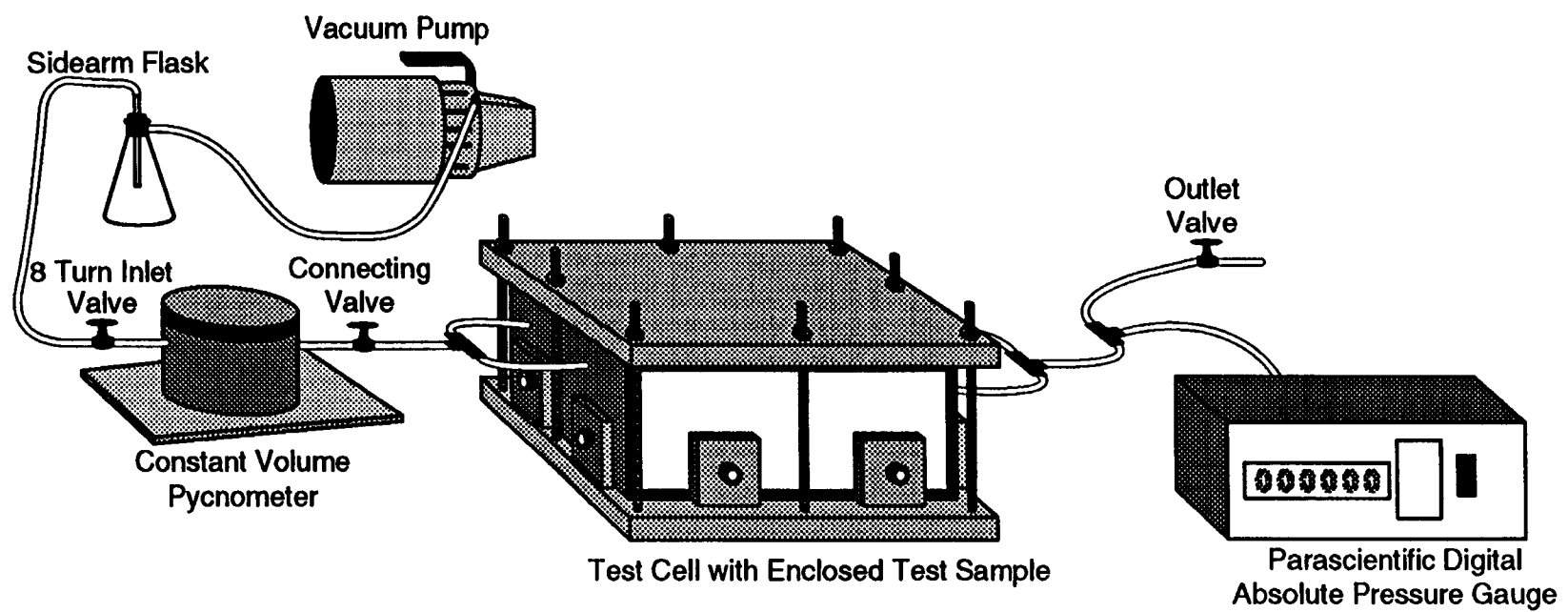


Figure 4-7. Schematic of vacuum experimental apparatus used to measure aperture volume

no leaks. The valve between the reservoir and the sample/test cell was closed, isolating the reservoir at the initial pressure (P_r). The relief valve located on the sample/test cell was opened, allowing the cell to come to atmospheric pressure (P_a), which was then recorded. The relief valve was then closed, and the two chambers were pneumatically connected by opening the valve between them. Once again, the system was allowed to sit for 3 to 5 min to ensure thermal equilibrium, after which the final pressure (P_f) of the combined system was recorded. The aperture volume was calculated using Eq. (4-1).

The second procedure was similar to the first with the exception that an initial known vacuum was drawn upon the system (P_r). A positive displacement vacuum pump capable of pulling up to -29.3 in. Hg (P_a) was used to create the vacuum. The aperture volume was calculated as in the first procedure.

4.3.3.2 Liquid-Saturated Fracture Flow Experimental Apparatus and Procedures

The design for the liquid-saturated fracture flow experimental apparatus and laboratory procedures was modified from the literature to conform to the physical size of naturally fractured specimens available to the CNWRA laboratory. The basic apparatus layout is shown in Figure 4-8. It consists of two major components, a computer-driven, constant-flow pump and a differential pressure transducer (DPT).

A QUIZIX 1040-A dual-piston positive displacement pump capable of creating constant-flow rates of 0.1 ml/min to 120 ml/min was utilized to create a constant flux through the aperture of the test specimen. The pump was run via computer software supplied by the manufacturer. The software also allowed for creation of a database of the flow rates instigated by the operator.

The pressure differential across the specimen was measured using a calibrated Rosemont DPT capable of measuring differential pressures to within ± 0.005 in. of H_2O . The pressure differential was recorded utilizing a calibrated chart recorder (Fluke hydra data logger). A Fluke meter was used to verify the pressure measurements.

Three types of flow-rate tests can be run using the QUIZIX 1040-A software. The first is a static-flow-rate test, in which the operator specifies the rate of the pump outflow. For cumulative volumes up to 60 ml/min, the pump can provide for continuous operation. At flow rates from 60 to 120 ml/min, the pump delivers a maximum of 80 ml outflow.

The second type of liquid saturated flow test conducted was a ramp-up test. This test establishes an increasing flow rate over time up to 60 ml/min. The operator sets the initial and final flow rates for the test to be conducted over a desired time period.

The final type of liquid-saturated flow test is the ramp-down test. This test establishes decreasing flow rates over time and is essentially conducted the same as the ramp-up tests.

The temperature of the permeating deionized and deaerated water was measured with a thermometer placed in a beaker that collected the outflow. In all tests, the temperature of the permeant was maintained between 22 and 24 °C.

A total of 7 static flow tests, 10 ramp-up tests, and 10 ramp-down tests were conducted on the test specimen with 4, 4, and 4 in the forward and 3, 6, and 6 in reverse flow directions. The static-flow tests were run both before and after the ramp-up and ramp-down tests.

4.3.3.3 Pneumatic Fracture Flow Experimental Apparatus

The design for the gas-saturated fracture flow experiments used a similar apparatus as the liquid-saturated flow experiments. The gas-flow apparatus consists of two major sections, a constant (or static) flow apparatus and a differential pressure apparatus (Figures 4-9 and 4-10).

Two types of flow metering devices were used, one for high flow rates (from 200 to 4,700 ml/min) and one for low flow rates (from 10 to 200 ml/min). Metering and establishment of high flow rates were carried out using a constant-area flowmeter or a rotameter (Figure 4-9). Low flow rates were measured using an electronic J&W Scientific flowmeter capable of measuring flow rates to within ± 0.005 ml/min. The low flow rate was established using an 8-turn valve connected to the inlet side of the flow path (Figure 4-9).

The differential pressure drop across the specimen was measured with the Rosemont differential pressure transducer. The pressure drop was recorded either with a calibrated chart recorder or a Fluke hydra data logger, enabling the data to be directly downloaded to a spreadsheet for inspection and use.

Static-flow-rate tests were conducted in both the forward and reverse flow directions. In each test, the flow rate was established, and the pressure differential was recorded for a minimum of 10 to 15 min to attain equilibrium or steady-flow conditions.

A total of 34 flow rates versus pressure differentials was measured in the forward and reverse directions.

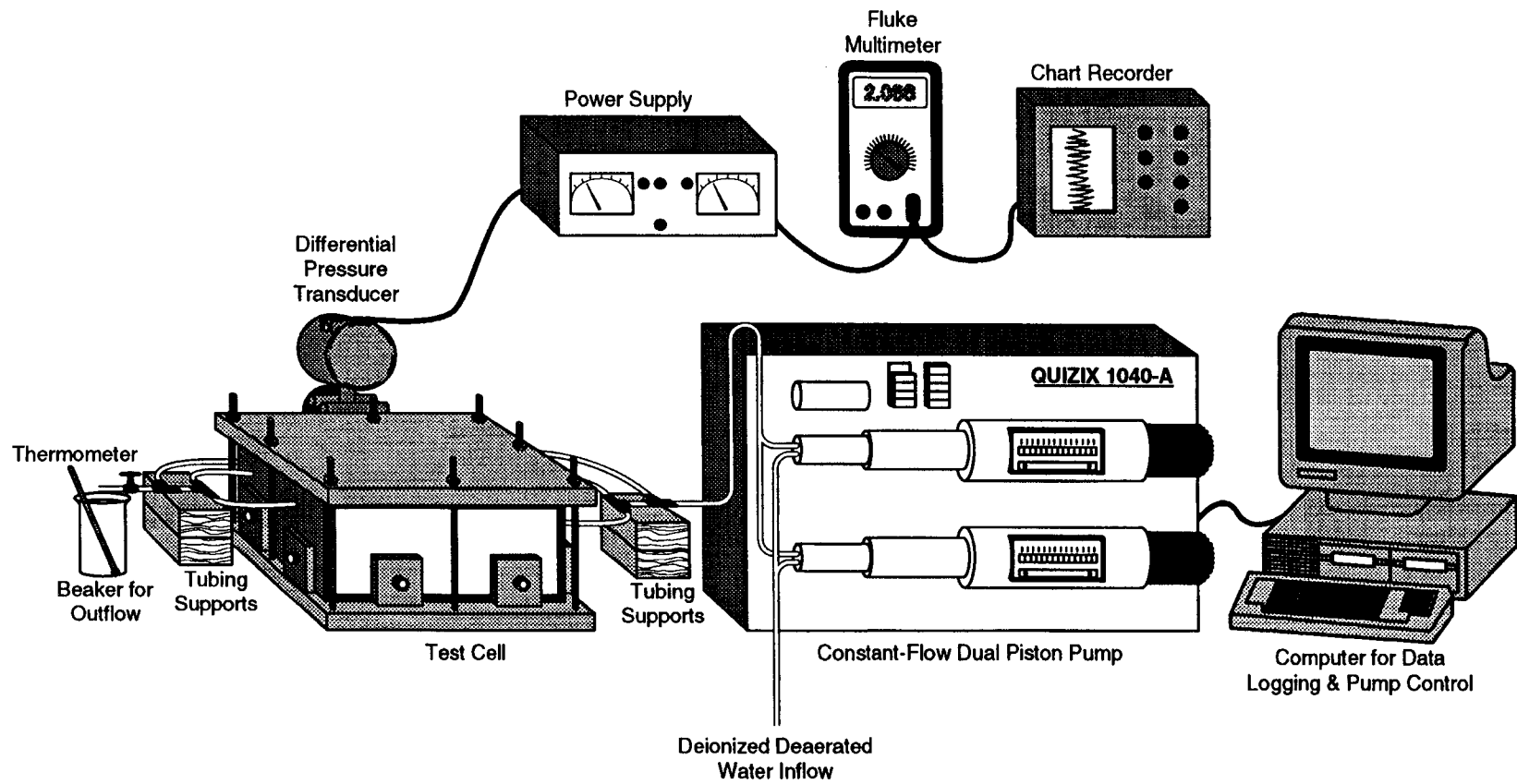


Figure 4-8. Schematic of liquid-saturated fracture flow experimental apparatus

4-15

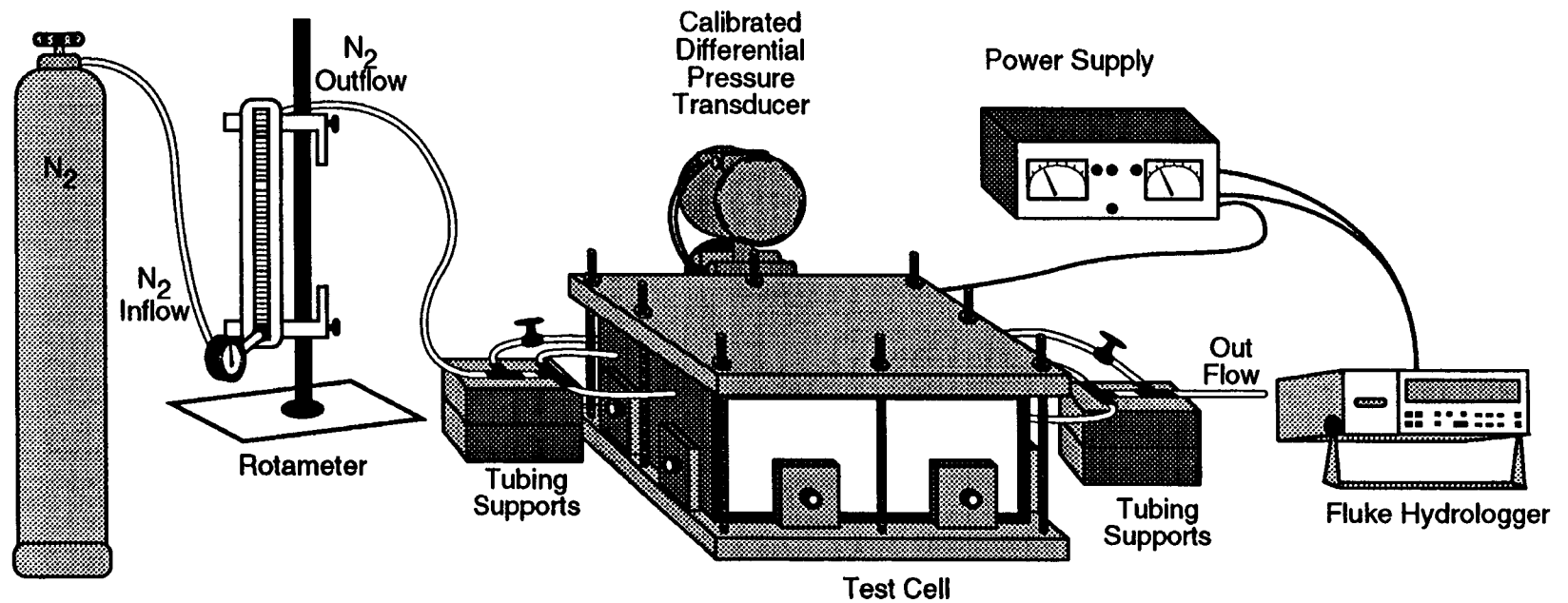


Figure 4-9. Schematic of pneumatic fracture flow experimental apparatus using a constant-area flowmeter

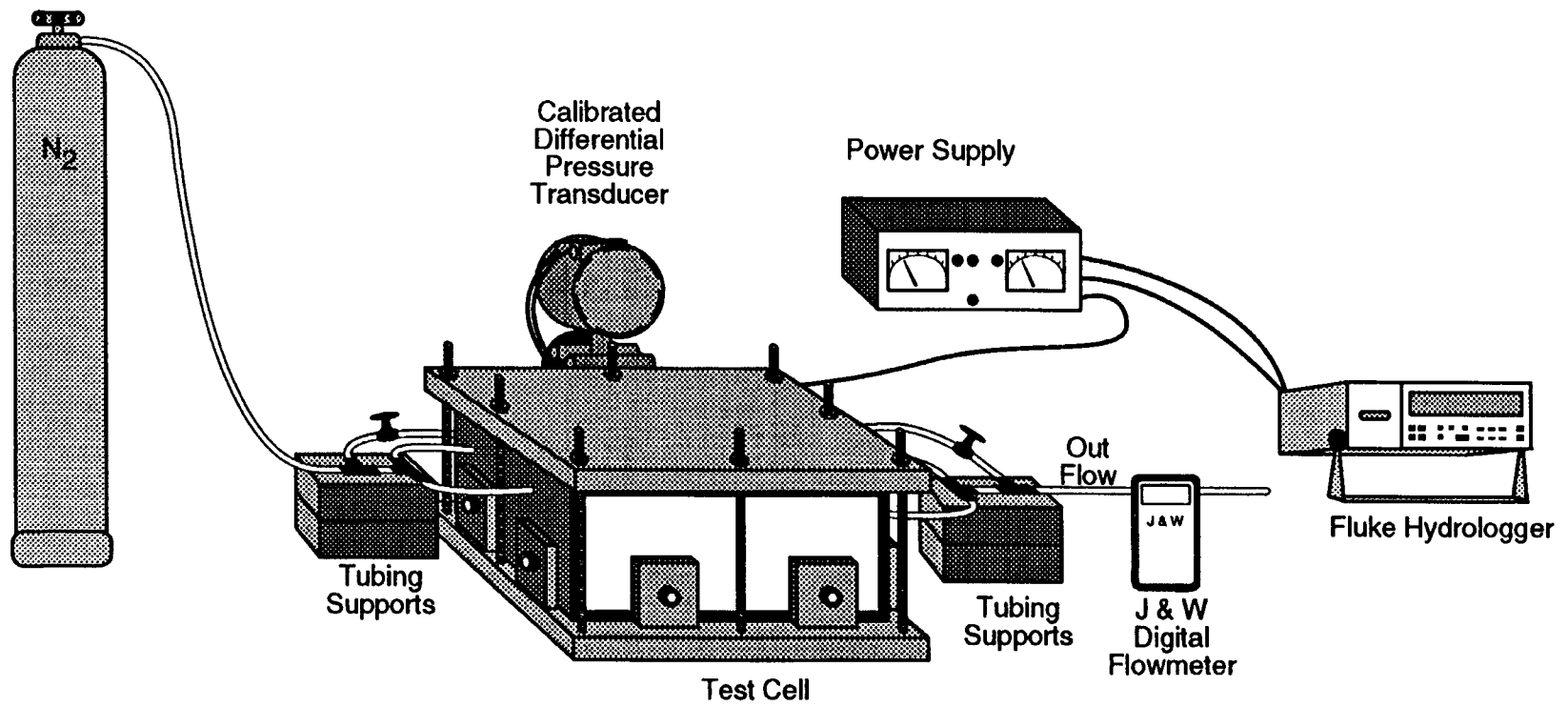


Figure 4-10. Schematic of pneumatic fracture flow experimental apparatus using a J&W scientific flowmeter

5 RESULTS AND DISCUSSION

This chapter presents results from the auxiliary experiments on fracture flow and fracture permeability determination. A comparison is made between pycnometer and fracture flow methods for fracture volume measurement. The effect of disturbing a fractured rock mass on fracture hydraulic properties is also investigated. Data from the noncontacting profilometry for an example test specimen are presented and the change in flow path under imposed normal load is investigated. Finally, the influence of rock dilation in the event of a shear displacement is numerically investigated.

5.1 RESULTS FROM AUXILIARY EXPERIMENTS

The average aperture of the fracture in a single rock specimen was calculated from pycnometer measurements. Two types of pycnometer measurements, positive pressure and vacuum, were used to determine the total void volume of the test cell. The total void volume of the test cell consisted of the inlet and outlet manifold volumes, the volume of the tubing, and the volume of the fracture. The combined volume of the manifolds and the tubing was measured independently with the pycnometer and determined to be $2.07 \times 10^{-5} \text{ m}^3$. Subtracting this volume from the total volume resulted in the fracture volume.

Three positive and three vacuum pycnometer tests were conducted on the block. The six total fracture volume measurements are summarized in Table 5-1. The rock block and test container were not altered or disassembled throughout the pycnometer tests to ensure that the fracture aperture remained constant during the six measurements. The average fracture volume was calculated from the six fracture volume measurements to be $5.01 \times 10^{-5} \text{ m}^3$. This volume corresponds to an average aperture of $1.2 \times 10^{-3} \text{ m}$ for the 20.3-cm-long and 20.3-cm-wide fracture. If the fracture is assumed to be two smooth parallel plates, fracture permeability can be estimated using the measured average aperture and the cubic law [Eq. (2-2)] to be $1.2 \times 10^{-7} \text{ m}^2$.

5.1.1 Liquid and Gas Fracture Flow Test Results

The drop of pressure across the fracture was measured over a range of flow rates in liquid and gas flow experiments to determine permeability. Liquid flow rates were varied from 0 to 120 mL/min with corresponding pressure differentials as high as 25 cm H₂O. Gas flow rates were varied up to 250 mL/min with resulting pressure differentials of less than 0.25 cm H₂O. The pressure differential was measured at the inlet and outlet manifolds of the rock block during both forward and reverse flow across the fracture. These opposing direction experiments were conducted by simply reversing the direction of fluid flow through the fracture. Additionally, both static and variable flow tests were conducted. Static tests were conducted to measure the pressure differential over a range of specified constant flow rates. Alternatively, variable flow tests were conducted in which the pressure differential was measured at flow rates that were initially increased and then decreased at a uniformly varying rate. The flow rates in the variable flow rate tests were either increased or decreased at a sufficiently low rate to allow the assumption of instantaneous steady flow in response to the change in pressure differential. The variable flow tests are thereby assumed to be equivalent to the static tests over a range of pressure differentials and flow rates. The rock block and test container were not altered or disassembled throughout the duration of the flow experiments to ensure that the fracture aperture and the flow pathways remained constant during the tests. Pressure differential measurements for both the forward and reversed liquid flow experiments at static conditions are illustrated in Figure 5-1. Similarly, pressure differentials observed during the variable liquid flow tests are illustrated in Figure 5-2. Recorded data corresponding to the figures are presented in Appendices A and B. Pressure

Table 5-1. Pycnometer pressure and volume data

| Total Void Volume | | | | |
|---------------------|--------------------|------------------|--------------------------------------|------------------------------------|
| Experimental Method | Initial Press (Pa) | Final Press (Pa) | Pycnometer Volume (cm ³) | Fracture Volume (cm ³) |
| Positive Pressure | 69943 | 54633 | 69.73 | 49.03 |
| Positive Pressure | 69754 | 54216 | 71.30 | 50.60 |
| Positive Pressure | 78519 | 61082 | 71.00 | 50.30 |
| Vacuum Pressure | 94493 | 73546 | 70.90 | 50.20 |
| Vacuum Pressure | 94525 | 73587 | 70.80 | 50.10 |
| Vacuum Pressure | 94538 | 73594 | 70.80 | 50.10 |

differential was measured only statically in the gas flow tests. Results from the gas flow tests are illustrated in Figure 5-3.

The liquid static and variable flow tests provided similar results, with the exception of the step pressure differential decrease observed in three of the forward variable flow tests. In all other liquid flow tests, a monotonic change in pressure differential was observed. However, in the three separate but simultaneous forward liquid flow tests, a step decrease in the pressure differential was observed when flow was increased above 30 mL/min. After the flow was increased above this rate in these tests, the pressure differential suddenly decreased from about 6.8 to 5.0 cm H₂O, after which the pressure differential increased monotonically for the duration of the test (i.e., up to 60 mL/min). The flow rate/pressure differential relationship observed after the step decrease in pressure differential in this series of forward variable flow tests was closer to those relationships observed in a second set of forward liquid variable flow tests, all the reverse variable flow tests and both of the static flow tests, than the relationship observed prior to the step decrease. The repeatability of the step phenomenon in the three tests suggests that an actual physical mechanism is observed. The pressure differential is attributed to an obstruction in the primary flow pathway. Although the source of this obstruction has not been positively identified, it is likely that the absence of the primary flow path during these tests resulted from the inadvertent presence of gas bubbles situated in the larger sized apertures of the primary pathway. The primary pathway may have been established in these tests only when the flow rate exceeded a minimum threshold level that could fully saturate the entire pathway. Upon exceeding this threshold flow level, the establishment of the primary pathway allowed the pressure to drop. Similar flow behavior has been observed elsewhere in partially saturated media (Green et al., 1995). It should be noted that the specimen was vacuum saturated before the water-flow experiments were conducted. The step decrease in pressure differential was not observed when the flow direction was reversed. Also, the step decrease in the pressure differential observed in liquid flow tests was not repeated after the conduct of the gas flow tests. This lack of repeatability suggests that the obstruction observed during the first series of forward liquid flow tests was not present during the second series of forward liquid flow tests.

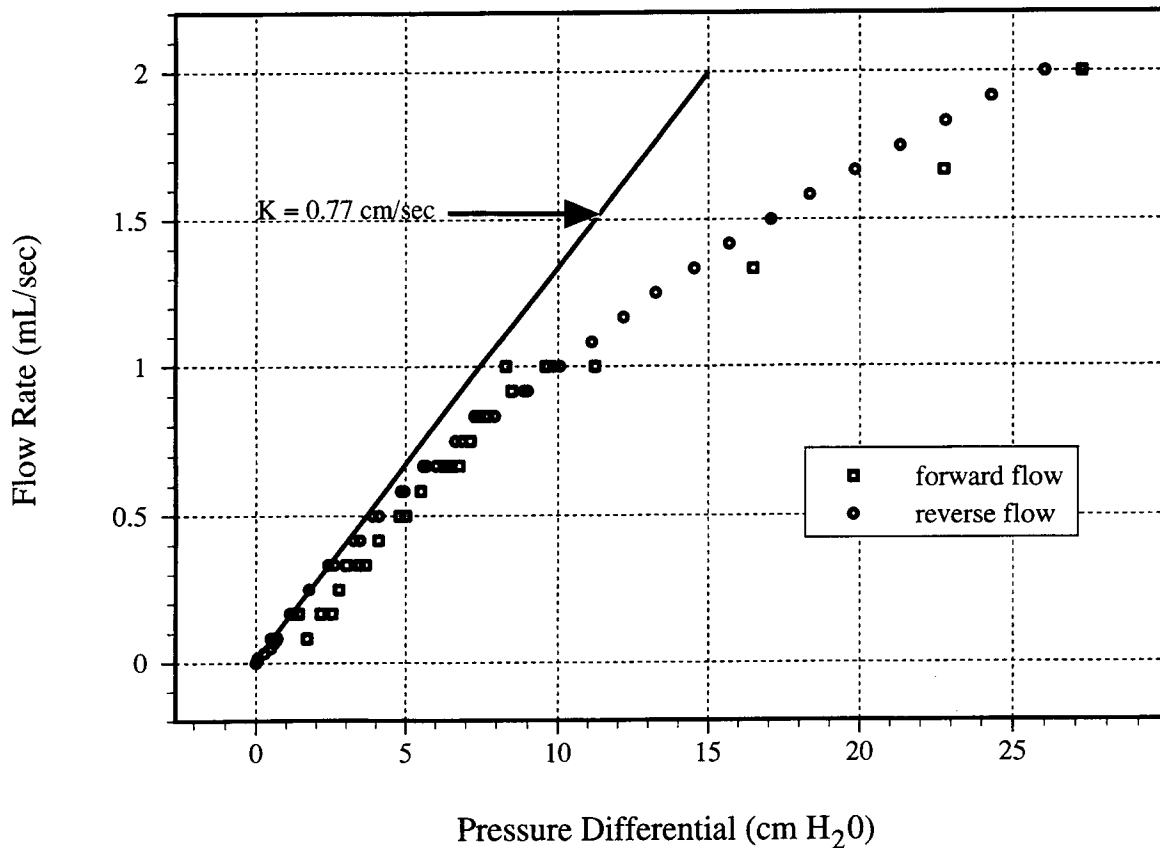


Figure 5-1. Steady-state flow rate versus pressure differential across the fracture during forward and reverse water flow

The permeability of the fracture was calculated from those liquid and gas flow measurements determined to be representative of a laminar flow regime. Turbulence was indicated in those flow rate/pressure differential relationship results in which the observed results departed from linearity. Turbulence was evident in liquid flow rates that exceeded 10 to 20 mL/min; therefore the liquid permeability was calculated from results at flow rates less than 10 mL/min. Data collected during both the flow rate increase and decrease in the variable flow tests were used in the permeability calculations. The fracture permeability values calculated using liquid flow test results varied from 5.7×10^{-10} to 1.9×10^{-9} m². Pressure differential measurements made during the gas flow tests appeared to be laminar at flow rates up to 200 mL/min. There was no appreciable difference in the observed pressure differentials between the forward and reverse gas flow tests. The fracture permeability to gas of 2.5×10^{-9} m² was calculated using the results from both the forward and reverse flow tests. The fracture permeability values calculated from the gas and liquid flow tests are summarized in Table 5-2.

The measured fracture permeability values are approximately a factor of 100 less than the permeability estimated using the measured aperture values and the cubic law. The discrepancy can be attributed to tortuosity and surface roughness. This discrepancy is consistent with other laboratory-based fracture flow experiments in which measured fracture permeabilities were significantly less than that predicted with the cubic law (Shrauf and Evans, 1984).

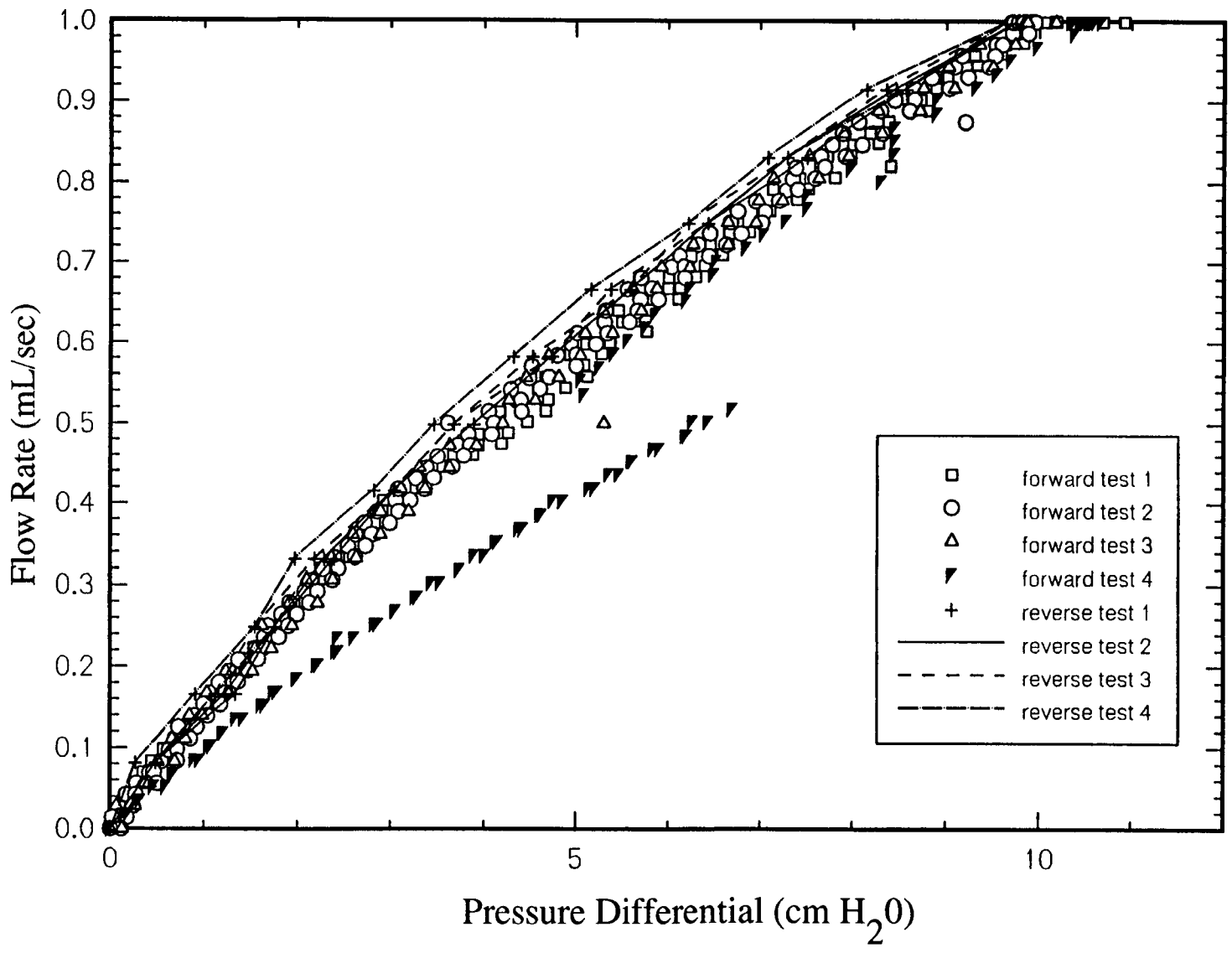


Figure 5-2. Water flow rate versus pressure differential across the fracture with respect to a constantly increasing flow rate

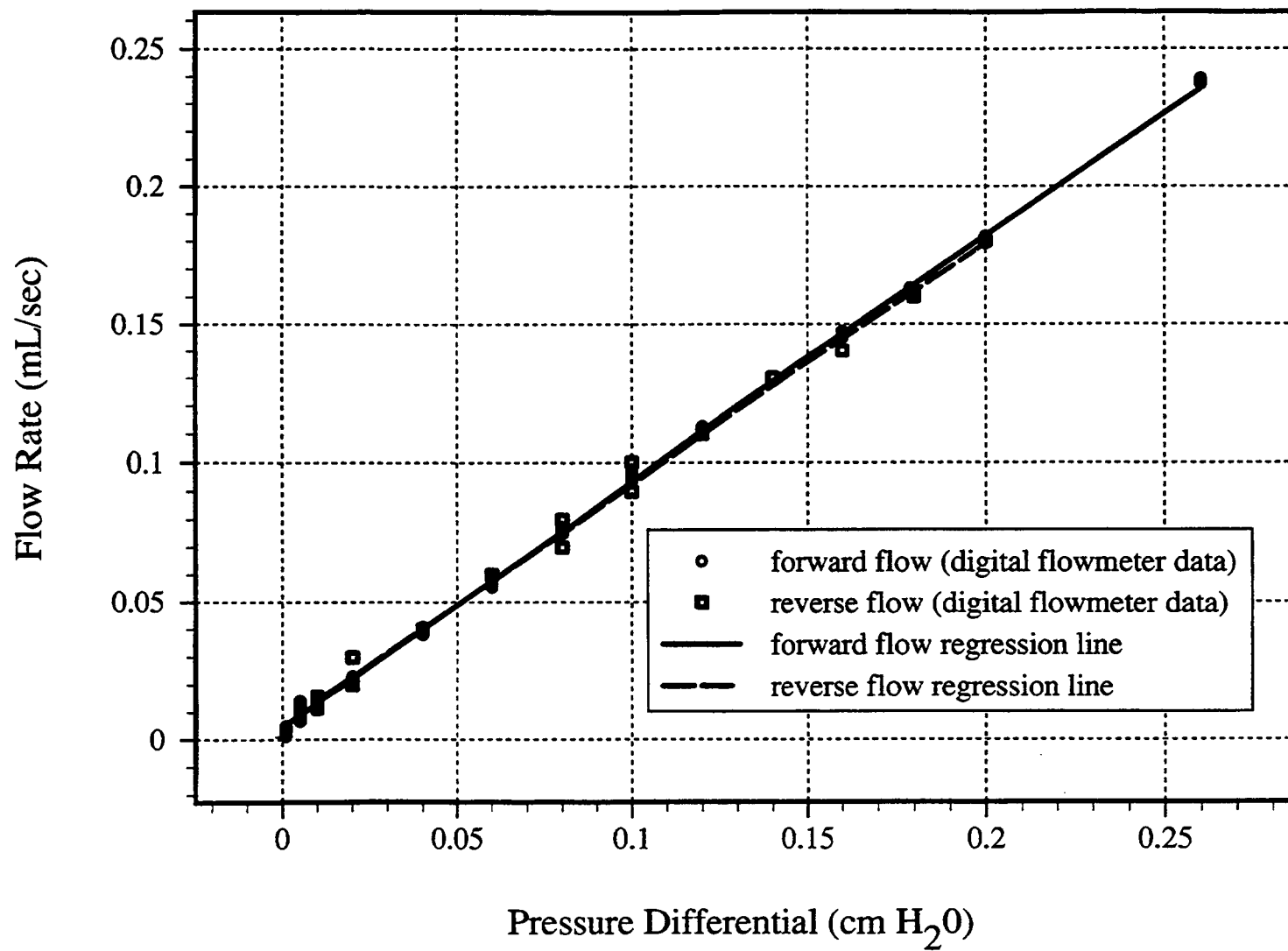


Figure 5-3. Steady-state flow rate versus pressure differential across the fracture

Table 5-2. Fracture permeability (m²) calculated from gas and liquid flow tests

| Liquid | | | |
|-----------------------|-----------------------|----------------------|----------------------|
| Static | | Variable | |
| Forward | Reverse | Forward | Reverse |
| 5.7×10^{-10} | 8.5×10^{-10} | 1.4×10^{-9} | 1.9×10^{-9} |
| Gas | | | |
| Static | | Variable | |
| Forward | Reverse | Forward | Reverse |
| 2.5×10^{-9} | 2.5×10^{-9} | n/a | n/a |

5.1.2 Effect of Forced Splitting of Fractured Specimen on Permeability

Experiments were conducted to study alteration in fracture flow characteristics when the jointed rock mass was disturbed from its original form in which it existed in nature. By disturbing the rock, we imply that the two faces of the joint specimen originally held together presumably by means of cementitious material were physically detached from each other.

A smaller specimen, 4.10 cm long and 7.76 cm in diameter, was used for this test. This specimen was cored from a large block of ALT, and the coring was done selectively such that the two sides of the fractured rock mass would be held together by the pre-existing cementing material. The loose materials generated due to the process of detaching were not disturbed. The fracture permeability was measured by using an existing permeameter generally used for measuring intact rock mass hydraulic conductivity. In this apparatus, the fluid injection took place across the whole cross-sectional area of the specimen and not just in the neighborhood of the fracture entrance. The injected fluid was distributed across the whole cross-sectional area of the inlet end because of the interconnected concentric grooves engraved into the end plate. A similar arrangement was performed at the outlet end. The rock matrix had extremely low hydraulic conductivity compared to the fracture, and the rock mass was fully saturated with the injected fluid. Therefore, the fluid was expected to flow exclusively through the fracture.

Experiments were conducted at various confining pressures, varying from 30 to 90 psi. The relationships between steady-state pressure drops along the length of the fracture and the flow rates are presented in Figure 5-4. Similar relationships for the specimen after the split are presented in Figure 5-5 for various confining pressure varying between 10–70 psi. Higher confining pressure could not be applied because of the pressure limitation of the experimental apparatus.

In Figure 5-4, the fluctuation in the data prevents one from seeing any pattern in the effect of confining pressure on hydraulic conductivity. In Figure 5-5, though a definite pattern is seen, the trend

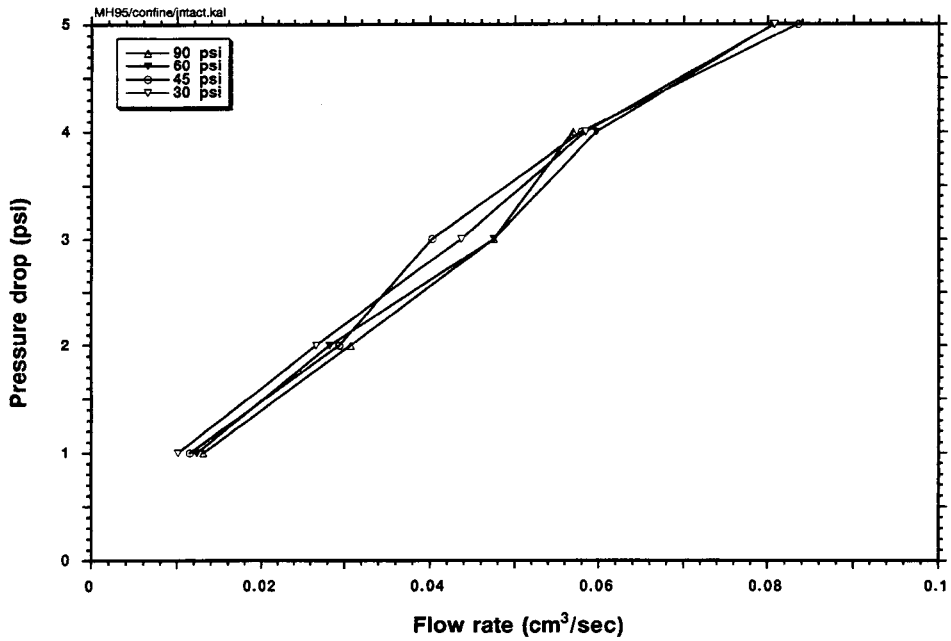


Figure 5-4. Flow rate versus pressure drop across a fracture at low confining pressures varying between 30 and 90 psi for an unsplit natural fracture

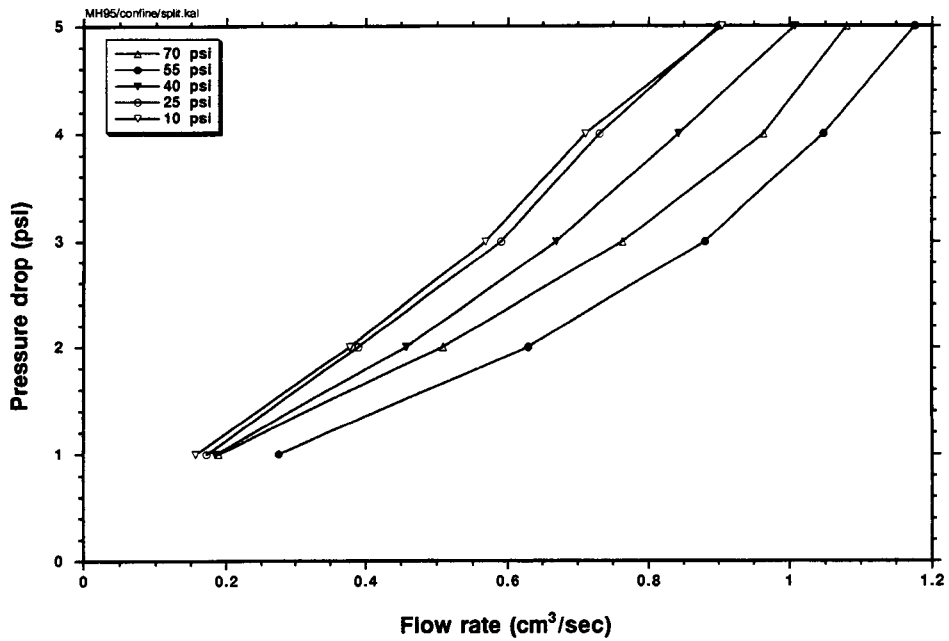


Figure 5-5. Flow rate versus pressure drop across a fracture at low confining pressures varying between 30 and 90 psi for a split natural fracture

is counter intuitive. It may be suggested that the debris formed due to the splitting of the specimen is clogging the flow path. When the confining pressure is released, the debris is likely to move under the pressure gradient and become captured in the fracture toward the downstream of the flow. An order of magnitude increase in permeability was observed after splitting the specimen. We did not expect to see much of a definitive behavior because the confining pressure is small in magnitude. Nonetheless, this test compares the hydraulic conductivity of the rock joint before and after splitting.

5.2 ANALYSIS OF APERTURE DATA

The mechanical characteristics of jointed rock are typically studied by relating joint surface roughness and joint matedness data to the imposed loading conditions. Similarly, hydrologic characteristics are related to the loading conditions through the joint aperture data. It is therefore intuitive to study MH coupling by relating aperture distribution to the surface roughness data, possibly through functional relationships. Various measures of surface roughness have been proposed including the root mean square (Z_2 parameters) approach (Myers, 1962; Tse and Crudden, 1979) to predict JRC, autocorrelation function based approach (Wu and Ali, 1978), fractal dimension approach (Brown and Scholz, 1985; Carr and Warriner, 1989; McWilliams et al., 1990). These methods are based on the analysis of individual roughness profiles. Another method is based on the geostatistical method, which could offer properties based on 2D and 3D topographical profiles, thus taking into account directional anisotropy.

In the geostatistical approach, the surface heights are used as random variables for characterizing surface roughness whereas aperture widths are used for characterizing the flow field. One of the most commonly used estimates in the field of linear geostatistics is the semivariogram function $\gamma(\mathbf{h})$ for all directed distances \mathbf{h} . The semivariogram describes the spatial continuity of the phenomenon studied. The experimental semivariogram $\gamma(\mathbf{h})$ is half the expected squared difference between random variables $Z(\mathbf{h})$ separated by a specified lag distance \mathbf{h} . For a set of N datapoints within an area of interest, the usual semivariogram estimator is

$$\gamma(\mathbf{h}) = \frac{1}{2N} \sum_{i=1}^N [Z(x_i) - Z(x_i + \mathbf{h})]^2 \quad (5-1)$$

where N is the number of pairs of data separated by the vector \mathbf{h} . In our case, we consider the surface height from the reference as the random variable of interest for surface roughness and the aperture thickness as the random variable of interest for aperture distribution. The variogram increases with the lag distance and eventually tends toward an asymptotic value. The semivariogram value corresponding to the asymptotic region is called the sill of the variogram. The sill value of the variogram is also the variance of the random function. The lag distance at which the variogram reaches its asymptotic value is called the range. When the phenomenon under consideration does not have a finite variance, the variogram will never have a horizontal asymptotic value.

5.2.1 Analysis of Apache Leap Tuff Profile Data

Using surface height data obtained for the top and bottom layers, the aperture data were obtained by the method described in Chapter 3. The four vertical sides of the ALT specimen of rectangular shape are shown in Figure 5-6. In addition to showing the heterogeneity in the rock mass, this figure also gives a 2D visual impression of the fracture aperture size, large-scale variation, and fracture continuity. The surface height profiles with respect to a reference plane for both the surfaces constituting the fracture are

presented in Figure 5-7. The spatial distribution of aperture obtained by using the two surface height profiles is also presented in the same figure. A maximum aperture value of 1.59 mm and a minimum aperture value of 0 mm were obtained. A few scattered data points were negative values. Therefore, a zero cut-off was enforced to remove all the negative numbers. The scatter and density of these data points representing negative values are shown in Figure 5-8. Less than 4 percent negative numbers were observed, and the aperture distribution consisted of 9,900 data points. However, the percentage of such data can be considered to be very small. The histogram of aperture distribution in the fully matched condition is shown in Figure 5-9. A mean aperture value of 0.21 mm was observed, and a standard deviation of 0.14 was observed. From the histogram of aperture distribution, it appears that a log-normal aperture distribution exists.

In our test, semivariograms were plotted for three different random fields: upper surface heights, lower surface heights, and aperture distributions. The semivariogram for the aperture distribution in the horizontal direction is presented in Figure 5-10. In this figure, the semivariogram is plotted as a function of lag distance. It reveals that there is a clear correlation length associated with the aperture distribution. The correlation length appears to be 12 pixel lengths (0.48 mm). The unusually high value at larger lag distances is an artifact of the semivariogram approach due to the boundary effect and does not indicate the existence or nonexistence of a different correlation structure at larger length scale. It should be noted that the fracture used in this case was a clean fracture freshly induced in a rock. The joint specimen collected from the field may indicate a different geometric description compared to a fresh fracture. Fracture specimens collected from the field as well as fresh fractures most often show weak spots on the fracture faces from which the rock materials easily chip off. Some of the large apertures in the aperture distribution may correspond to a few such areas from which the rock may have chipped off. The rock chip-off is quite evident from the aperture distribution presented in Figure 5-11 for a different rock sample. An elongated large-aperture streak seen on this specimen is the region on the fracture face from which loose material had been removed before scanning the rock. This removal will inevitably change the geometric characteristics presented in Figure 5-9.

From the aperture data obtained from surface profilometry, the contact between the top and bottom block appears to be point contacts. These contact points are shown in Figure 5-8. In this figure, the aperture distribution has been converted to a binary image in which the black pixels represent contact areas (zero aperture) and the grey region represents the regions with aperture greater than zero. In order to observe the pattern of change in the contact area, the top block was numerically moved toward the bottom rock in step-wise increments of 0.1 mm. The change in contact area has been presented in Figure 5-12 for changes of 0.1, 0.2, 0.3, 0.4, and 0.5 mm. From these values, it is apparent that under vertical displacement, the scattered contact areas at zero cutoff (corresponds to no normal load) grow in size, and new scattered contact areas develop as the greater normal displacement is allowed. Thus, the point contacts grow out to be area contact, and surfaces previously available for fluid flow are now in touch with each other. As a result, the area available for fluid flow overall will decrease. Clearly, at a cutoff of 0.2 mm, the flow paths begin to be more disconnected because of the increase in cluster size of the pixels constituting contact areas. At the cutoff of 0.3 mm, connected flow paths in the fracture no longer exist. With the increasing stress, the original flow paths will become constricted, and pools of water that were originally a part of the flow path will now become almost isolated, with perhaps only one connection with the flow stream. The number of paths carrying water will gradually decrease as the stress level is increased, and those pools of water that had only one connection will perhaps completely lose its connection with the flow stream. The increasing stress may separate the flow channels while simultaneously narrowing down. However, the extent to which such reduction will take place depends on the strength of the rock mass. Various investigators in the past have observed that, under normal stress,

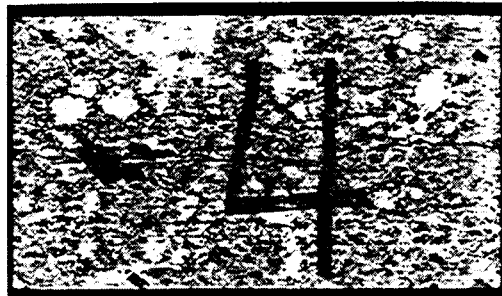
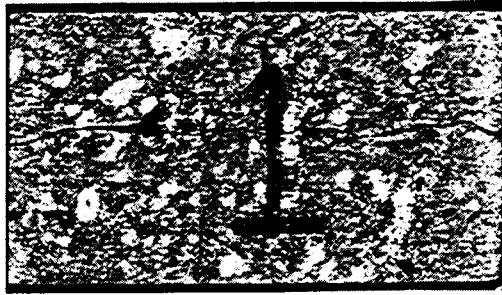


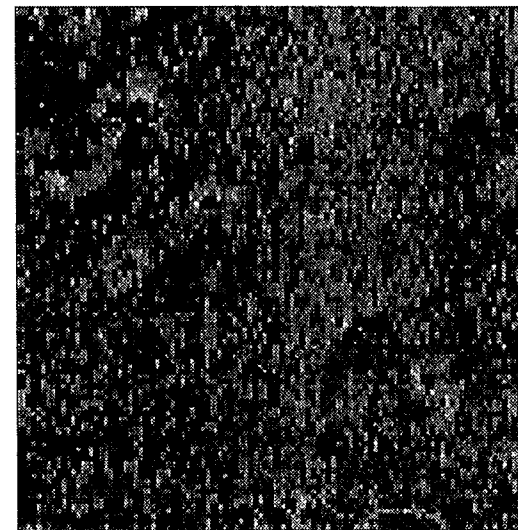
Figure 5-6. Photograph of the four vertical sides of a single rock mass (40×40×25 mm) containing a single fracture



Height (Top block)



Height (bottom block)



Aperture profile

Figure 5-7. Surface heights data collected from the two faces of a fractured rock. Dark areas and light areas represent high and low points, respectively. Also presented is the corresponding aperture data.

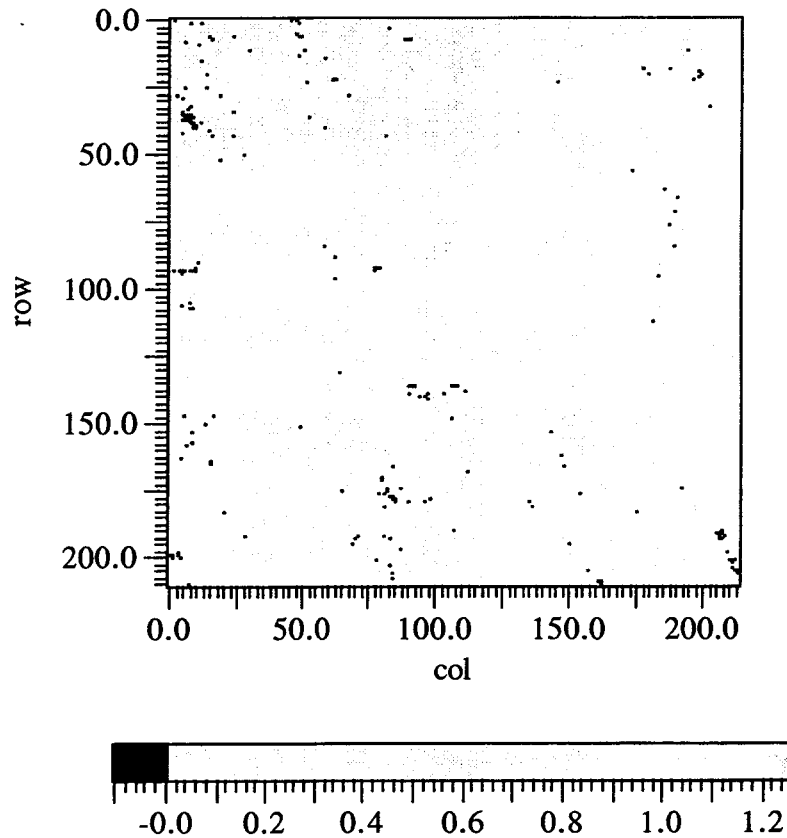


Figure 5-8. Sparsely distributed contact points between the two surfaces of the rock joint

the fracture apertures tend to completely close. Thus the flow would be limited only to the matrix flow. Our experimental data (Mohanty et al., 1994; 1995) suggest that the reduction in aperture width is only 35 percent for normal loads of up to 8 MPa.

In an effort to numerically study the effect of rock dilation due to shear, the top block of the joint was systematically displaced. Only translational displacement in a direction parallel to one of the joint edges was allowed. The fracture was allowed to dilate, thus resembling a condition of shear displacement under constant normal load. It was ensured that the top and the bottom rocks touched each other in at least one point. Another simplifying assumption made was that the top and the bottom surfaces of the jointed rock mass were parallel to each other at all displacements. No gouge production due to shear displacement was simulated. Absence of the production of gouge resembled a condition of rock mass having infinite strength.

Snapshots of aperture distributions obtained at intervals of 0.4 mm (i.e., one pixel length) intervals and with a maximum displacement of 2.4 mm (i.e., 6 pixel lengths) were studied. The top and bottom blocks were of the same length and width. Therefore, after each displacement, the size of the aperture field were reduced by two lines of aperture data. As seen from the semivariogram plot for the fully matched aperture distribution (Figure 5-10), the aperture distribution is isotropic, and the correlation length is nearly 16 pixel lengths (i.e., one sixth of the fracture length). Therefore, the reduction in field

size with numerical shear displacement is not expected to have a noticeable effect on the flow calculations that are described below.

The contour diagrams of the aperture fields at the end of each numerical shear displacement are shown in Figures 5-13, 5-15, and 5-17. Corresponding histograms of aperture distribution are presented in Figures 5-14, 5-16, and 5-18, respectively. While the gray scale in Figures 5-13, 5-15, and 5-17 show the aperture height variations, the contours superimposed on the grey scale image show the islands of aperture value. At the end of the 6-pixel-length displacement, the largest aperture width was observed to be 5.2 mm, and the smallest aperture value was maintained at 0 mm as described earlier. However, it was observed that the maximum change in the largest aperture value took place at the first numerical displacement step (2.3 times the initial largest aperture value) and then the change rapidly slowed down. With a final mean aperture value of 1.8 mm, the change in the mean aperture value for the same displacement condition was observed to be 7.6 times that of the original mean aperture. Similarly, with a standard deviation of 0.524 mm, the change with respect to the matched condition was found to be 2.55 times. The increasing trends in the above mentioned aperture characteristics as well as the change in aperture distribution can be clearly seen in Figures 5-13, 5-15, and 5-17. It appears that with the increase in numerical displacement, that is, with the increase in fracture face mismatch, the aperture distribution deviates from log-normality and tends to be more gaussian. At the maximum displacement (6 pixels), a hump in the histogram appears at the large aperture value, perhaps, suggesting a shift toward bimodal distribution.

While the aperture distribution in a matched condition appears to be isotropic, the displacement tends to develop large aperture streaks. These streaks appear to grow in size (with a simultaneous increase in aperture height in the streaks) with the displacement. These streaks will potentially contribute to the growth of an anisotropic flow path, such as flow channels. The position of these streaks coincide with the anisotropy in the surface height distributions in the top and bottom blocks of the jointed rock mass. In order to demonstrate the variation in surface height compared to the aperture widths, a row of data obtained by taking a cross section perpendicular to the fracture plane is shown in Figure 5-19. The two curves with large undulation represent the position of the two fracture faces, and the curve with only the small scale variation is the aperture width distribution. It should be noted that the y-axis in this figure has been stretched to show the details.

5.2.2 Effective Aperture Determination

The effect of the aperture distribution on the fluid flow in the fracture typically assumes a stepped profile as shown in Figure 5-20. The step sizes are typically determined by the profiler used in retrieving the aperture data. Ideally, a continuous profile can be obtained by using the surface-contacting stylus method. However, the noncontacting laser profiler implements discrete positioning of the source/detector assembly. The user assigns the spatial interval steps at which the data must be collected. Each position represents an area on the fracture face, and the surface heights within that area are averaged. Therefore, a single value is obtained. Since variations within this area are not recorded, the aperture corresponding to this area is assumed to be represented by parallel planes. The fact that each pixel represents an area average of the surface height data, the two surfaces of the fractures cannot be matched exactly at that scale. Thus, it comes as no surprise that nearly 4 percent of the data are negative, as mentioned in the previous section. Repeated experiments by using three different specimens and specimens of different sizes indicate that the number of negative aperture values are limited to 4 percent of the total points.

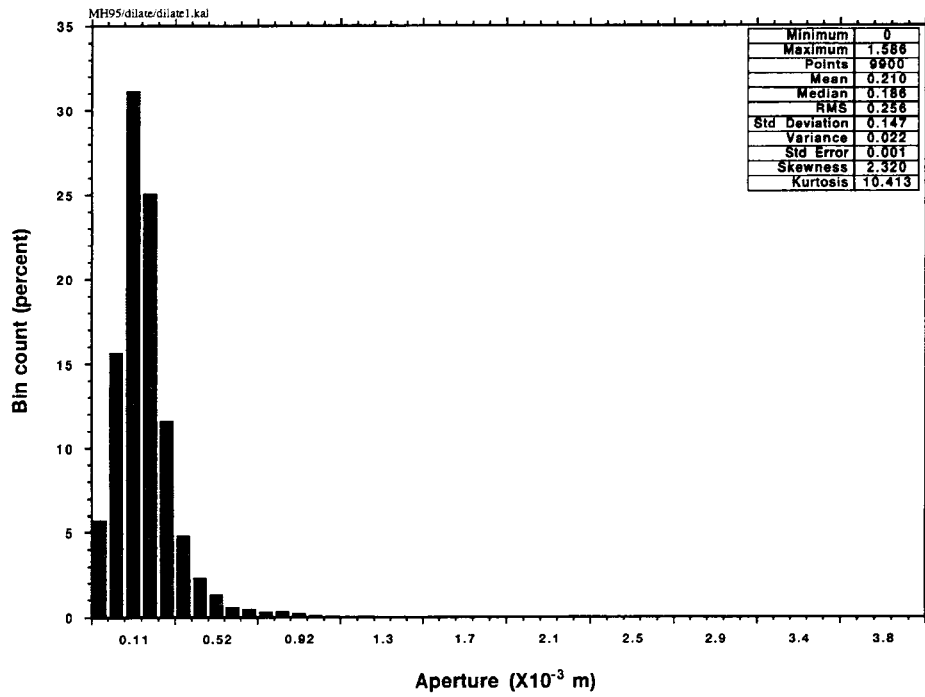


Figure 5-9. Histogram of joint aperture distribution presented in Figure 5-7. The aperture distribution appears to be approximately log-normal.

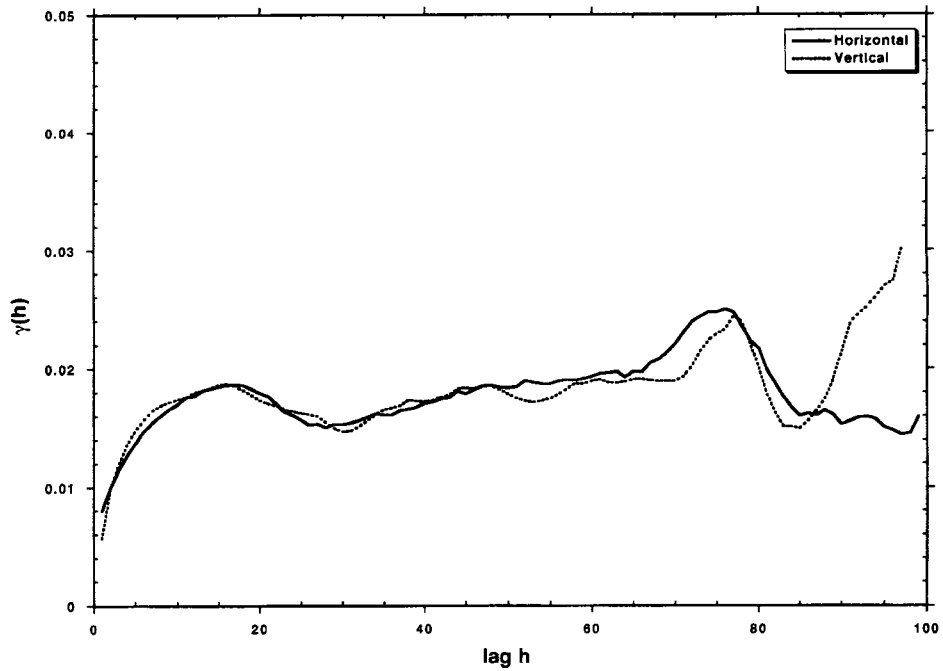


Figure 5-10. Semivariogram plot of the fracture aperture data showing stationary correlation length

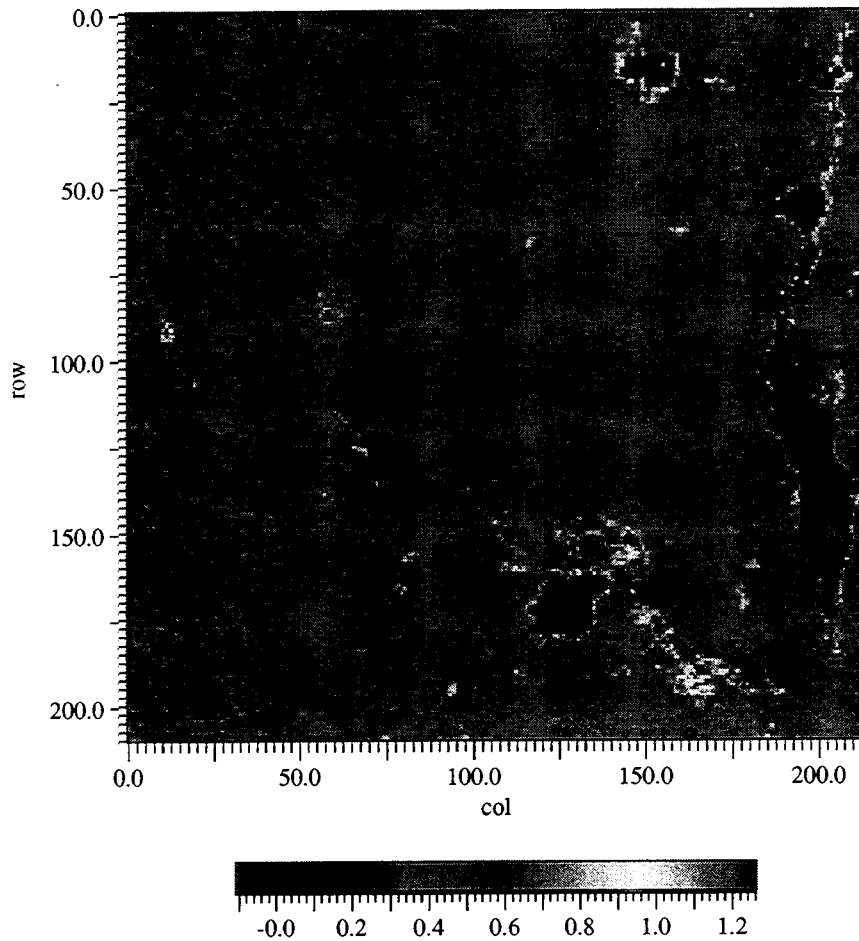


Figure 5-11. Aperture distribution showing rock chip-off, which could potentially distort the aperture statistics

In order to properly account for the tortuous flow path in our calculation, we have performed a steady-state flow simulation by using a fracture aperture distribution. In this flow simulation, a laminar, incompressible fluid flow has been assumed. A 2D flow simulation has been conducted by using a finite-difference simulation scheme. The flow takes place between the left and right faces of the aperture composite, as shown in Figure 5-21. Constant pressure boundary conditions have been applied at the inlet and outlet boundaries. This constant pressure is accomplished by keeping the pressure at all inlet node points identical and constant and also keeping pressures at all outlet end nodes constant at a value smaller than the inlet pressure. A unit pressure differential is applied between the inlet and outlet ends. Under steady-state flow conditions, the flow rates at each node at any one cross section perpendicular to the general flow direction are summed in order to determine the total flow rate. By assuming that an equivalent aperture for the aperture field exists, the equivalent flow resistance/conductance is determined from the Darcy's equation. Since the equivalent aperture is unknown, the fracture cross-sectional area is also an unknown. Therefore, by using the average flow rate and an imposed steady-state pressure drop, q/A is obtained from Darcy's law. Then, by using the equivalence between permeability and squared-aperture width relationship, the effective hydraulic aperture value is determined.

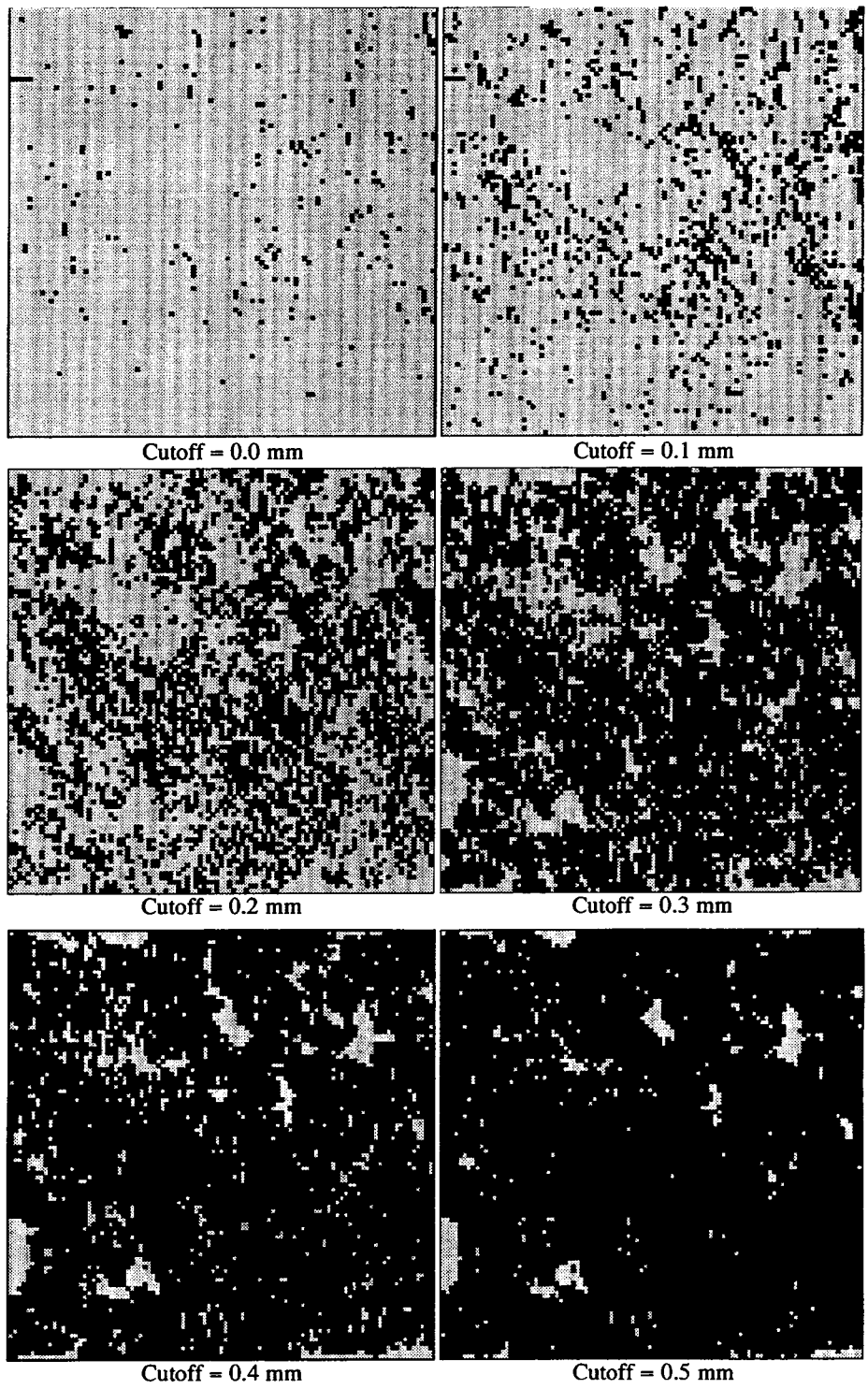


Figure 5-12. Sequence of the figures showing the geometric configuration of contact area at various interpenetrations of the two faces of the fractured rock. Cutoffs are arbitrarily chosen to demonstrate areas of contact.

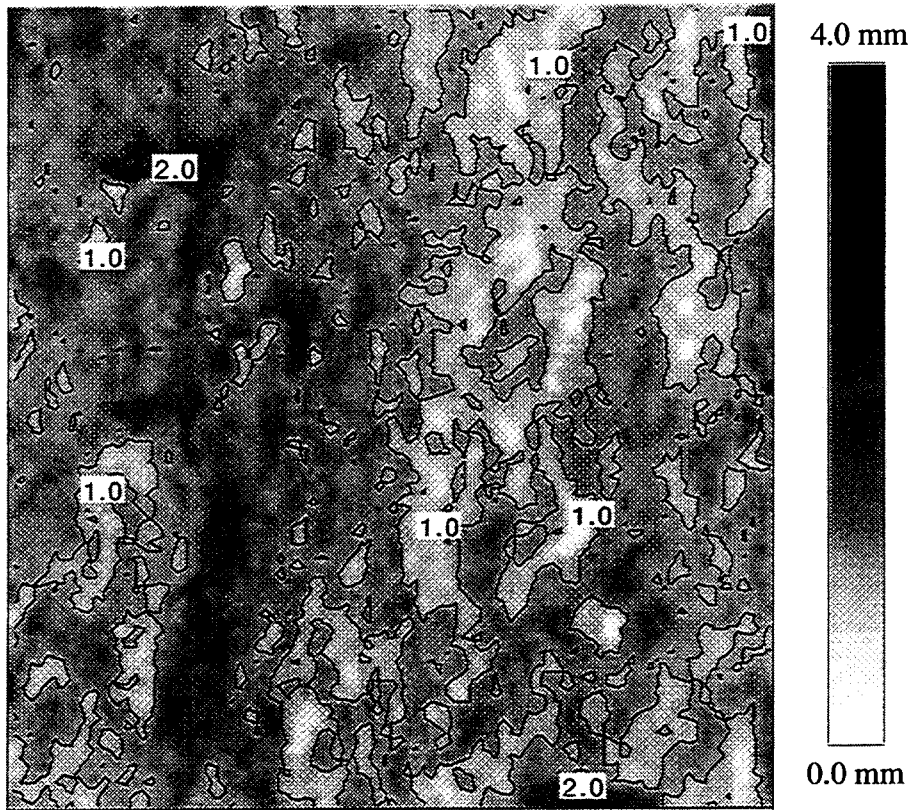


Figure 5-13. Aperture distribution of Apache Leap tuff under simulated no-load joint dilation. The top rock is offset with respect to the bottom rock by 0.08 mm (2 pixels) along the x-direction.

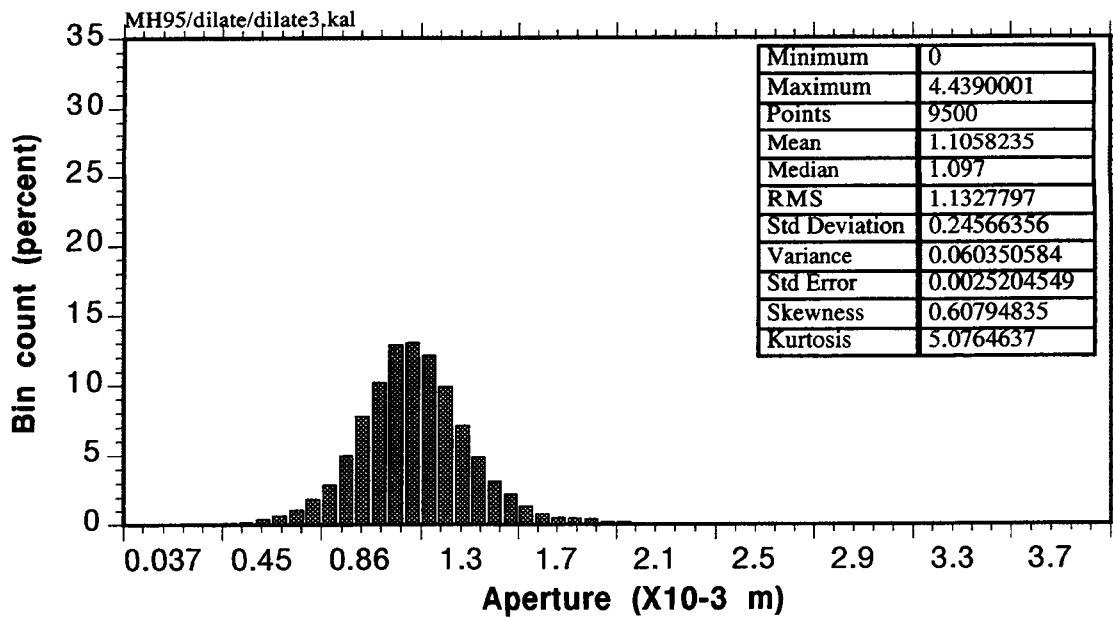


Figure 5-14. Histogram of aperture distribution corresponding to Figure 5-13

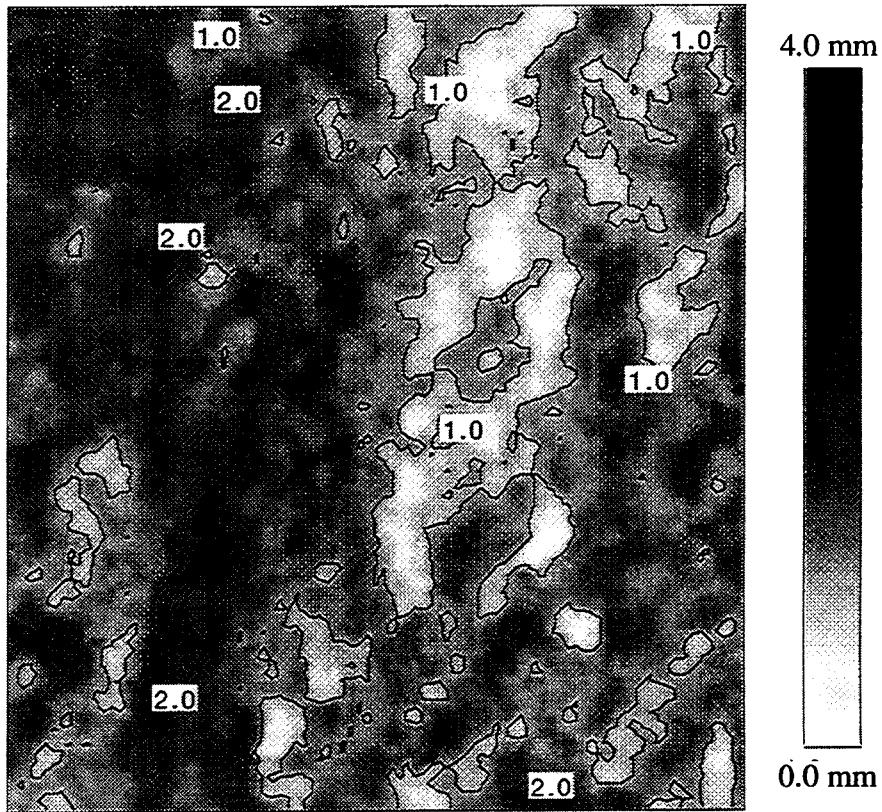


Figure 5-15. Aperture distribution of Apache Leap tuff under simulated no-load joint dilation. The top rock is offset with respect to the bottom rock by 1.6 mm (4 pixels) along the x-direction.

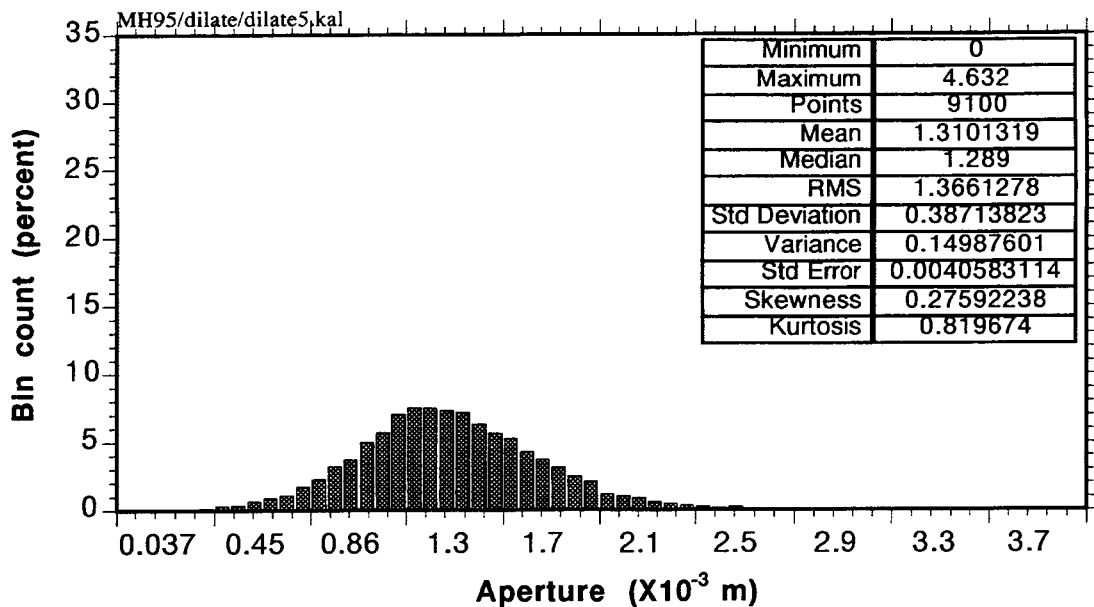


Figure 5-16. Histogram of aperture distribution corresponding to Figure 5-15

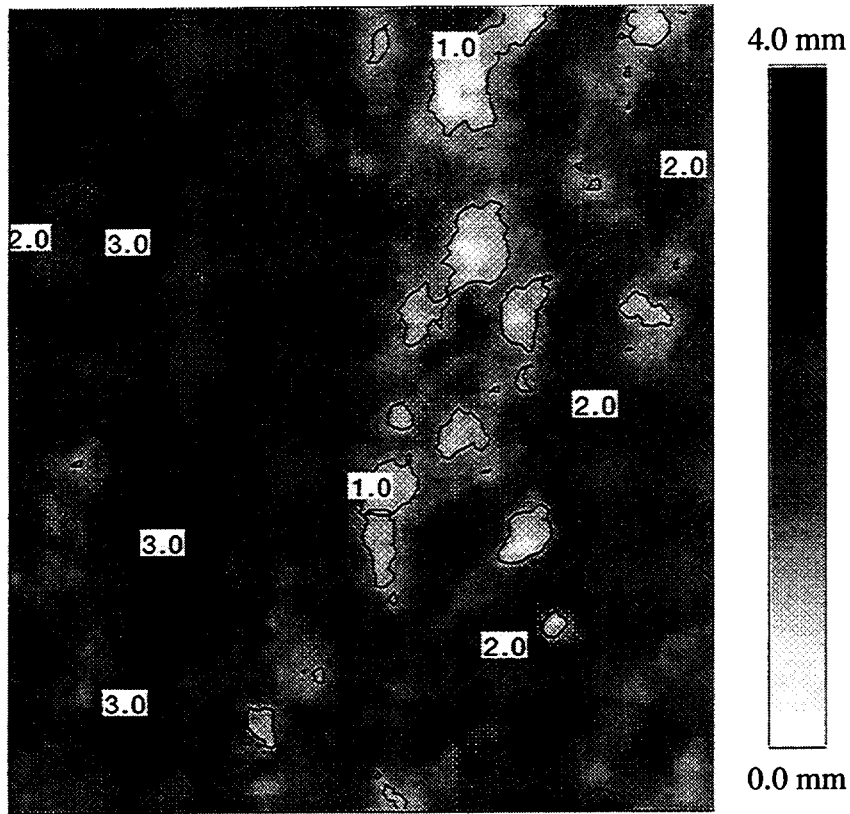


Figure 5-17. Aperture distribution of Apache Leap tuff under simulated no-load joint dilation. The top rock is offset with respect to the bottom rock by 2.4 mm (6 pixels) along the x-direction.

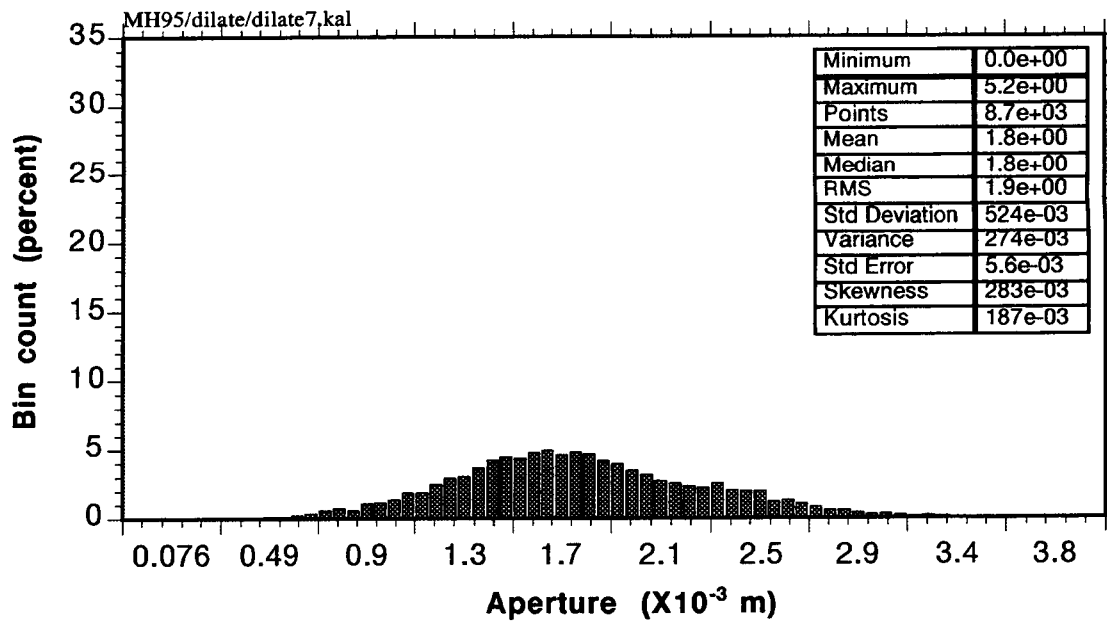


Figure 5-18. Histogram of aperture distribution corresponding to Figure 5-17

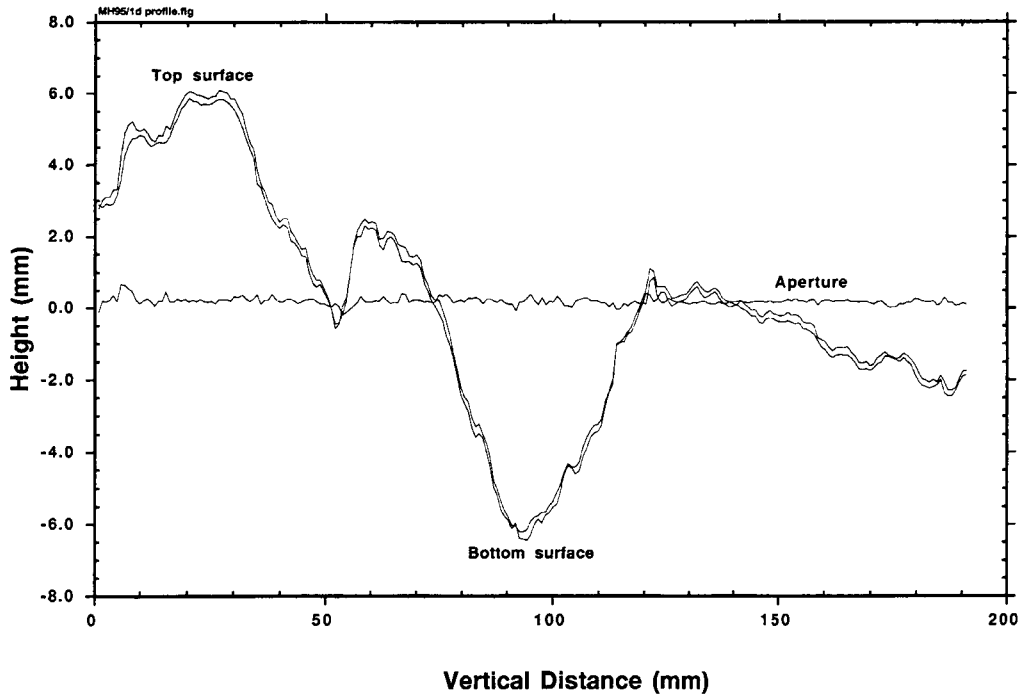


Figure 5-19. Fracture surface height data of a vertical cross section along the x-direction. The aperture data have been plotted along with surface height data to demonstrate the order of magnitude variation.

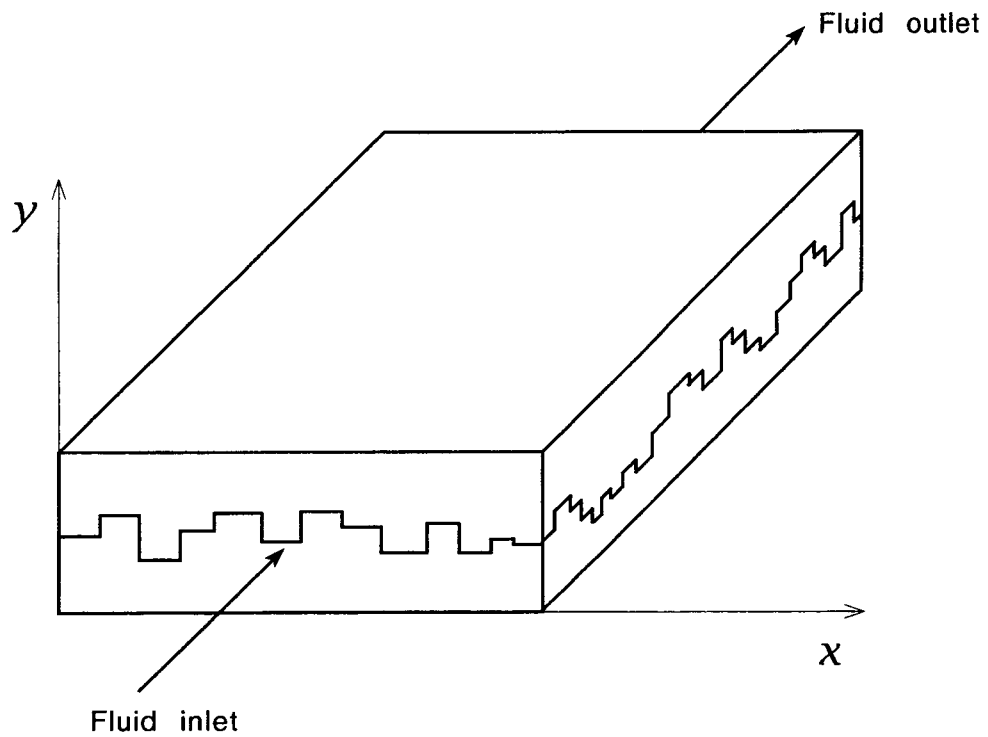


Figure 5-20. Idealization of the fracture face as a network of parallel plates

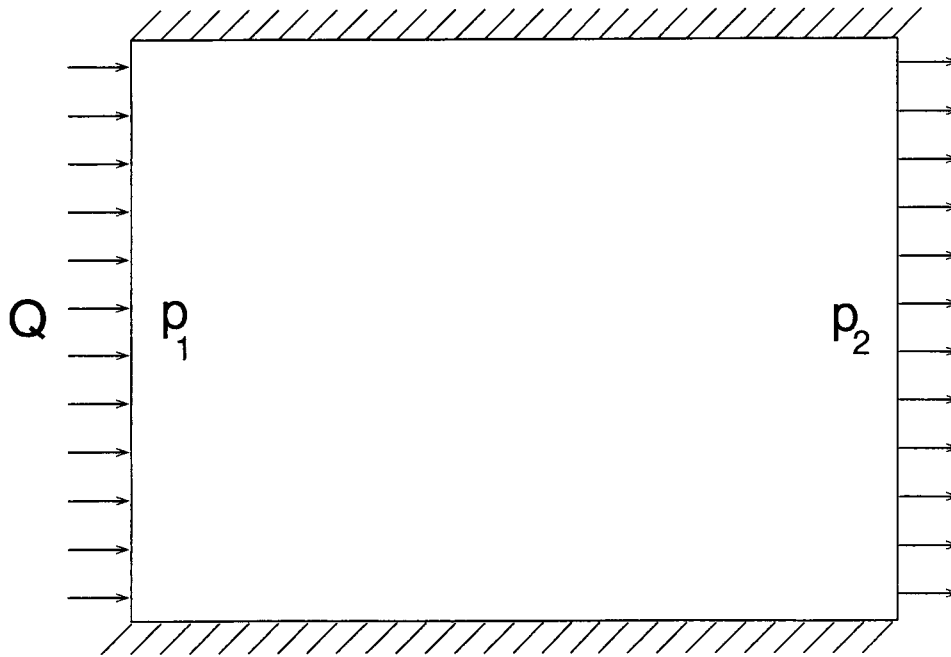


Figure 5-21. Imposed boundary condition for numerically determining the effective aperture of a given aperture field

Calculations have been conducted by using approximately 10,000 nodes on a square lattice. Since the calculations have been done in 2D, the relative positions of the aperture (as shown, for example, in Figure 5-19) in the z-direction were neglected, and the gravity effects were also neglected. The effects due to this simplification are expected to be insignificant as long as large wavelength surface roughness is absent.

To demonstrate the effect of aperture on the flow path, a steady-state flux field has been obtained by using a 100×100 aperture field (the fracture field obtained under best-matched condition). The flux field is presented in Figure 5-22. A similar flux field was also obtained by using a smaller portion (38×37) of the aperture field from Figure 5-22 in order to highlight the channeling effect (Figure 5-23). At the bottom left corner, three independent channels appear to merge together, and the converged flow takes place in a high permeability streak to the central region. The high-permeable streak ends there, and the flow tends to diverge in various directions. It could be anticipated that if the high permeability streak (i.e., preferential path) had spanned across the whole field to the outlet end, then the fluid flow would have been primarily a channel flow. In the last two illustrations, the flux fields have been superimposed on the permeability fields to verify that the fast path tracks the high permeability streaks.

By using the above procedure, fracture permeabilities have been computed along the flow direction (x-direction) and transverse to the flow direction (y-direction). Equivalent permeabilities have been obtained at various numerical shear displacements by translating the top rock in the x-direction. The x- and y-directional permeabilities are compared in Figure 5-24. For convenience, the dilation corresponding to the displacement steps has also been presented. Results from a physical experiment conducted by Piggott and Elsworth (1990) are presented in Figure 5-25. In this experiment, the fracture faces were mismatched in order to mimic a dilated condition under shear. More than two orders of

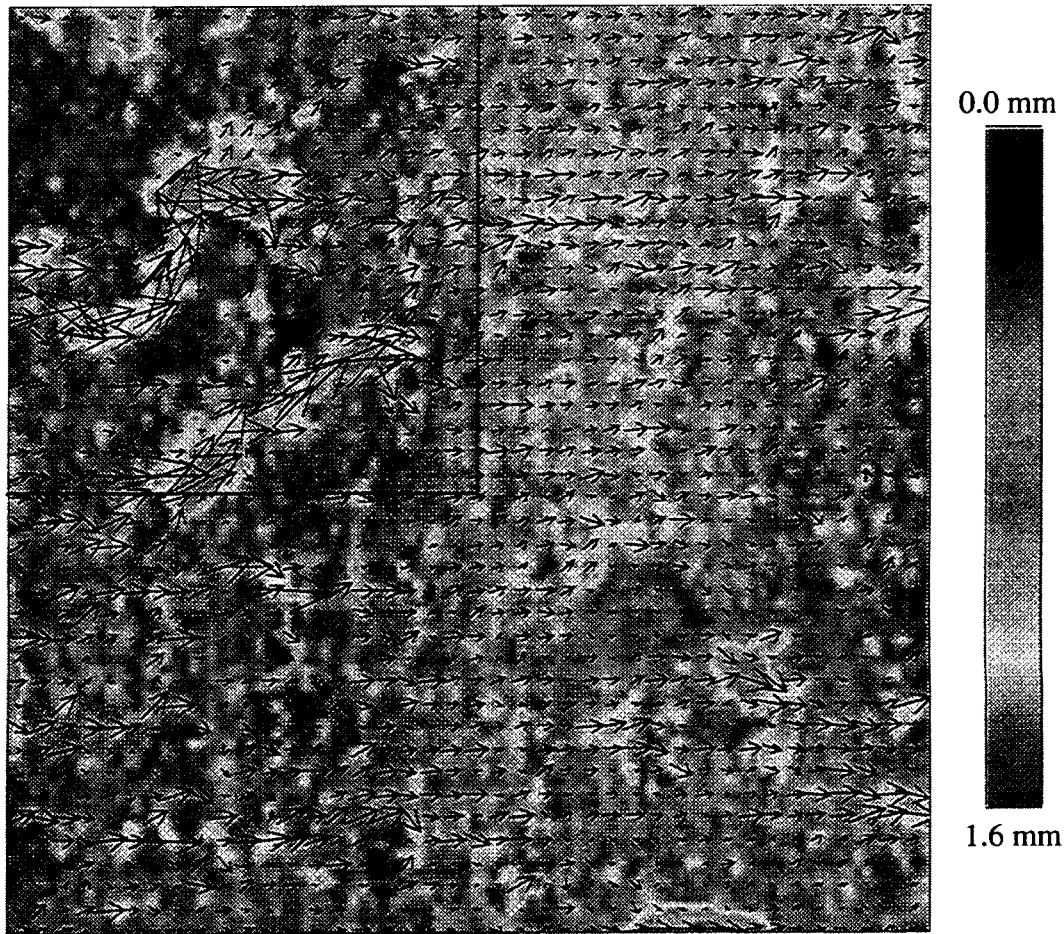


Figure 5-22. Flux field superimposed on the corresponding aperture field

magnitude variation in flow rate were observed at a given pressure drop. Esaki et al. (1991) indicated that dilatancy increased with increasing shear displacement at all normal stress conditions. They also observed a rather faster increase in normal displacement at the beginning of the shear displacement as our numerical exercise indicates. They also observed one to two orders of magnitude increase in hydraulic conductivity for the first 5 mm of shear displacement. They attributed this increase to the fracture dilatancy. The aperture opening by shear deformation was in the range of 1 to 3 mm (Esaki et al., 1992). It may be noted that at zero horizontal displacement (i.e., fully matched condition), the equivalent permeabilities in the x- and y-directions were essentially identical, suggesting isotropicity in the aperture field. As dilation occurred due to the displacement, the permeability increased in a nonlinear fashion, with the y-directional permeability rising more rapidly than the x-directional permeability. After about 1.5-mm displacements the effective permeability appears to increase more rapidly with the x- and y-directional permeabilities diverging even further. While this two-tier increase in permeability tracks the dilation curve rather closely, the permeability curves may be indicating development of anisotropy with a larger displacement. The two-tier increase may also be indicative of two distinct scales of heterogeneity inherent in the fracture faces. A 13-fold increase in the equivalent fracture conductivity has been observed as a result of the 2.4-mm numerical shear displacement. It may be recalled that a 350-percent change in permeability was

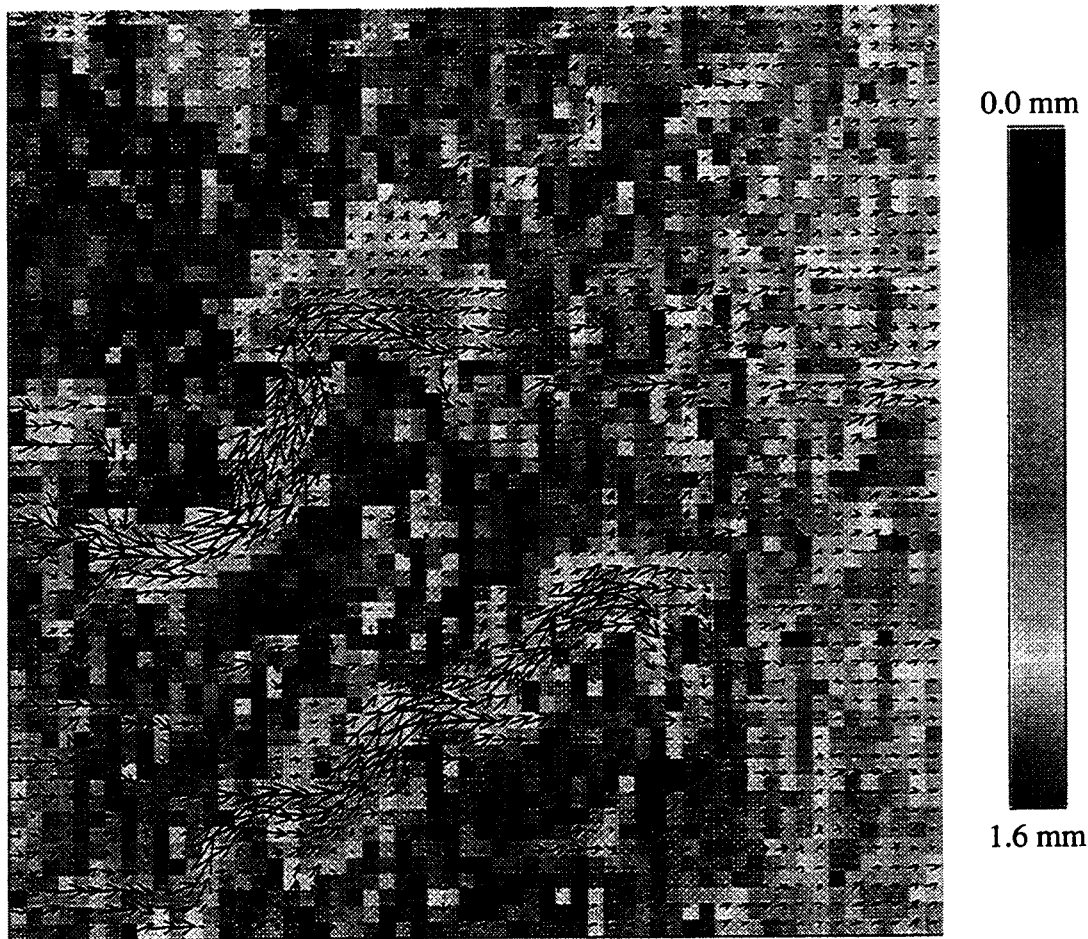


Figure 5-23. Zoomed portion of the flux field from Figure 5-22 to highlight channeling effect conforming to the pattern of heterogeneity in the aperture field.

observed during a four-cycle shear displacement of 0.75 in. (19.05 mm) under normal loads up to 5 MPa. It appears that the increase in permeability due to dilation will offset the permeability reduction effect of the gouge production.

Thompson and Brown (1991), using numerically generated fracture surfaces, calculated effective hydraulic aperture by adjusting the degree to which the two fracture surfaces are matched in order to change the correlation length of the resulting aperture distribution. They concluded that, while two well-matched surfaces are characterized by five to eight channels across the width of the fracture, only one or two channels occurred in fractures with poorly matched surfaces. Poorly matched fractures with transverse and isotropic roughness exhibit a lower flow rate than the well-matched fractures. On the other hand, if the fracture has longitudinal roughness, then a higher flow rate was obtained due to mismatch. For surface roughness correlation lengths less than half the length of the fracture, fracture hydraulic properties are almost independent of the correlation length (Tsang and Tsang, 1987; Thompson and Brown, 1991). For the mismatched surfaces, whose correlation lengths are comparable to the fracture length, the flow rate represents properties of a single channel. This single channel in a poorly matched fracture shows higher flow rates than the well-matched fractures with several channels. Overall, the above study suggests that direction characteristics of the fracture surfaces strongly influences microscopic fluid flow and solute

transport. If the hydraulic gradient aligns with the direction of the trough on the fracture surface, then the solute transport rate will be higher as a result of the higher flow capacity of these channels.

Transverse and isotropic surface roughness on the fracture will strongly influence tracer transport because the tortuous flow path gives rise to a strong transverse dispersion. In this case, the velocity obtained from the breakthrough curve is smaller than the mean fluid velocity. When the surfaces have longitudinal roughness parallel to the pressure gradient, longitudinal dispersion and diffusion contribute to the velocity of the tracer exceeding the mean fluid velocity. If such behavior is not taken into account, then the prediction of solute transport from hydraulic conductivity tests may be in error.

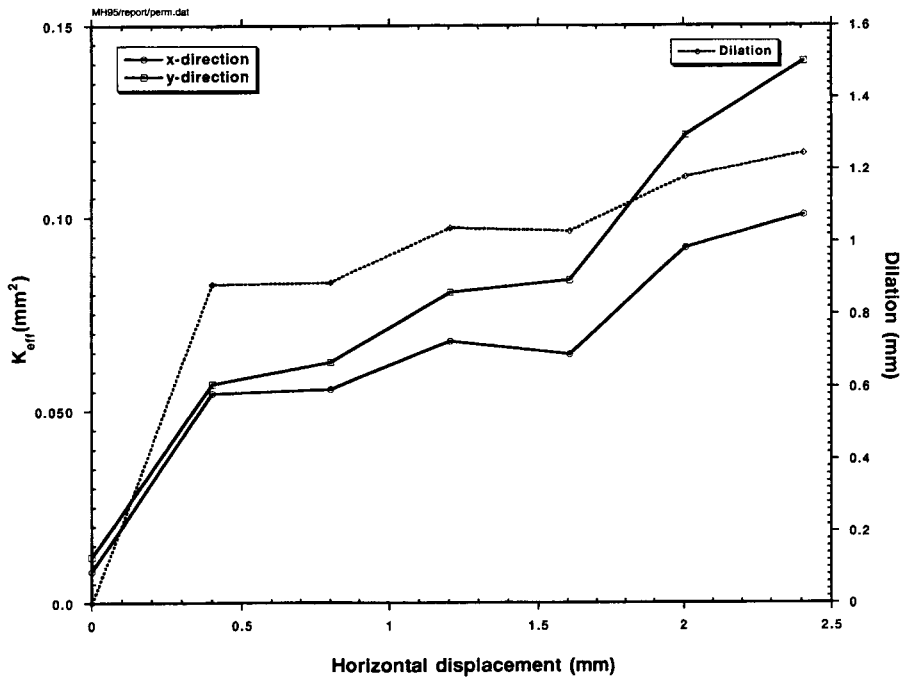


Figure 5-24. Effect of artificial joint dilation on the fracture permeability at various shear displacement under negligible normal-stress condition. The opposite axis represents the minimum dilation.

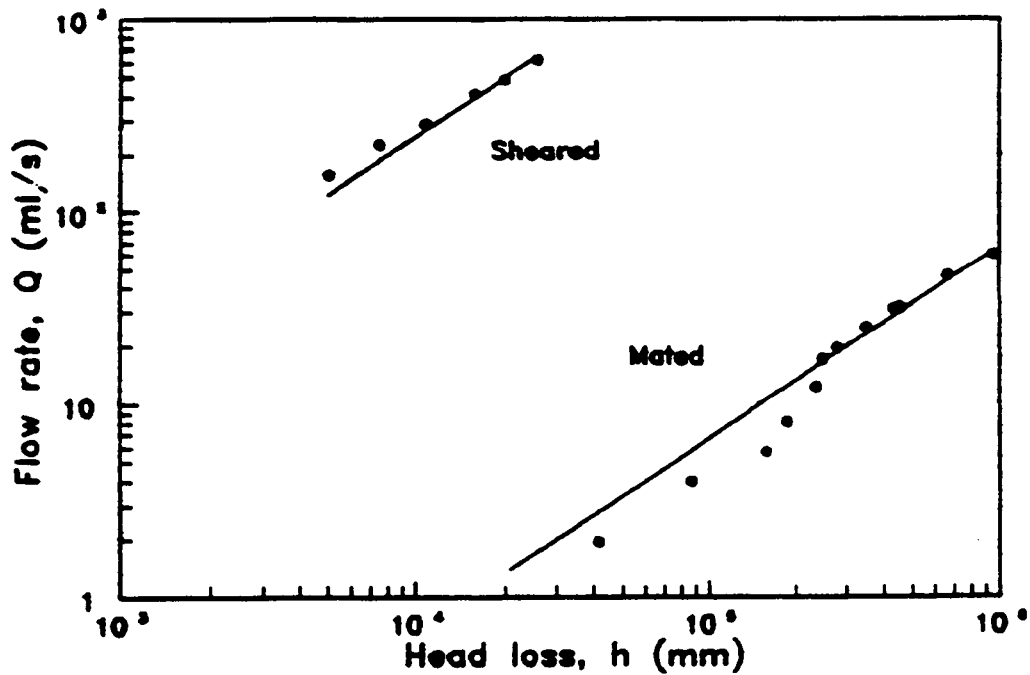


Figure 5-25. Flow rates presented as a function of head losses in a fully matched (mated) condition and at a specified shear under negligible normal load (Piggott et al., 1990)

6 SUMMARY

This report presents the progress made during FY95 on laboratory experimental activities relevant to coupled TMH processes research at the CNWRA. The current activities focus only on the MH part of the coupled TMH processes research with emphasis on fluid flow through rock fractures. The objective of the MH experiments is to understand the key parameters affecting the stress-dependent fracture flow and to provide a database that can be used to evaluate current capabilities for calculating such fracture flow. In FY94, limited experiments were conducted, to study the effects of normal and shear loads on the fracture flow, using a single-jointed ALT specimen. In conducting these experiments, needs have been identified to modify the MH experiment apparatus as well as to conduct some basic laboratory and numerical experimentation studies that will enhance the design of the MH experiments. The FY95 accomplishments include modification of MH experiment apparatus, experimental determination of fracture volume and fracture absolute permeability, numerical determination of fracture aperture from fracture profile data, the effect of disturbing the rock joint from its naturally occurring conditions on the fracture permeability, and focused literature review on fracture flow.

A focused literature review has been conducted on single- and multiphase fluid flow in single fractures under stressed and nonstressed conditions which provided a state-of-the-art information on fracture flow. This information will be useful for design of fracture flow experiments.

The apparatus for conducting MH experiments with emphasis on fracture flow has been modified to address the deficiencies identified in FY94 and reported by Mohanty et al. (1994). This modified apparatus along with the techniques developed in auxiliary experiments for the determination of fracture volume, fracture absolute permeability, and fracture aperture from profile data is suitable for conducting saturated/unsaturated fracture flow experiments under normal and shear loads.

One of the auxiliary experiments involved a feasibility and method establishment study for measuring unsaturated hydraulic conductivity. This required the determination of fracture volume which will be used in the future in the saturation versus relative permeability relationship. Pycnometer method was used in this experiment for determining fracture volume. This method is expected to be readily implementable in the MH experimental apparatus. The average of six fracture volume measurements taken by using pycnometer method was determined to be $5.01 \times 10^{-4} \text{ m}^3$. This corresponded to an average aperture of $1.2 \times 10^{-3} \text{ m}$. Gas fracture permeability was found to be three to four times greater than the liquid permeability. No correction was done to account for gas slippage. The fracture permeability from the flow experiment values were found to be nearly a hundred times smaller than the permeability estimated using the arithmetic mean fracture aperture obtained from the pycnometer method. The results from the pycnometer method will be verified in the future against the cumulative aperture volume from the aperture distribution obtained by using surface profilometry approach.

The second experiment involved studying the effect of disturbing the rock joint from its naturally occurring condition. A specimen was carefully collected from a larger field sample. Tests were conducted to verify the effect of disturbing a rock joint obtained from the field. The test particularly addressed the effect of physically splitting a joint in which two surfaces were held together either by cementitious materials or by a very small contact and into which the fracture has not propagated. Fracture permeabilities were measured before and after splitting the fracture. One order of magnitude increase in permeability was observed after splitting the specimen. The debris formed due to the splitting of the specimen might be clogging the flow path because when the confining pressure is released, the debris are likely to move

under the pressure gradient and get captured in the fracture toward the downstream of the flow. No definitive effect of confining pressure on the fracture permeability was observed at low confining pressures at which the experiments were conducted.

Fracture profile data were collected using a noncontacting surface profilometer. A procedure was developed to calculate fracture aperture from the measured fracture profile. It appears that, in spite of the strong heterogeneity (anisotropy, scale effects, etc.), the corresponding aperture distribution does not display such strong heterogeneity. Although the aperture configuration carries a signature of the surface heterogeneity, it shows geometric isotropy and reduced scale effect. However, further studies are needed using more specimens of different sizes. The aperture distribution measurements of an ALT specimen with induced fracture showed approximately lognormal distribution of the aperture. A mean aperture value of 0.21 mm was observed and a standard deviation of 0.14 mm was observed. A maximum aperture value of 1.59 mm and a minimum aperture of 0 mm were observed. A semivariogram plot for the aperture configuration revealed an isotropic correlation length of about one sixth of the system length. It should be kept in mind that the joint specimen collected from the field may show a different geometric description compared to a freshly induced fracture. Fracture specimens collected from the field as well as fresh fractures most often show weak spots on the fracture faces from rock materials that easily chip off. Some of the large apertures in the aperture distribution may correspond to a few such areas from where rock may have chipped off. If it is present in a larger proportion, then scaling of fracture properties may be difficult and perhaps misleading.

It was observed that the maximum change in the largest aperture value took place at the first numerical displacement step (2.3 times the initial largest aperture value) and then the change rapidly slowed down. The largest aperture width was observed to be 5.2 mm. With a final mean aperture value of 1.8 mm, the change in mean aperture value at the corresponding displacement was observed to be 7.6 times that of the original mean aperture. Similarly, with a standard deviation of 0.524 mm, the change with respect to the matched condition was found to be 2.55 times. This numerical exercise also indicates that, under shear displacement, the aperture distribution deviates from log-normal and tends to be more gaussian. At larger shear displacements, a shift from unimodal to bimodal aperture distribution may take place. While the aperture distribution in a matched condition appears to be isotropic, the displacement tends to develop large aperture streaks that may potentially contribute to the growth of an anisotropic flow path, such as flow channels. The position of these streaks appears to correspond to the anisotropy in the fracture surface height data.

Fracture permeabilities have been obtained at various numerical shear displacements. At zero horizontal displacement (i.e. fully matched condition) the equivalent permeabilities in the x- and y-directions were essentially identical, suggesting isotropicity in the aperture field. As dilation occurred due to the displacement, the permeability increased in a nonlinear fashion, with y-directional permeability rising more rapidly than the x-directional permeability. After about 1.5-mm displacement, the effective permeability appears to increase more rapidly with x- and y-directional permeabilities diverging even further. While this two-tier increase in permeability tracks the dilation curve rather closely, the permeability curves may be indicating development of anisotropy with larger displacement. The two-tier increase may also confirm the two distinct scales of heterogeneity inferred from the aperture distribution data. A 13-fold increase in the equivalent fracture conductivity has been observed as a result of 2.4-mm numerical shear displacement.

7 REFERENCES

- Abelin, H., L. Bergersson, J. Gidlund, L. Moreno, I. Neretnieks, H. Widen, and T. Agren. 1987. *3-D Migration Experiment—Report 3 Part I, Performed Experiments, Results and Evaluation*. Stripa Project Technical Report 87-21. Stockholm, Sweden: Swedish Nuclear Fuel and Waste Management Company (SKB).
- Ahola, M.P., S.M. Hsiung, L.J. Lorig, and A.H. Chowdhury. 1992. *Thermo-Hydro-Mechanical Coupled Modeling: Multiple Fracture Model BMT2; Coupled Stress-Flow Model, TC1. DECOVALEX—Phase I*. CNWRA 92-005. San Antonio, TX: Center for Nuclear Waste Regulatory Analyses.
- Ahola, M.P., S.M. Hsiung, L.J. Lorig, and A.H. Chowdhury. 1993. *Thermo-Hydro-Mechanical Coupled Modeling: Multiple Fracture Model BMT3; Coupled Stress-Flow Model, TC1. DECOVALEX—Phase II*. CNWRA 93-002. San Antonio, TX: Center for Nuclear Waste Regulatory Analyses.
- Ahola, M.P., G.I. Ofoegbu, A.H. Chowdhury, and S.M. Hsiung. 1994. *Thermo-Hydro-Mechanical Coupled Modeling: Big-Ben Experiment, TC3. DECOVALEX—Phase III*. CNWRA 94-021. San Antonio, TX: Center for Nuclear Waste Regulatory Analyses.
- Althaus, E., A. Friz-Topfer, C. Lempp, and O. Hatau. 1994. Effects of water on strength and failure mode of coarse-grained granites at 300 °C. *Rock Mechanics and Rock Engineering* 27: 1–21.
- Amadei, B., J.F. Carrier, and T. Illangasekare. 1995. Effect of turbulence on fracture flow and advective transport of solute. *International Journal of Rock Mechanics and Mining Sciences & Geomechanics Abstracts* 32(4): 343–356.
- Amyx, J.W., D.N. Bass, and R.L. Whiting. 1960. *Petroleum Reservoir Engineering*. New York, NY: McGraw-Hill Book Company.
- Baker, W.J. 1955. Flow in fissured formations. *Proceedings of Fourth Petroleum Congress, Rome*: 2: 379–293.
- Bandis, S.C., A.C. Lumsden, and N.R. Barton. 1981. Experiment studies of scale effect on the shear behavior of rock joints. *International Journal of Rock Mechanics and Mining Sciences & Geomechanics Abstracts* 18: 1–20.
- Bandis, S.C., A.C. Lumsden, and N.R. Barton. 1983. Fundamentals of rock joint deformation. *International Journal of Rock Mechanics and Mining Sciences & Geomechanics Abstracts* 20: 249–268.
- Barton, N., S. Bandis, and K. Bakhtar. 1985. Strength, deformation and conductivity coupling of rock joints. *International Journal of Rock Mechanics and Mining Sciences & Geomechanics Abstracts* 22(3): 121–140.
- Barton, N.R. 1986. Deformation phenomena in jointed rock. *Geotechnique* 36(2): 147–167.

- Bassett, R.L., S.P. Neumann, T.C. Rasmussen, A. Guzman, G.R. Davidson, and C.F. Lohrstorfer. 1994. *Validation Studies for Assessing Unsaturated Flow and Transport through Fractured Rock*. NUREG/CR-6203. Washington, DC: Nuclear Regulatory Commission.
- Bernaix, J. 1967. *Étude géotechnique de la roche de Malpasset*. Paris, France. Dunod: 215.
- Bernaix, J. 1969. New laboratory methods of studying the mechanical properties of rock. *International Journal of Rock Mechanics and Mining Sciences & Geomechanics Abstracts* 6: 43–90.
- Blair, S.C. 1994. Overview and status of coupled THMC processes: Geomechanics. *NRC-DOE Technical Exchange on Couple TMHC Processes*. Las Vegas, NV.
- Blandpied, M.L. T.E. Tullis, and J.D. Weeks. 1987. Frictional behavior of granite at low and high sliding velocities. *Geophysical Research Letter* 14: 554–557.
- Brower, R.R., and N.R. Morrow. 1985. Fluid flow in cracks as related to low-permeability gas sands. *Society of Petroleum Engineers Journal*, 25: 191–201.
- Brown, D.M. 1984. *Stochastic Analysis of Flow and Solute Transport in a Variable-Aperture Rock Fracture*. M.S. Thesis. Cambridge, MS: Massachusetts Institute of Technology.
- Brown, S.R., and C.H. Scholtz. 1985. Broad bandwidth study of the topography of natural rock surfaces. *Journal of Geophysical Research* 90: 575–582.
- Brown, S.R., and C.H. Scholtz. 1986. Closure of rock joint. *Journal of Geophysical Research* 91: 4,939–4,948.
- Brown, S.R. 1987. Fluid flow through rock joints: The effect of surface roughness. *Journal of Geophysical Research*. 92: 1,337–1,347.
- Buscheck, T.A., and J.J. Nitao. 1993. The analysis of repository-heat-driven hydrothermal flow at Yucca Mountain. *Proceedings of the Fourth International Conference on High Level Radioactive Waste Management*. La Grange Park, IL: American Nuclear Society: 847–867.
- Carr, J.R. and J.B. Warriner. 1989. Relationship between fractal dimension and joint roughness coefficient. *Bulletin of the Association of Engineering Geologists* 26: 253–263.
- Case, J.B, and P.C. Kelsall. 1987. Coupled processes in repository sealing. *Coupled Processes Associated with Nuclear Waste Repository*. C.F. Tsang, ed. Orlando, FL: Academic Press, Inc.: 43: 591.
- Chan, T., and B.W. Nakka. 1995. A two-dimensional analytical well model with application to geosphere flow modeling. *AECL-10880/COG-93-215*. Atomic Energy of Canada Limited.
- Christensen, R.J., S.R. Swanson, and W.S. Brown. 1974. Torsional shear measurements of the frictional properties of westerly granite. *Proceedings of the Third Congress of the International Society for Rock Mechanics*: 221–225.

- Chuang, Y., W.R. Haldeman, T.C. Rasmussen, and D.D. Evans. 1990. *Laboratory Analysis of Fluid Flow and Solute Transport Through a Variably Saturated Fracture Embedded in Porous Tuff*. NUREG/CR-5482. Washington, DC: Nuclear Regulatory Commission.
- Danielson, R.E., and P.L. Southerland. 1986. Porosity. *Methods of Soil Analysis Part 1—Physical and Mineralogical Methods*. A. Klute, ed. Madison, WI: Soil Science Society of America, Inc: 443–461.
- Darcy, H. 1856. *Les Fontaines Publique de la Ville de Digon*. Paris, France.
- de Marsily, G. 1987. An overview of coupled processes with emphasis on geohydrology. *Coupled Processes Associated with Nuclear Waste Repositories*. C.F. Tsang, ed. San Diego, CA: Academic Press: 23–27.
- Elsworth, D., and R.E. Goodman. 1986. Characterization of rock fissure hydraulic conductivity using idealized wall roughness profiles. *International Rock Mechanics and Mining Science and Geomechanics Abstracts* 23: 233–243.
- Engelder, T., and C.H. Scholtz. 1981. Fluid flow along very smooth joints at effective pressure up to 200 megapascals. *Mechanical Behavior of Crustal Rocks*. *American Geophysical Union Mono.* No. 24: 147–152.
- Esaki, T., H. Hojo, T. Kimura, and N. Kameda. 1991. Shear-flow coupling test on rock joints. *Proceedings of the 7th International Congress on Rock Mechanics*. W. Wittke (ed.) Aachen, Deutschland: 1: 389–392.
- Esaki, T., K. Ikusada, A. Aikawa, and T. Kimura. 1992. Surface roughness and hydraulic properties of sheared rock. *Conference of Fractured and Jointed Rock Masses. Preprints*. Lake Tahoe, CA: Lawrence Berkeley Laboratory.
- Foltz, S.D., V.C. Tidwell, R.J. Glass, and S.R. Sobolik. 1993. Investigation of fracture-matrix interaction: Preliminary experiments in simple system. *Proceedings of the Fourth International Conference on High Level Radioactive Waste Management*. La Grange Park, IL: American Nuclear Society: 328–335.
- Freeze, R.A., and J.A. Cherry. 1979. *Groudwater*. Englewood Cliffs, NJ: Prentice Hall.
- Gale, J.E. 1975. *A Numerical Field and Laboratory Study of Flow in Rocks with Deformable Fractures*. Ph.D Thesis. Berkeley, CA: University of California.
- Gale, J.E., and K.G. Raven. 1980. *Effect of Sample Size on Stress-Permeability Relationships for Natural Fractures*. Technical Information Report No. 48, LBL-11865, SAC-48, UC-70. Berkeley, CA: Lawrence Berkeley Laboratory.
- Gale, J.E. 1982. The effects of fracture type (induced versus natural) on the stress, fracture-closure, fracture-permeability relationships. *Proceedings of the 23rd U.S. Rock Mechanics Symposium*. Berkeley, CA: University of California: 290–298.

- Gale, J.E. 1984. Changes in fracture permeability as a function of sample size, fracture type, and stress history. *Proceedings of the International Symposium on Groundwater Utilization and Contaminant Hydrogeology*. Montreal, Quebec: International Association of Hydrology: 259.
- Gale, J.E. 1987. Comparison of coupled fracture deformation and fluid flow models with direct measurements of fracture pore structure and stress-flow properties. *Proceedings of the 28th US Symposium on Rock Mechanics*. Tucson, AZ: University of Arizona: 1,213–1,222.
- Gale, J.E., A. Rouleu, and L.C. Atkinson. 1985. Hydraulic properties of fractures. *Memoires Volume XVII Part 1 Proceedings on Hydrogeology of Rocks of Low Permeability*. Tuscon, AZ: International Association of Hydrogeologists: 1–15.
- Gallegos, D.P., S.G. Thoma, and D.M. Smith. 1992. Impact of fracture coatings on the transfer of water across fracture faces in unsaturated media. *Proceedings of the Third Annual International High-Level Radioactive Waste Management Conference*. LaGrange Park, IL: American Nuclear Society: 738–745.
- Gangi, A.F. 1978. Variation of whole and fractured porous rock permeability with confining pressure. *International Journal of Rock Mechanics and Mining Sciences & Geomechanics Abstracts* 15: 249–257.
- Gilling, D., N.L. Jefferies, P. Fowles, M.R. Hawkesworth, and D.J. Parker. 1991. The application of position emission tomography to the study of mass transfer in fractured rock. *Nirex Report NSS/R241*. Harwell, Oxfordshire, UK: UK Nirex Ltd.
- Glass, R.J., and D.L. Norton. 1992. Wetted-region structure in horizontal unsaturated fractures: Water entry through the surrounding porous matrix. *Proceedings of the Third Annual International High-Level Radioactive Waste Management Conference*. LaGrange Park, IL: American Nuclear Society: 321–331.
- Goodman, R.E. 1976. *Method of Geological Engineering in Discontinuous Rocks*. St. Paul, MN: West Publishing Co.
- Green, R.T., F.T. Dodge, S.J. Svedeman, R.D. Manteufel, G. Rice, K.A. Meyer, and R.G. Baca. 1995. *Thermally Driven Moisture Redistribution in Partially Saturated Porous Media*. CNWRA 95-005. San Antonio, TX: Center for Nuclear Waste Regulatory Analyses.
- Gureghian, A.B., C.J. Noronha, and T.T. Vandergraaf. 1990. *Large Block Migration Experiments INTRAVAL Phase I, Test Case 9*. Report #BMI/OWTD-7. Prepared by Office of Waste Technology Development and Atomic Energy of Canada Limited for Office of Waste Technology Development. Willowbrook, IL: Battelle.
- Gustaffson, E., and C.E. Klockars. 1982. Studies of groundwater transport in fractured crystalline rock under controlled conditions using non-radioactive tracers. *KBS-Technical Report 81-07*. Stockholm, Sweden: Svensk Kärnbränslehanterings AB.

- Hill, D.P., et al. 1993. Seismicity remotely triggered by the magnitude 6.3 Landers, California earthquake. *Science* 260: 1,617–1,623.
- Hsiung, S.M., W. Blake, A.H. Chowdhury, and M.P. Ahola. 1992a. *Field Site Investigation: Effect of Mine Seismicity on a Jointed Rock Mass*. CNWRA 92-012. San Antonio, TX: Center for Nuclear Waste Regulatory Analyses.
- Hsiung, S.M., W. Blake, A.H. Chowdhury, and T.J. Williams. 1992b. Effects of mining-induced seismic events on a deep underground mine. *PAGEOPH* 139(3/4): 741–762.
- Hsiung, S.M., D.D. Kana, M.P. Ahola, A.H. Chowdhury, and A. Ghosh. 1994. *Laboratory Characterization of Rock Joints*. NUREG/CR-6178. Washington, DC: Nuclear Regulatory Commission.
- Huitt, J.L. 1956. Fluid flow in simulated fractures. *AICHE Journal* 2: 259.
- Hull, L.C., J.D. Miller, and T.M. Clemo. 1987. Laboratory and simulation studies of solute transport in fracture networks. *Water Resources Research* 23(8): 1,505–1,513.
- Iwai, K. 1976. *Fundamental Studies of Fluid Flow Through a Single Fracture*. Ph.D. Thesis. Berkeley, CA: University of California.
- Johnson, B. 1983. Permeability of a simulated fracture as a function of normal stress. *Proceedings of the 24th U.S. Symposium on Rock Mechanics*. College Station, TX: Texas A&M University: 519–523.
- Jones, F.O. 1975. A laboratory study of the effects of confining pressure on fracture flow and storage capacity in carbonate rocks. *Journal of Petroleum Technology*: 21–27.
- Jouanna, P. 1972. *Effet des Sollicitations Mécaniques sur les Écoulements dans Certains Milieux Fissurés*. Thèse, Docteur ES-Sciences Physiques. France: Université de Toulouse.
- Kana, D.D., D.C. Scheidt, B.H.G. Brady, A.H. Chowdhury, S.M. Hsiung, and B.W. Vanzant. 1990. *Development of a Rock-Joint Dynamic Shear Test Apparatus*. CNWRA 90-005. San Antonio, TX: Center for Nuclear Waste Regulatory Analyses.
- Kana, D.D., B.H.G. Brady, B.W. Vanzant, and P.K. Nair. 1991. *Critical Assessment of Seismic and Geomechanics Literature Related to a High-Level Nuclear Waste Underground Repository*. NUREG/CR-5440. Washington, DC: Nuclear Regulatory Commission.
- Kana, D.D., D.J. Fox, S.M. Hsiung, and A.H. Chowdhury. 1995. *An Experimental Model Study of Seismic Response of an Underground Opening in Jointed Rock*. CNWRA 95-012. San Antonio, TX: Center for Nuclear Waste Regulatory Analyses.
- Keller, A.A., P.V. Roberts, and P.K. Kitanidis. 1995. Prediction of single phase transport parameters in a variable aperture fracture. *Geophysical Research Letters* 22(11): 1,425–1,428.

- Klavetter, E.A., and R.R. Peters. 1986. *Estimation of Hydrologic Properties of an Unsaturated Fracture Rock Mass*. SAND84-2642. Albuquerque, NM: Sandia National Laboratories.
- Kranz, R.L., S.D. Frankel, T. Engelder, and C.H. Scholz. 1979. The permeability of whole and jointed Barre granite. *International Journal of Rock Mechanics and Mining Sciences & Geomechanics Abstracts* 16: 225–235.
- Kutter, H.K. 1974. Rotary shear testing of rock joints. *Proceedings for the Third Congress of the International Society for Rock Mechanics*. Washington, DC: National Academy Sciences: 254–262.
- Kwicklis, E.M., F. Thamir, R.W. Healy, C.J. Boughton, and S. Anderson. 1991. *Numerical and Laboratory Investigations of Transient and Steady-State Flow in a Fractured Core*. NUREG/CP-0040. Washington, DC: Nuclear Regulatory Commission: 101–108.
- Lai, C.S. 1971. *Fluid Flow Through Rock Salt Under Various Stress States*. Ph.D. Dissertation. East Lansing, MI: Michigan State University.
- Lamb, H. 1932. *Hydrodynamics*. 6th ed. New York, NY: Dover Publications.
- Lin, W.A., and W.D. Daily. 1989. Laboratory study of fracture healing in Topopah Spring tuff—implications for near field hydrology. *Nuclear Waste Isolation in Unsaturated Zone Focus '89 Proceedings*. La Grange Park, IL: American Nuclear Society: 443–449.
- Lomize, G.M. 1951. *Flow in Fractured Rocks*. Moscow, Russia: All-Union Energetics Publishers: 7–127.
- Louis, C. 1969. A study of groundwater flow in jointed rock and its influence on the stability of rock masses. *Rock Mechanics Research Report No. 10*. London, England: Imperial College.
- Louis, C. 1974. Introduction. *Hydraulique des Roches*. Orlèans, France: Bureau de Recherches Géologiques et Minières.
- Maini, Y.N.T. 1971. *In situ Hydraulic Parameters in Jointed Rock—Their Measurement and Interpretation*. Ph.D. Thesis. London, England: Imperial College.
- Maini, T., and G. Hocking. 1977. An examination of the feasibility of hydrologic isolation of a high level repository in crystalline rock. *Geologic Disposal of High-Level Radioactive Waste Session, Annual Meeting of the Geologic Society of America*. Seattle, WA: Geologic Society of America: 99–106.
- Makurat, A., and N. Barton. 1985. Shear-flow coupling in non-planar rock joints. *Proceedings of the International Symposium on Coupled Processes Affecting the Performance of Nuclear Waste Repository*. Berkeley, CA: Lawrence Berkeley Laboratory: 225–258.
- Makurat, A., N. Barton, N.S. Rad, and S. Bandis. 1990. Joint conductivity variation due to normal and shear deformation. *Rock Joints*. N. Barton and O. Stephansson, ed. A.A. Balkema: Rotterdam, The Netherlands: 535–540.

- Manteufel, R.D., M.P. Ahola, D.R. Turner, and A.H. Chowdhury. 1993. *A Literature Review of Coupled Thermal-Hydrologic-Mechanical-Chemical Processes Pertinent to the Proposed High-Level Nuclear Waste Repository at Yucca Mountain*. NUREG/CR-6021, CNWRA 92-011. Washington, DC: Nuclear Regulatory Commission.
- McWilliams, P.C., S.M. Miller, and J.C. Kerkering. 1990. Fractal characterization of rock fracture roughness for estimating shear strength. *Mechanics of Jointed and Faulted Rock*. H.P. Rossmanith, ed. A.A. Balkema: Rotterdam, The Netherlands: 331-338.
- Moench. A.F. 1984. Double-porosity models for a fissured groundwater reservoir with fracture skin. *Water Resources Research* 20: 834-846.
- Mohanty, S., A.H. Chowdhury, S.M. Hsiung, and M.P. Ahola. 1994. *Single Fracture Flow Behavior of Apache Leap Tuff Under Normal and Shear Loads*. CNWRA 94-024. San Antonio, TX: Center for Nuclear Waste Regulatory Analyses.
- Mohanty, S., R.D. Manteufel, A.H. Chowdhury, and J. Philip. 1995. Fracture permeability under effect of normal and shear stress: A preliminary experimental investigation. *Proceedings of the Sixth International Conference on High-Level Radioactive Waste Management*. LaGrange Park, IL: American Nuclear Society: 41-43.
- Moreno, L., Y.W. Tsang, C.F. Tsang, F. Hale, and I. Neretnieks. 1988. Flow and tracer transport in a single fracture. A stochastic model and its relation to some field observations. *Water Resource Research* 24 (12): 2,033-2,048.
- Moreno, L., and C. Tsang. 1994. Flow channeling in strongly heterogeneous porous media: A numerical study. *Water Resources Research* 30(5): 1,421-1,430.
- Myers, N.O. 1962. Characterization of surface roughness. *Wear* 5: 182-189.
- Nelson, R.A., and J. Handin. 1977. Experimental study of fracture permeability in porous rock. *The American Association of Petroleum Geologists Bulletin* 61(2): 227-236.
- Neretnieks, I. 1985. Transport in fractured rocks. *Memoires of International Association of Hydrogeologists*. XVII(2): 301-318.
- Neretnieks, I. 1987a. Some coupled processes which may be important for a nuclear waste repository. *Coupled Processes Associated with Nuclear Waste Repository*. C.F. Tsang, ed. Orlando, FL: Academic Press, Inc.: 759-763.
- Neretnieks, I. 1987b. Channeling effects in flow and transport in fractured rocks—Some recent observations and models. *Proceedings of GEOVAL-87 Symposium*. Stockholm, Sweden: Swedish Nuclear Power Inspectorate.

- Neretnieks, I., H. Abelin, and L. Birgersson. 1987. Some recent observations of channeling in fractured rocks—its potential impact on radionuclide migration. *Proceedings of the Conference on Geostatistical, Sensitivity, and Uncertainty Methods for Ground-Water Flow and Radionuclide Transport Modeling*. Columbus, OH: Battelle Press: 387–410.
- Neuzil, C.E., and J.V. Tracy. 1981. Flow through fractures. *Water Resources Research* 17(7): 191–199.
- Ofoegbu, G.I., S.M. Hsiung, A.H. Chowdhury, and J. Philip. 1995. *Field Site Investigation: Effect of Mine Seismicity on Groundwater Hydrology*. NUREG/CR-6283. Washington, DC: Nuclear Regulatory Commission.
- Ohnishi, Y. 1973. *Laboratory Measurement of Induced Water Pressures in Jointed Rocks*. Ph.D. Thesis. Berkely, CA: University of California.
- Olsson, W.A. 1987. *Rock Joint Compliance Studies*. SAND86-0177. Albuquerque, NM: Sandia National Laboratories.
- Page, J.B. 1948. Advantages of the pressure pycnometer for measuring the pore space in soils. *Proceedings—Soil Science Society of America* 12: 81–84.
- Parrish, D.R. 1963. Fluid flow in rough fractures. *Proceedings of the Society of Petroleum Engineers of the American Institute of Mining, Metallurgical, and Petroleum Engineers. Production Research Symposium*. Norman, OK: Paper No. SPE 563: 9.
- Persoff, P., K. Pruess, and L. Myer. 1991. Two-phase flow visualization and relative permeability measurement in transparent replicas of rough-walled rock fractures. *Proceedings—Sixteenth Workshop on Geothermal Reservoir Engineering*. SGP-TR-134. Stanford, CA: Stanford University.
- Piggott, A.R., and D. Elsworth. 1990. Laboratory studies of transport within a single rock fracture. *Rock Joints*. N. Barton and O. Stephansson, eds. Rotterdam, The Netherlands: A.A. Balkema: 397–404.
- Pratt, H.R., H.S. Swolfs, and A.D. Black. 1974. *Properties of In Situ Jointed Rock*. Final Technical Report No. TR54-57. Salt Lake City, UT: Terra-Tek.
- Price, R.H., S.R. Brown, W.A. Olsson. 1994. Laboratory determination of the mechanical properties of fractures. Study Plan 8.3.1.15.1.4 RO. Albuquerque, NM: Sandia National Laboratory.
- Priest, S.D. 1993. *Discontinuity Analysis for Rock Engineering*. New York, NY: Chapman and Hall.
- Pruess, K., and Y.W. Tsang. 1990. On two-phase relative permeability and capillary pressure of rough-walled rock fractures. *Water Resources Research* 26(9): 1,915–1,926.
- Pyrak-Nolte, L.J., L.R. Myer, N.G.W. Cook, and P.A. Witherspoon. 1987. Hydraulic and mechanical properties of natural fractures in low permeability rock. *Proceedings of Sixth International Congress on Rock Mechanics*. Rotterdam, The Netherlands: A.A. Balkema.

- Rasmussen, T.C. 1992. Bypass flow through unsaturated fractured rock: Effective models for fracture-matrix interactions. *AGU 1992 Fall Meeting Abstract Supplement*. H32A-11. San Francisco, CA: American Geophysical Union.
- Rasmussen, T.C. 1995. Laboratory characterization of fluid flow parameters in a porous rock containing a discrete fracture. *Geophysical Research Letters* 22(11): 1,401-1,404.
- Reda, D.C., and R. G. Hadley. 1985. Saturated permeability measurements on pumice and welded-tuffaceous materials. *Hydrogeology of Rocks of Low Permeability*. Memoires, International Congress. International Association of Hydrologists 17: 87-98.
- Rissler, P. 1978. Determination of the water permeability of jointed rock. English edition of Volume 5. *Institute for Foundation Engineering Mechanics, Rock Mechanics and Water Ways Construction*. Aachen, Republic of Germany: RWTH University.
- Romm, E.S. 1966. *Flow Characteristics of Fractured Rocks*. Russian edition. Moscow, Russia: Nedra: 283.
- Russell, M.B. 1950. A simplified air-pycnometer for field use. *Proceedings of the Soil Science Society of America*: Madison, WI: Soil Science Society of America 14: 73-76.
- Russo, A.J., and D.C. Reda. 1989. Drying of and initially saturated fractured volcanic tuff. *Journal of Fluids Engineering* 3: 191-196.
- Schrauf, T.W., and D.D. Evans. 1984. *Relationship Between the Gas Conductivity and Geometry of a Natural Fracture*. NUREG/CR-3680. Tucson, AZ: University of Arizona.
- Sharp, J.C. 1970. *Fluid Flow Through Fissured Media*. Ph.D. Thesis. London, England: University of London: Imperial College of Science and Technology.
- Sharp, J.S., and Y.N.T. Maini. 1972. Fundamental considerations on the hydraulic characteristics of joints in rock. *Proceedings of Symposium on Percolation through Fissured Rock*. Stuttgart, Germany: International Society for Rock Mechanics and International Association of Engineering Geology: T1-F 1-15.
- Sharp, J.M., Jr., N.I. Robinson, R.C. Smyth-Boulton, and K.L. Milliken. 1995. Fracture skin effects. *Groundwater Transport*. H.P. Rossmanith, ed. Rotterdam, The Netherlands: Balkema: 449-454.
- Silliman, S.E. 1989. Interpretation of the difference between aperture estimates derived from hydraulic and tracer tests in a single fracture. *Water Resource Research* 15(6): 1,543-1,559.
- Smith, L., C.W. Mase, and F.W. Schwartz. 1987. Estimation of fracture aperture using hydraulic and tracer tests. *28th U.S. Symposium on Rock Mechanics*. Tucson, AZ: University of Arizona. 453-463.

- Smyth-Boulton, R.C., and J.M. Sharp, Jr. 1994. Geological controls on porosity and permeability of the Santan ash-flow tuff. Trans-Pecos Texas: *Geological Society of America Abstract with Programs* 26: A-285.
- Snow, D.T. 1968. Rock fracture spacings, openings, and porosities. *Journal of Soil Mechanics and Foundation Division* 94(1): 73-91.
- Snow, D.T. 1970. The frequency of apertures of fractures in rock. *International Journal of Rock Mechanics and Mining Sciences & Geomechanics Abstracts*. 7: 23-40.
- Somerton, W.H., I.M. Soylemezoglu, and R.D. Dudley. 1975. Effect of stress on permeability of coal. *International Rock Mechanics and Mining Sciences & Geomechanics Abstracts* 12: 5-6.
- Swan, G. 1983. Determination of stiffness and other joint properties from roughness measurements. *Rock Mechanics and Rock Engineering* 18: 19-38.
- Takahashi, M., H. Koide, and X. Zi-qui. 1991. Correlation between permeability and deformational characteristics of the Shirahama sandstone and Inada granite. *Proceedings of the 7th International Congress on Rock Mechanics*. W. Wittke ed. Aachen/Deutschland: 417-420.
- Taufel, L. 1987. Permeability changes during shear deformation of fractured rock. *Proceedings of the 28th Symposium on Rock Mechanics*. Tucson, AZ: University of Arizona. 473-480.
- Thompson, M.E., and S.R. Brown. 1991. The effect of anisotropic surface roughness on flow and transport in fractures. *Journal of Geophysical Research* 96(B13): 21,923-21,932.
- Thorpe, R.K., D.J. Watkins, and W.E. Ralph. 1983. Strength and permeability of an extra-large specimen of granitic rock. *Proceedings of the 24th US Symposium on Rock Mechanics*. College Station, TX: Texas A&M University: 511-518.
- Tsang, Y.W. 1992. Usage of "equivalent aperture" for rock fractures as derived from hydraulic and tracer tests. *Water Resources Research* 28(5): 1,451-1,455.
- Tsang, Y.W., and P.A. Witherspoon. 1981. Hydromechanical behavior of a deformable rock fracture subject to normal stress. *Journal of Geophysical Research* 86(B10): 9,287-9,298.
- Tsang, Y.W., and P.A. Witherspoon. 1983. The dependence of fracture mechanical and fluid flow properties on fracture roughness and sample size. *Journal of Geophysical Research* 88(B3): 2,359-2,366.
- Tsang, Y.W., and P.A. Witherspoon. 1985. Effect of fracture roughness on fluid flow through a single deformable fracture. *Hydrogeology of Rocks of Low Permeability, Memoires/International Association of Hydrogeologists* 17: 683-694.
- Tsang, Y.W., and C.F. Tsang. 1987. Channel model of flow through fractured media. *Water Resources Research* 23(3): 467-479.

- Tse, R., and D.M. Crudden. 1979. Estimating joint roughness coefficients. *International Journal of Rock Mechanics and Mining Sciences & Geomechanics Abstracts* 16: 303–307.
- U.S. Department of Energy. 1988. *Site Characterization Plan: Yucca Mountain Site, Nevada Research and Development Area, Nevada*. Washington, DC: U.S. Department of Energy, Office of Civilian Radioactive Waste Management.
- U.S. Department of Energy. 1994. Yucca Mountain Site Characterization Project Five-Year Plan, Fiscal Years 1996-2000. Predecisional Draft. Washington, DC: DOE.
- Vandergraaf, T.T. 1995. Radionuclide migration experiments under laboratory conditions. *Geophysical Research Letters* 22(11): 1,409–1,412.
- Walsh, J.B. 1981. Effects of pore pressure and confining pressure on fracture permeability. *International Rock Mechanics and Mining Sciences & Geomechanics Abstracts* 18: 429–435.
- Wang, R., and J.M. Kemeny. 1994. A study of the coupling between mechanical loading and flow properties in tuffaceous rock. *Rock Mechanics* Nelson and Laubach, eds. Balkema: Rotterdam, The Netherlands: 749–756.
- Watanabe, K., and Y. Hoshino. 1980. Estimation method of permeability coefficient in the natural open-crack. *Journal of the Japan Society of Engineering Geology* 21(2): 60–70.
- Watanabe, K., and N. Kodajima. 1981. Fundamental study on the theoretical estimation of permeability coefficient of fracture system in rock mass. *Journal of the Japan Society of Engineering Geology* 22(4): 1–7.
- Wilson, C.R., P.A. Witherspoon, J.C.S. Long, R.M. Galbraith, A.O. Dubois, and M.J. McPherson. 1983. Large-scale hydraulic conductivity measurements in fractured granite. *International Journal of Rock Mechanics of Mining Sciences & Geomechanics Abstract*: 20(6): 269–276.
- Witherspoon, P.A., J.S.Y. Wang, K. Iwai, and J.E. Gale. 1980. Validity of cubic law for fluid flow in a deformable rock fracture. *Water Resources Research* 16(6): 1,016–1,024.
- Wu, T.H., and E.M. Ali. 1978. Statistical representation of joint roughness. *International Journal of Rock Mechanics and Mining Science and Geomechanical Abstracts* 15: 259–262.
- Xu, S., and M.H. Frieta. 1988. Use of a rotary shear box for testing the shear strength of rock joints. *Geotechnique* 38(2): 301–309.
- Zimmerman, R.W., and G.S. Bodvarsson. 1994. *Hydraulic Conductivity of Rock Fractures*. Berkeley, CA: University of California.

APPENDIX A
PRESSURE DIFFERENTIAL MEASUREMENTS FOR
FORWARD AND REVERSE LIQUID FLOW EXPERIMENTS

| | Press. Diff. (cm H ₂ O) | Q (ml/sec) |
|---------------------|---------------------------------------|---------------|
| Reverse Flow | 0.333 | 2.612 |
| | 0.417 | 3.463 |
| | 0.500 | 4.101 |
| | 0.583 | 4.952 |
| | 0.667 | 6.016 |
| | 0.750 | 6.867 |
| | 0.833 | 7.931 |
| | 0.917 | 8.994 |
| | 1.000 | 10.058 |
| | 0.000 | 0.000 |
| | 0.017 | 0.060 |
| | 0.033 | 0.272 |
| | 0.050 | 0.485 |
| | 0.067 | 0.591 |
| | 0.083 | 0.698 |
| | 0.167 | 1.230 |
| | 0.250 | 1.761 |
| | 0.333 | 2.612 |
| | 0.417 | 3.251 |
| | 0.500 | 3.889 |
| | 0.583 | 4.846 |
| | 0.667 | 5.697 |
| | 0.750 | 6.654 |
| | 0.833 | 7.718 |
| | 0.917 | 8.888 |
| | 1.000 | 9.845 |
| | 1.083 | 11.122 |
| | 1.167 | 12.185 |
| | 1.250 | 13.249 |
| | 1.333 | 14.525 |
| | 1.417 | 15.695 |
| | 1.500 | 17.078 |
| | 1.583 | 18.354 |
| | 1.667 | 19.843 |
| | 1.750 | 21.333 |
| 1.833 | 22.822 | |
| 1.917 | 24.311 | |
| 2.000 | 26.013 | |
| 0.017 | 0.060 | |
| 0.083 | 0.485 | |
| 0.167 | 1.123 | |
| 0.333 | 2.400 | |
| 0.500 | 3.889 | |
| 0.667 | 5.591 | |

| | Press. Diff. (cm H₂O) | Q (ml/sec) |
|---------------------|---|-----------------------|
| Forward Flow | 0.833 | 7.292 |
| | 1.000 | 9.632 |
| | 0.083 | 0.645 |
| | 0.167 | 1.412 |
| | 0.333 | 3.016 |
| | 0.667 | 6.787 |
| | 1.000 | 11.232 |
| | 1.333 | 16.487 |
| | 1.667 | 22.766 |
| | 2.000 | 27.198 |
| | 0.167 | 2.532 |
| | 0.333 | 3.647 |
| | 0.500 | 5.011 |
| | 0.667 | 6.462 |
| | 0.833 | 7.375 |
| | 1.000 | 8.297 |
| | 0.083 | 1.690 |
| | 0.167 | 2.150 |
| | 0.250 | 2.764 |
| | 0.333 | 3.434 |
| | 0.417 | 4.086 |
| | 0.500 | 4.797 |
| | 0.583 | 5.521 |
| | 0.667 | 6.304 |
| | 0.750 | 7.144 |
| | 0.833 | 7.650 |
| | 0.917 | 8.485 |
| | 1.000 | 9.593 |

APPENDIX B

RAMP UP AND RAMP DOWN TESTS IN THE FORWARD AND REVERSE FLOW DIRECTIONS

| | Press. Diff. (cm/H ₂ O) | Q (ml/sec) |
|-----------------------|---------------------------------------|---------------|
| Forward Test 1 | 0.000 | 0.002 |
| | 0.000 | 0.002 |
| | 0.000 | 0.002 |
| | 0.000 | 0.002 |
| | 0.000 | 0.002 |
| | 0.000 | 0.002 |
| | 0.075 | 0.016 |
| | 0.178 | 0.029 |
| | 0.250 | 0.043 |
| | 0.439 | 0.057 |
| | 0.424 | 0.071 |
| | 0.569 | 0.085 |
| | 0.693 | 0.099 |
| | 0.833 | 0.113 |
| | 0.915 | 0.127 |
| | 0.992 | 0.141 |
| | 1.087 | 0.154 |
| | 1.202 | 0.168 |
| | 1.290 | 0.182 |
| | 1.422 | 0.196 |
| | 1.534 | 0.210 |
| | 1.627 | 0.224 |
| | 1.759 | 0.238 |
| | 1.822 | 0.252 |
| | 1.943 | 0.265 |
| | 2.082 | 0.279 |
| | 2.158 | 0.293 |
| | 2.293 | 0.307 |
| | 2.412 | 0.321 |
| | 2.535 | 0.335 |
| | 2.655 | 0.349 |
| | 2.797 | 0.363 |
| | 2.944 | 0.377 |
| | 3.048 | 0.390 |
| | 3.122 | 0.404 |
| | 3.270 | 0.418 |
| | 3.428 | 0.432 |
| | 3.592 | 0.446 |
| | 3.881 | 0.460 |
| | 4.186 | 0.474 |
| | 4.261 | 0.488 |
| | 4.467 | 0.502 |
| | 4.672 | 0.515 |
| | 4.696 | 0.529 |

| Press. Diff. (cm/H₂O) | Q (ml/sec) |
|---|-----------------------|
| 4.884 | 0.543 |
| 5.122 | 0.557 |
| 5.089 | 0.571 |
| 5.282 | 0.585 |
| 5.366 | 0.599 |
| 5.764 | 0.613 |
| 5.637 | 0.626 |
| 5.793 | 0.640 |
| 6.107 | 0.654 |
| 6.130 | 0.668 |
| 6.307 | 0.682 |
| 6.406 | 0.696 |
| 6.591 | 0.710 |
| 6.652 | 0.724 |
| 6.881 | 0.738 |
| 6.998 | 0.751 |
| 7.101 | 0.765 |
| 7.394 | 0.779 |
| 7.513 | 0.793 |
| 7.806 | 0.807 |
| 8.403 | 0.821 |
| 7.972 | 0.835 |
| 8.272 | 0.849 |
| 8.223 | 0.863 |
| 8.381 | 0.876 |
| 8.653 | 0.890 |
| 8.570 | 0.904 |
| 9.055 | 0.918 |
| 8.882 | 0.932 |
| 9.332 | 0.946 |
| 9.583 | 0.960 |
| 9.821 | 0.974 |
| 9.841 | 0.988 |
| 10.176 | 1.001 |
| 10.008 | 1.000 |
| 10.022 | 1.000 |
| 10.923 | 1.000 |
| 10.077 | 1.000 |
| 9.872 | 1.000 |
| 9.849 | 1.000 |
| 10.083 | 1.000 |
| 9.865 | 1.000 |
| 9.927 | 1.000 |
| 10.187 | 1.000 |
| 10.687 | 1.000 |

| Press. Diff. (cm/H ₂ O) | Q (ml/sec) |
|---------------------------------------|---------------|
| 10.056 | 1.000 |
| 9.752 | 0.986 |
| 9.631 | 0.972 |
| 9.303 | 0.958 |
| 9.212 | 0.944 |
| 9.012 | 0.931 |
| 8.888 | 0.917 |
| 8.726 | 0.903 |
| 8.812 | 0.889 |
| 8.379 | 0.875 |
| 8.182 | 0.861 |
| 7.997 | 0.847 |
| 7.721 | 0.833 |
| 7.646 | 0.820 |
| 7.420 | 0.806 |
| 7.136 | 0.792 |
| 7.206 | 0.778 |
| 7.022 | 0.764 |
| 6.754 | 0.750 |
| 6.668 | 0.736 |
| 6.464 | 0.722 |
| 6.254 | 0.708 |
| 6.228 | 0.695 |
| 6.001 | 0.681 |
| 5.997 | 0.667 |
| 5.836 | 0.653 |
| 5.455 | 0.639 |
| 5.498 | 0.625 |
| 5.320 | 0.611 |
| 5.112 | 0.597 |
| 4.930 | 0.584 |
| 4.518 | 0.570 |
| 4.664 | 0.556 |
| 4.581 | 0.542 |
| 4.372 | 0.528 |
| 4.169 | 0.514 |
| 4.138 | 0.500 |
| 3.939 | 0.486 |
| 3.937 | 0.472 |
| 3.671 | 0.459 |
| 3.558 | 0.445 |
| 3.462 | 0.431 |
| 3.374 | 0.417 |
| 2.927 | 0.403 |
| 3.022 | 0.389 |

| Press. Diff. (cm/H₂O) | Q (ml/sec) |
|---|-----------------------------|
| 3.005 | 0.375 |
| 2.832 | 0.361 |
| 2.671 | 0.347 |
| 2.565 | 0.334 |
| 2.254 | 0.320 |
| 2.380 | 0.306 |
| 2.208 | 0.292 |
| 2.116 | 0.278 |
| 2.006 | 0.264 |
| 1.816 | 0.250 |
| 1.691 | 0.236 |
| 1.537 | 0.223 |
| 1.418 | 0.209 |
| 1.320 | 0.195 |
| 1.241 | 0.181 |
| 1.122 | 0.167 |
| 1.036 | 0.153 |
| 0.934 | 0.139 |
| 0.830 | 0.125 |
| 0.735 | 0.111 |
| 0.569 | 0.098 |
| 0.446 | 0.084 |
| 0.351 | 0.070 |
| 0.368 | 0.056 |
| 0.266 | 0.042 |
| 0.155 | 0.028 |
| 0.054 | 0.014 |
| Forward Test 2 | |
| 0.020 | 0.014 |
| 0.107 | 0.028 |
| 0.170 | 0.042 |
| 0.281 | 0.056 |
| 0.424 | 0.069 |
| 0.545 | 0.083 |
| 0.629 | 0.097 |
| 0.691 | 0.111 |
| 0.730 | 0.125 |
| 0.900 | 0.139 |
| 1.002 | 0.153 |
| 1.084 | 0.167 |
| 1.163 | 0.180 |
| 1.269 | 0.194 |
| 1.371 | 0.208 |
| 1.556 | 0.222 |
| 1.652 | 0.236 |

| Press. Diff. (cm/H₂O) | Q (ml/sec) |
|---|-----------------------|
| 1.687 | 0.250 |
| 1.832 | 0.264 |
| 1.920 | 0.278 |
| 2.080 | 0.292 |
| 2.149 | 0.305 |
| 2.278 | 0.319 |
| 2.403 | 0.333 |
| 2.549 | 0.347 |
| 2.630 | 0.361 |
| 2.724 | 0.375 |
| 2.858 | 0.389 |
| 3.054 | 0.403 |
| 3.081 | 0.417 |
| 3.271 | 0.430 |
| 3.384 | 0.444 |
| 3.500 | 0.458 |
| 3.716 | 0.472 |
| 3.830 | 0.486 |
| 3.609 | 0.500 |
| 4.047 | 0.514 |
| 4.349 | 0.528 |
| 4.287 | 0.541 |
| 4.488 | 0.555 |
| 4.518 | 0.569 |
| 4.795 | 0.583 |
| 4.946 | 0.597 |
| 5.012 | 0.611 |
| 5.308 | 0.625 |
| 5.322 | 0.639 |
| 5.701 | 0.653 |
| 5.557 | 0.666 |
| 5.706 | 0.680 |
| 6.033 | 0.694 |
| 6.126 | 0.708 |
| 6.332 | 0.722 |
| 6.461 | 0.736 |
| 6.682 | 0.750 |
| 6.757 | 0.764 |
| 6.951 | 0.777 |
| 7.279 | 0.791 |
| 7.346 | 0.805 |
| 7.380 | 0.819 |
| 7.654 | 0.833 |
| 7.775 | 0.847 |
| 7.887 | 0.861 |

| Press. Diff. (cm/H₂O) | Q (ml/sec) |
|---|-----------------------|
| 8.058 | 0.875 |
| 8.294 | 0.889 |
| 8.447 | 0.902 |
| 8.659 | 0.916 |
| 8.840 | 0.930 |
| 9.087 | 0.944 |
| 9.167 | 0.958 |
| 9.529 | 0.972 |
| 9.705 | 0.986 |
| 9.695 | 1.000 |
| 9.717 | 1.000 |
| 9.895 | 1.000 |
| 9.925 | 1.000 |
| 14.024 | 1.000 |
| 9.849 | 1.000 |
| 9.821 | 1.000 |
| 9.840 | 1.000 |
| 9.769 | 1.000 |
| 9.891 | 1.000 |
| 9.917 | 1.000 |
| 9.825 | 1.000 |
| 9.952 | 1.000 |
| 9.877 | 0.986 |
| 9.595 | 0.972 |
| 9.518 | 0.958 |
| 9.453 | 0.944 |
| 9.232 | 0.931 |
| 9.028 | 0.917 |
| 8.654 | 0.903 |
| 8.607 | 0.889 |
| 9.207 | 0.875 |
| 8.311 | 0.861 |
| 8.093 | 0.847 |
| 7.920 | 0.833 |
| 7.694 | 0.820 |
| 7.589 | 0.806 |
| 7.400 | 0.792 |
| 7.198 | 0.778 |
| 7.050 | 0.764 |
| 7.015 | 0.750 |
| 6.793 | 0.736 |
| 6.632 | 0.722 |
| 6.449 | 0.708 |
| 6.174 | 0.695 |
| 6.183 | 0.681 |

| Press. Diff. (cm/H₂O) | Q (ml/sec) |
|---|-----------------------|
| 5.825 | 0.667 |
| 5.891 | 0.653 |
| 5.669 | 0.639 |
| 5.580 | 0.625 |
| 5.339 | 0.611 |
| 5.215 | 0.597 |
| 4.999 | 0.584 |
| 5.001 | 0.570 |
| 4.706 | 0.556 |
| 4.606 | 0.542 |
| 4.398 | 0.528 |
| 4.406 | 0.514 |
| 4.102 | 0.500 |
| 4.080 | 0.486 |
| 3.850 | 0.472 |
| 3.783 | 0.459 |
| 3.656 | 0.445 |
| 3.458 | 0.431 |
| 3.362 | 0.417 |
| 3.210 | 0.403 |
| 3.084 | 0.389 |
| 2.994 | 0.375 |
| 2.803 | 0.361 |
| 2.739 | 0.347 |
| 2.626 | 0.334 |
| 2.446 | 0.320 |
| 2.382 | 0.306 |
| 2.221 | 0.292 |
| 2.132 | 0.278 |
| 1.999 | 0.264 |
| 1.906 | 0.250 |
| 1.805 | 0.236 |
| 1.643 | 0.223 |
| 1.580 | 0.209 |
| 1.476 | 0.195 |
| 1.367 | 0.181 |
| 1.234 | 0.167 |
| 1.178 | 0.153 |
| 1.041 | 0.139 |
| 0.927 | 0.125 |
| 0.858 | 0.111 |
| 0.718 | 0.098 |
| 0.716 | 0.084 |
| 0.465 | 0.070 |
| 0.497 | 0.056 |

| Press. Diff. (cm/H ₂ O) | Q (ml/sec) |
|---------------------------------------|---------------|
|---------------------------------------|---------------|

| | |
|-------|-------|
| 0.271 | 0.042 |
| 0.239 | 0.028 |
| 0.176 | 0.014 |
| 0.116 | 0.000 |
| 0.000 | 0.000 |
| 0.000 | 0.000 |
| 0.000 | 0.000 |

Forward Test 3

| | |
|-------|-------|
| 0.000 | 0.000 |
| 0.000 | 0.000 |
| 0.066 | 0.028 |
| 0.350 | 0.056 |
| 0.509 | 0.083 |
| 0.661 | 0.111 |
| 0.847 | 0.139 |
| 1.035 | 0.167 |
| 1.238 | 0.194 |
| 1.551 | 0.222 |
| 1.623 | 0.250 |
| 1.918 | 0.278 |
| 2.103 | 0.306 |
| 2.371 | 0.333 |
| 2.602 | 0.361 |
| 2.894 | 0.389 |
| 3.109 | 0.417 |
| 3.309 | 0.444 |
| 3.630 | 0.472 |
| 5.304 | 0.500 |
| 4.267 | 0.528 |
| 4.458 | 0.556 |
| 4.699 | 0.583 |
| 5.100 | 0.611 |
| 5.296 | 0.639 |
| 5.615 | 0.667 |
| 5.922 | 0.694 |
| 6.279 | 0.722 |
| 6.654 | 0.750 |
| 6.981 | 0.778 |
| 7.141 | 0.806 |
| 7.524 | 0.833 |
| 7.900 | 0.861 |
| 8.266 | 0.889 |
| 8.753 | 0.917 |
| 9.021 | 0.944 |
| 9.354 | 0.972 |

| Press. Diff. (cm/H ₂ O) | Q (ml/sec) |
|---------------------------------------|---------------|
| 10.179 | 1.000 |
| 9.838 | 1.000 |
| 9.866 | 1.000 |
| 9.732 | 0.972 |
| 9.495 | 0.944 |
| 9.085 | 0.917 |
| 8.715 | 0.889 |
| 8.307 | 0.861 |
| 7.953 | 0.833 |
| 7.630 | 0.806 |
| 7.237 | 0.778 |
| 6.950 | 0.750 |
| 6.654 | 0.722 |
| 6.238 | 0.694 |
| 5.876 | 0.667 |
| 5.708 | 0.639 |
| 5.394 | 0.611 |
| 5.046 | 0.583 |
| 4.813 | 0.556 |
| 4.553 | 0.528 |
| 4.198 | 0.500 |
| 3.917 | 0.472 |
| 3.628 | 0.444 |
| 3.368 | 0.417 |
| 3.194 | 0.389 |
| 2.895 | 0.361 |
| 2.638 | 0.333 |
| 2.386 | 0.306 |
| 2.220 | 0.278 |
| 1.945 | 0.250 |
| 1.725 | 0.222 |
| 1.525 | 0.194 |
| 1.257 | 0.167 |
| 0.987 | 0.139 |
| 0.804 | 0.111 |
| 0.690 | 0.083 |
| 0.418 | 0.056 |
| 0.266 | 0.028 |
| 0.125 | 0.000 |
| Forward Test 4 | |
| 0.004 | 0.000 |
| 0.011 | 0.002 |
| 0.009 | 0.002 |
| 0.006 | 0.002 |
| 0.155 | 0.018 |

| Press. Diff. (cm/H₂O) | Q (ml/sec) |
|---|-----------------------|
| 0.289 | 0.035 |
| 0.465 | 0.052 |
| 0.661 | 0.068 |
| 0.960 | 0.085 |
| 1.059 | 0.102 |
| 1.199 | 0.118 |
| 1.342 | 0.135 |
| 1.659 | 0.152 |
| 1.747 | 0.168 |
| 2.001 | 0.185 |
| 2.234 | 0.202 |
| 2.445 | 0.218 |
| 2.617 | 0.235 |
| 2.831 | 0.252 |
| 3.051 | 0.268 |
| 3.265 | 0.285 |
| 3.439 | 0.302 |
| 3.739 | 0.318 |
| 3.896 | 0.335 |
| 4.148 | 0.352 |
| 4.423 | 0.368 |
| 4.601 | 0.385 |
| 4.856 | 0.402 |
| 5.210 | 0.418 |
| 5.467 | 0.435 |
| 5.596 | 0.452 |
| 5.839 | 0.468 |
| 6.213 | 0.485 |
| 6.274 | 0.502 |
| 6.700 | 0.518 |
| 5.086 | 0.535 |
| 5.051 | 0.552 |
| 5.253 | 0.568 |
| 5.410 | 0.585 |
| 5.561 | 0.602 |
| 5.759 | 0.618 |
| 5.858 | 0.635 |
| 6.197 | 0.652 |
| 6.246 | 0.668 |
| 6.496 | 0.685 |
| 6.526 | 0.702 |
| 6.843 | 0.718 |
| 7.036 | 0.735 |
| 7.277 | 0.752 |
| 7.503 | 0.768 |

| Press. Diff. (cm/H₂O) | Q (ml/sec) |
|---|-----------------------|
| 7.512 | 0.785 |
| 8.299 | 0.802 |
| 7.981 | 0.818 |
| 8.439 | 0.835 |
| 8.447 | 0.852 |
| 8.445 | 0.868 |
| 8.896 | 0.885 |
| 8.902 | 0.902 |
| 9.324 | 0.918 |
| 9.538 | 0.935 |
| 9.686 | 0.952 |
| 9.974 | 0.968 |
| 10.386 | 0.985 |
| 10.554 | 1.000 |
| 10.614 | 1.000 |
| 10.460 | 1.000 |
| 10.570 | 1.000 |
| 10.499 | 1.000 |
| 10.568 | 1.000 |
| 10.484 | 1.000 |
| 10.377 | 1.000 |
| 10.677 | 1.000 |
| 10.493 | 1.000 |
| 10.498 | 1.000 |
| 10.501 | 1.000 |
| 10.530 | 1.000 |
| 10.588 | 1.000 |
| 10.582 | 1.000 |
| 10.366 | 1.000 |
| 10.380 | 1.000 |
| 10.440 | 1.000 |
| 10.342 | 1.000 |
| 0.009 | 0.002 |
| 0.005 | 0.002 |
| 0.200 | 0.018 |
| 0.322 | 0.035 |
| 0.594 | 0.052 |
| 0.684 | 0.068 |
| 0.899 | 0.085 |
| 1.088 | 0.102 |
| 1.212 | 0.118 |
| 1.426 | 0.135 |
| 1.620 | 0.152 |
| 1.787 | 0.168 |
| 1.990 | 0.185 |

| Press. Diff. (cm/H₂O) | Q (ml/sec) |
|---|-----------------------|
| 2.208 | 0.202 |
| 2.417 | 0.218 |
| 2.440 | 0.235 |
| 2.871 | 0.252 |
| 3.058 | 0.268 |
| 3.296 | 0.285 |
| 3.531 | 0.302 |
| 3.736 | 0.318 |
| 4.007 | 0.335 |
| 4.122 | 0.352 |
| 4.372 | 0.368 |
| 4.631 | 0.385 |
| 4.748 | 0.402 |
| 5.144 | 0.418 |
| 5.359 | 0.435 |
| 5.618 | 0.452 |
| 5.906 | 0.468 |
| 6.185 | 0.485 |
| 6.442 | 0.502 |

Reverse Test 1

| | |
|-------|-------|
| 0.000 | 0.000 |
| 0.485 | 0.083 |
| 1.230 | 0.167 |
| 1.761 | 0.250 |
| 2.400 | 0.333 |
| 3.038 | 0.417 |
| 3.889 | 0.500 |
| 4.740 | 0.583 |
| 5.591 | 0.667 |
| 6.441 | 0.750 |
| 7.505 | 0.833 |
| 8.569 | 0.917 |
| 9.739 | 1.000 |
| 9.739 | 1.000 |
| 8.462 | 0.917 |
| 7.292 | 0.833 |
| 6.441 | 0.750 |
| 5.591 | 0.667 |
| 4.740 | 0.583 |
| 3.889 | 0.500 |
| 3.038 | 0.417 |
| 2.293 | 0.333 |
| 1.761 | 0.250 |
| 1.336 | 0.167 |

| Press. Diff. (cm/H₂O) | Q (ml/sec) |
|---|-----------------------|
| 0.485 | 0.083 |
| 0.000 | 0.000 |
| 0.485 | 0.083 |
| 1.123 | 0.167 |
| 1.549 | 0.250 |
| 2.187 | 0.333 |
| 3.038 | 0.417 |
| 3.676 | 0.500 |
| 4.527 | 0.583 |
| 5.591 | 0.667 |
| 6.229 | 0.750 |
| 7.292 | 0.833 |
| 8.356 | 0.917 |
| 9.632 | 1.000 |
| 9.632 | 1.000 |
| 8.569 | 0.917 |
| 7.292 | 0.833 |
| 6.441 | 0.750 |
| 5.378 | 0.667 |
| 4.740 | 0.583 |
| 3.676 | 0.500 |
| 3.038 | 0.417 |
| 2.187 | 0.333 |
| 1.761 | 0.250 |
| 1.123 | 0.167 |
| 0.485 | 0.083 |
| 0.000 | 0.000 |
| 0.272 | 0.083 |
| 0.910 | 0.167 |
| 1.549 | 0.250 |
| 1.974 | 0.333 |
| 2.825 | 0.417 |
| 3.463 | 0.500 |
| 4.314 | 0.583 |
| 5.165 | 0.667 |
| 6.229 | 0.750 |
| 7.080 | 0.833 |
| 8.143 | 0.917 |
| 9.632 | 1.000 |
| 9.632 | 1.000 |
| 8.569 | 0.917 |
| 7.292 | 0.833 |
| 6.441 | 0.750 |
| 5.591 | 0.667 |
| 4.740 | 0.583 |

| Press. Diff. (cm/H ₂ O) | Q (ml/sec) |
|---------------------------------------|---------------|
| 3.889 | 0.500 |
| 3.038 | 0.417 |
| 2.400 | 0.333 |
| 1.761 | 0.250 |
| 1.123 | 0.167 |
| 0.485 | 0.083 |

Reverse Test 2

| | |
|-------|-------|
| 0.000 | 0.000 |
| 0.485 | 0.083 |
| 1.230 | 0.167 |
| 1.761 | 0.250 |
| 2.400 | 0.333 |
| 3.038 | 0.417 |
| 3.889 | 0.500 |
| 4.740 | 0.583 |
| 5.591 | 0.667 |
| 6.441 | 0.750 |
| 7.505 | 0.833 |
| 8.569 | 0.917 |
| 9.739 | 1.000 |
| 9.739 | 1.000 |
| 8.462 | 0.917 |
| 7.292 | 0.833 |
| 6.441 | 0.750 |
| 5.591 | 0.667 |
| 4.740 | 0.583 |
| 3.889 | 0.500 |
| 3.038 | 0.417 |
| 2.293 | 0.333 |
| 1.761 | 0.250 |
| 1.336 | 0.167 |
| 0.485 | 0.083 |

Reverse Test 3

| | |
|-------|-------|
| 0.000 | 0.000 |
| 0.485 | 0.083 |
| 1.123 | 0.167 |
| 1.549 | 0.250 |
| 2.187 | 0.333 |
| 3.038 | 0.417 |
| 3.676 | 0.500 |
| 4.527 | 0.583 |
| 5.591 | 0.667 |
| 6.229 | 0.750 |
| 7.292 | 0.833 |
| 8.356 | 0.917 |

| Press. Diff. (cm/H ₂ O) | Q (ml/sec) |
|---------------------------------------|---------------|
| 9.632 | 1.000 |
| 9.632 | 1.000 |
| 8.569 | 0.917 |
| 7.292 | 0.833 |
| 6.441 | 0.750 |
| 5.378 | 0.667 |
| 4.740 | 0.583 |
| 3.676 | 0.500 |
| 3.038 | 0.417 |
| 2.187 | 0.333 |
| 1.761 | 0.250 |
| 1.123 | 0.167 |
| 0.485 | 0.083 |

Reverse Test 4

| | |
|-------|-------|
| 0.000 | 0.000 |
| 0.272 | 0.083 |
| 0.910 | 0.167 |
| 1.549 | 0.250 |
| 1.974 | 0.333 |
| 2.825 | 0.417 |
| 3.463 | 0.500 |
| 4.314 | 0.583 |
| 5.165 | 0.667 |
| 6.229 | 0.750 |
| 7.080 | 0.833 |
| 8.143 | 0.917 |
| 9.632 | 1.000 |
| 9.632 | 1.000 |
| 8.569 | 0.917 |
| 7.292 | 0.833 |
| 6.441 | 0.750 |
| 5.591 | 0.667 |
| 4.740 | 0.583 |
| 3.889 | 0.500 |
| 3.038 | 0.417 |
| 2.400 | 0.333 |
| 1.761 | 0.250 |
| 1.123 | 0.167 |
| 0.485 | 0.083 |